TECHNISCHE UNIVERSITÄT MÜNCHEN
LEHRSTUHL FÜR HOCHFREQUENZTECHNIK

Near-Field Error Analysis and Efficient Sampling Techniques for the Fast Irregular Antenna Field Transformation Algorithm

Muhammad Ayyaz Qureshi

Vollständiger Abdruck der von der Fakultät für Elektrotechnik und Informationstechnik der Technische Universität München zur Erlangung des akademischen Grades eines

Doktor-Ingenieurs

genehmigten Dissertation.

Vorsitzender: Univ.-Prof. Dr. sc. techn. Andreas Herkersdorf

Prüfer der Dissertation:

1. Univ.-Prof. Dr.-Ing. Thomas Eibert

2. Prof. Dr. ir. Hendrik Rogier

Universiteit Gent / Niederlande

Die Dissertation wurde am 13.06.2013 bei der Technische Universität München eingereicht und durch die Fakultät für Elektrotechnik und Informationstechnik am 04.10.2013 angenommen.

I confirm that this thesis is an original work of mine and is completed independently without inadmissible outside help.

Munich, December 4, 2013

Muhammad Ayyaz Qureshi

Acknowledgements

I would like to thank everyone who helped me in achieving this goal. I am thankful to my Ph.D. supervisor Prof. Thomas F. Eibert from the bottom of my heart for providing me an opportunity to do this work with the Institute of High Frequency Engineering. His positive criticism and continuous guidance through various conversations is an asset to me. It is his kind supervision which made me win best student paper awards in AMTA symposium for the consecutive years. Apart from studies, he has been a wonderful person nurturing and supporting me in many other non-educational matters.

Special thanks to Dr. Carsten Schmidt who facilitated me to achieve the results of this thesis. His continuous motivation and academic support made everything possible from the very beginning. He provided me with a wide range of references and also helped in reviewing this work.

I am grateful to Kazeem and Jawad for reviewing this work and for the fruitful discussions we had over a period of time. I would also acknowledge Astrium, Kathrein Werke, and NSI people for providing the measurement data and all other colleagues in the institute to whom I interacted in some way or the other. Not to forget my family who supported me from the day I was born and I am sure they will be supporting me as long as I need them. I must admit the support of my loving wife who also gave me the greatest gift of my life, my daughter Hania.

Finally, I would like to dedicate this work to my father M. Jahangir Qureshi for being a constant source of inspiration during my studies.

Munich, December 4, 2013
M. Ayyaz Qureshi

Contents

Abbreviations

AUT	Antenna under Test
CATR	Compact Antenna Test Range
CPU	Central Processing Unit
CS	Cardinal Series
dB	Decibel
dBi	Decibel Isotropic- gain/directivity of an antenna compared with hypothetical isotropic antenna
EM	Electromagnetic
RF	Radio Frequency
FFT	Fast Fourier Transform
2D FFT	Two Dimensional Fast Fourier Transform
FIAFTA	Fast Irregular Antenna Field Transformation Algorithm
FMM	Fast Multipole Method
GMRES	Generalized Minimum Residual Method
IEEE	Institute of Electronics and Electrical Engineers
LMS	Least Mean Square
MLFMM	Multilevel Fast Multipole Method
MoM	Method of Moments
NFT	Near-Field Transformation
NFFFT	Near-Field Far-Field Transformation
NIST	National Institute of Standards and Technology
NSI	Near-Field System Inc.
OEWG	Open Ended Waveguide
OSI	Optimal Sampling Interpolation
PDA	Personal Digital Assistant
PCHIP	Piecewise Cubic Hermite Interpolation
PNF	Planar Near Field
SLL	Side Lobe Level
SNR	Signal to Noise Ratio
WLAN	Wireless Local Area Network

Nomenclature

$\|\|A\|\|$	matrix
$\boldsymbol{A}$	vector
$\hat{\boldsymbol{A}}$	unit vector
$\|\boldsymbol{A}\|$	magnitude of a vector
*	conjugate complex
^{H}	adjoint (conjugate complex transpose)
$\bar{\boldsymbol{A}}$	Dyad
$\bigtriangledown$	Nabla operator
$\bigtriangledown \boldsymbol{A}$	Gradient
$\bigtriangledown \cdot \boldsymbol{A}$	Divergence
$\bigtriangledown \times \boldsymbol{A}$	Rotation

Symbols

$\|\|C\|\|$		coupling matrix
$\|\|C\|\|^H$		complex conjugate transpose of coupling matrix $\|\|C\|\|$
$C^{1/2}_{\phi/\theta}(k_\phi, k_\theta, \phi, \theta)$		coupling matrix element
$C(\phi, \theta), C(\hat{k}, \boldsymbol{r}_\mathrm{M})$		antenna radiation pattern
$C^{sn}_{\sigma,\mu,\nu}(kr_\mathrm{M})$		translation operator for spherical modes
d_a	m	diameter of the minimum sphere enclosing the antenna
d_p	m	diameter of the minimum sphere enclosing the probe
$d^n_{\mu m}(\theta)$		rotation coefficient for spherical wave function
$\mathrm{d}V$	m^3	infinitesimal volume element
$\mathrm{d}x$,$\mathrm{d}y$,$\mathrm{d}z$	m	infinitesimal length element
D	dB	directivity
$\boldsymbol{D}(\boldsymbol{K})$	Am	plane wave spectrum of measured data
$\bar{\boldsymbol{D}}^{i_n}_n\left(\boldsymbol{k}, \boldsymbol{r}^{i_n}_n\right)$		disaggregation and anterpolation operator
$\boldsymbol{e}_\theta, \boldsymbol{e}_\phi, \boldsymbol{e}_r$		spherical unit vectors
$\boldsymbol{E}(\boldsymbol{r})$	V/m	electric field strength
$\boldsymbol{E}_\mathrm{FF}$	V	electric far field
f	Hz	frequency
$\boldsymbol{F}^{(3)}_{smn}(\phi, \theta, r_\mathrm{M})$		spherical wave functions
$F^{1/2}$		impedance mismatch factor of probe 1 and probe 2
G	dB	antenna gain
$\bar{\boldsymbol{G}}(\boldsymbol{r}, \boldsymbol{r'})$	V/(Am^2)	Green's function of free space
$\mathrm{h}^{(2)}_l(x)$		spherical Hankel function of second kind
$\bar{\boldsymbol{I}}$		unit dyad
$\boldsymbol{I}^{1/2}_n$		cylindrical angular spectra
j		imaginary unit
$\boldsymbol{J}(\boldsymbol{r})$	A/m^2	electric current density
$\tilde{\boldsymbol{J}}(\hat{k})$	Am	plane wave spectrum
$\tilde{\boldsymbol{J}}_\mathrm{ef}$	Am	assumed error free plane wave spectrum
$\tilde{\boldsymbol{J}}_\mathrm{err}$	Am	error spectrum
$\tilde{\boldsymbol{J}}_\mathrm{o}$	Am	erroneous plane wave spectrum
$\boldsymbol{J}^{i_n}_n(\hat{k})$	Am	plane wave spectrum, level n, box i_n

$\boldsymbol{k}$	1/m	propagation vector, defines direction of plane wave
$\boldsymbol{K}$	1/m	transverse part of $\boldsymbol{k}$
k	1/m	wave number
k_x, k_y, k_z	1/m	wave number in x-, y-, and z-direction
k_ϕ, k_θ	1/m	wave number in ϕ- and θ-direction
L		multipole order
L_{T_L}		multipole order of translation operator
L_{AUT}		multipole order of the AUT
L_ϕ, L_θ	m	dimensions of planar measurement surface
L_{smn}	m	far-field pattern function
M, N		number of measurement points
P, Q		number of integration points
$\bar{\boldsymbol{P}}(\hat{k}, \boldsymbol{r}_{\text{M}})$	m	probe correction coefficient
P_{in}	W	input power
$\boldsymbol{P}$	m	transverse position vector
$\text{P}_l(x)$		Legendre polynomial of first kind
P_{rad}	W	radiated power
$Q^{(3)}_{smn}$	$\sqrt{\text{W}}$	spherical mode coefficients
r	m	radial distance from the antenna
$\boldsymbol{r}, \boldsymbol{r}_m$	m	position vector of an observation point
$\boldsymbol{r}', \boldsymbol{r}_n$	m	position vector of a point source
$\boldsymbol{r}_{\text{box}}$	m	vector AUT- box center on highest level
r_{FF}	m	far-field distance
r_{M}	m	measurement distance
$\boldsymbol{r}_{\text{M}}$	m	position vector of a measurement point
$\tilde{\boldsymbol{r}}_{\text{M}}$	m	vector box center of lowest level to the measurement point
$R_{\sigma,\mu,\nu}$		probe receiving coefficient (spherical near-field transformation)
$R_n^{(1/2)s}$		cylindrical receiving function of probe 1 and probe 2
s, m, n		mode indices, additionally m and n also denote main and cross components
$\boldsymbol{S}(k_y, k_z, \chi)$	1/m^2	probe characteristics (planar near-field measurement)
$\boldsymbol{s}^1_{02}(\boldsymbol{k}), \boldsymbol{s}^2_{02}(\boldsymbol{k})$		receiving parameters of probe 1 and probe 2
$T_L(\hat{k}, \boldsymbol{r}_{\text{M}})$	1/m	FMM translation operator
T^s_n		cylindrical wave transmitting function
$\boldsymbol{t}_{10}(\boldsymbol{k})$		transmitting parameter of the AUT
$\boldsymbol{U}(\boldsymbol{r}_{\text{M}})$	V	probe signal
$\boldsymbol{U}_{\text{o}}$	V	erroneous probe signal

$\boldsymbol{U}_{\text{err}}$	V	error in the probe signal
$\boldsymbol{U}_{\text{ef}}$	V	assumed error free probe signal
V	m^3	integration volume
V_o	V	input voltage to the AUT
V_{probe}	m^3	volume of the probe
$\boldsymbol{w}_{\text{probe}}(\boldsymbol{r})$	$1/\text{m}^2$	probe characteristic
$W_\theta^{l,n}, W_\phi^n$		quadrature weights
x, y, z		Cartesian coordinates
χ	$^\circ$	probe polarization angle
ϵ		error in the near field
ϵ_o	As/(Vm)	electric permittivity of free space $\approx (8.8541 * 10^{-12}$ As/Vm)
ϵ_r		relative dielectric permittivity
τ		relative residuum of GRMRES Solver
γ		factor controlling the accuracy of expansion of multipole order of the translation operator
ϕ, θ, r		spherical coordinates
η		efficiency
λ	m	wavelength
μ_o	Vs/(Am)	permeability of free space $(4\pi \cdot 10^{-7}$ Vs/(Am))
ν	m	antenna factor
π		constant (3.1415...)
$\rho(\boldsymbol{r})$	As/m^3	electric space charge density
$\rho_{\text{m}}(\boldsymbol{r})$	Vs/m^3	magnetic space charge density
σ, μ, ν		mode indices in probe coordinate system
$\sigma_s^{1/2}(\boldsymbol{k})$		polarization ratios of probe 1 and probe 2
ω	1/s	angular frequency
δ_x, δ_y	m	sample spacing in x- and y-direction
Γ_l, Γ_p		reflection coefficient of the load and the probe

Abstract

Near-field antenna measurements have been used for quite some time to determine the radiation pattern of antennas. Low cost, controlled environment, and good accuracy are some of the key advantages offered by near-field measurements. Standard near-field antenna measurements are commonly performed on planar, cylindrical, and spherical scanning surfaces to facilitate modal expansion methods making use of orthogonal modes in the post processing. The post-processing employs two dimensional Fast Fourier Transform (2D FFT) for an efficient computation. Like any other measurement technique, a reliable estimate of errors in the near-field measurement is carried out and there are many contributions in which the far-field uncertainty against these near-field errors using standard transformations techniques is determined. Due to the inability of 2D FFT based approaches to process near-field data collected on arbitrary grids and the high computational cost for full probe correction specifically in spherical measurements, equivalent source based transformation techniques have been developed in the recent past [1], [2], [3]. The Fast Irregular Antenna Field Transformation Algorithm (FIAFTA) [4] is one such technique which makes use of plane waves as equivalent sources. The sole algorithm can handle measurements on standard as well as arbitrary grids efficiently with full probe correction.

FIAFTA is an efficient near-field transformation technique and offers advantages like low computational complexity, full probe correction, near-field measurements on arbitrary grids, etc. In contrast to other plane wave based approaches FIAFTA utilizes the complete Ewald sphere of propagating plane waves which makes it more robust. Also, the use of plane waves as equivalent sources combined with Multilevel Fast Multipole Method (MLFMM) like acceleration makes it an efficient algorithm because it avoids the step involving the generation of plane waves from other equivalent sources like electric or magnetic currents.

In this work, a rigorous error analysis for the FIAFTA is performed for the first time. The performance maturity of FIAFTA is determined against standard near-field measurement errors. The near-field measurement errors include probe position inaccuracies, errors due to instrumentation uncertainties, and other general errors like scan area truncation etc. In the first step, the error analysis is performed for the planar measurements which is then compared with the traditional transformation technique employing 2D FFT. A common observation implicit in the available literature is that the error analysis is usually valid only for a given set of antennas and it assumes a specific scanning geometry. Error equations are not generalized and may not be applicable to all antennas. Also, the analysis is usually performed with emphasis on estimating the error in the main beam and in the first side lobe of the transformed far field. The mean and the maximum error estimation within the valid angle of the transformed far field needs more rigorous analysis. It is highly desirable to derive an error model which is suitable for arbitrary measurement grids and is suitable for all kind of antennas. The error model should also provide realistic error estimates and does not always consider the worst case scenario.

The challenging task of determining the error behavior of FIAFTA against near-field errors is analyzed afterwards keeping in view of arbitrary antennas measured on arbitrary scanning surfaces. Though we consider FIAFTA in the error analysis, the proposed error model is equally valid for transformation techniques making use of other equivalent sources like electric currents. These techniques use a forward operator in the formulation of the transmission equation. The linearity of the forward operator makes it possible to oversee the effect of near-field errors and to estimate the mean and the maximum error in the transformed far field. The accuracy of the estimated uncertainty in the far field is dependent on the knowledge of the near-field measurement inaccuracies. The magnitude of other near-field measurement inaccuracies can be extracted from the data sheets of the equipment. Once the uncertainties in near-field parameters are known, they can be used to find the uncertainty in the plane wave spectrum representing the AUT fields and hence the error in the far field. The novel error model is applied to a synthetically modelled horn antenna whose near field is collected on planar, cylindrical, and spherical grids. The near field is distorted with arbitrary errors and is processed using FIAFTA. The computed and the observed far-field uncertainty due to introduced errors are in accordance with each other and thus validate the proposed error model.

During the standard planar and cylindrical near-field scanning, the samples are mostly collected with a sample spacing of $\lambda/2$ in order to avoid errors in the reconstruction of the radiation pattern using standard 2D FFT based post-processing techniques. However, the regular 2D grid is only used to facilitate the specific transformation technique and poses a huge computational burden especially when dealing with electrically large antennas. The number of samples can be tremendously reduced if only necessary samples distributed efficiently on the scanning surface are used and the near-field data is post-processed using an efficient equivalent source based technique like FIAFTA. Such a reduction in the number of near-field samples along with effective scanning techniques is discussed in the second part of this contribution.

A unique approach to reduce the measurement time by reducing the number of data points in the near-field antenna measurements is presented. In this technique, the measurement system adapts itself during the measurement process and based on a given decision threshold, it concentrates mainly on the strongly changing near-field regions while skipping data points from smoothly varying locations. In contrast to the adaptive acquisition techniques proposed previously, the valid angle is not reduced and as such no extra measurement step is required. However, the extent at which the measurement time is reduced depends on the near-field distribution. Best results have been achieved for antennas with smoothly varying near-fields. The irregular grid obtained as a result of adaptive scanning is processed using the FIAFTA and showed promising results.

In another novel technique, a nonredundant sampling representation on arbitrary surfaces in near-field antenna measurements is described. The utilized sampling criterion depends on the electrical size of the antenna under test (AUT) along with the separation between the AUT and the measurement surface. The minimum number of samples required is directly linked with the number of unknowns in the linear system of equations derived considering spherical expansion of radiated AUT fields. Equivalent plane wave sources are used to represent the AUT fields. Plane wave translations can be directly performed for any arbitrary measurement grid with the same efficiency. Thus, nonredundant sampling representations can be utilized on any scan surface. The proposed sampling is applied to near-field measurements using a variety of antennas and the results are compared to the case of standard sampling. A remarkable decrease in the number of measurement points is observed with a negligible change in the accuracy of the transformed pattern, thereby greatly reducing the measurement time and the computational effort.

Chapter 1

Introduction

There has been a massive growth in the field of wireless communications in the last decade. The use of communication devices like mobile phones [5] [6], PDAs, notebooks, GPS, etc. have increased tremendously and is likely to increase in an exponential manner in the coming years. The usage and performance of all these devices are majorly linked with the performance of the transmitting and receiving component, i.e. the antenna. With increasing numbers and competition, innovative antenna designs with strict requirements are obvious especially in the space industry for satellite communication and for military purposes. The most effective and widely employed way to characterize antennas is by antenna measurements. Antenna measurements determine whether the designed antenna meets the desired specifications or not. Testing of antennas is not only a tricky business but also requires a lot of care in equipment handling during the measurements. Antenna parameters like radiation pattern, gain, bandwidth, and polarization are determined during the measurements.

Direct far-field measurements, compact range measurements [7] [8] and near-field measurements [9] are widely used for the characterization of antennas. Far-field measurements mostly involve outdoor ranges for electrically large antennas. The uncontrolled environment in the outdoor ranges limits the applicability of far-field measurements. Additionally, interference from other sources, reflections, huge land requirement, etc. bound the use of far-field measurements only for some specific applications. In contrast, compact range measurements are carried out in a controlled environment in shielded chambers. Reflected signals are also avoided by the use of proper absorbers and temperature is monitored by using air-conditioning mechanisms. Using compact ranges, direct measurements of the radiated field are possible in real time and the far-field condition is emulated at a short distance with the help of a special measurement setup. However, the expensive setup practically limits the use of compact ranges in general antenna measurements. The development of near-field scanning as a method of measuring antennas offers the advantage of using smaller area at lower expenditure as compared to direct far-field measurements. Near-field measurements are also carried out in a controlled and shielded environment. The collected near-field data is post-processed using appropriate near-field far-field (NFFF) transformation algorithms to finally determine the radiation pattern of the AUT. Nevertheless, near-field scanning is prone to errors and needs special care during the measurement. Minute errors in the near-field data can corrupt the far field depending on the maturity of the NFFF transformation algorithm.

Near-field measurements have gained a lot of importance for the last many decades due to mentioned advantages like small space requirements, low cost, controlled environment, etc. The traditional NFFF transformation algorithms mostly make use of modal expansion methods and utilize orthogonal modes in the post-processing of the acquired near-field data [9]. Afterwards, for

an efficient computation, 2D FFT is employed. However, the use of orthogonal modes limit the shape of the scanning grids only to canonical surfaces according to the choice orthogonal expansion functions. The use of 2D FFT in the modal expansion methods defines the sampling criteria to be used during the near-field measurements which may not be the requirement of the NFFF transformation itself. These two serious limitations reduce the flexibility of near-field measurements to a huge extent. Measurements on the arbitrary grids according to the choice of antenna or the available equipment along with the least possible number of measurement points are highly desirable. Afterwards, a reliable estimate of errors considering arbitrary surfaces and arbitrary antennas is of key concern to establish confidence on the used transformation algorithm. The main focus of this thesis revolves around these three objectives:

- the use of transformation algorithm based on equivalent sources which is capable of handling measurements on arbitrary grids [1], [2], [3]. We utilize Fast Irregular Antenna Field Transformation Algorithm (FIAFTA) [10], [4] based on equivalent plane wave sources.
- a comparative error analysis between the FIAFTA and traditional transformation techniques employing 2D FFT along with a reliable estimate of far-field uncertainties against arbitrary near-field errors considering arbitrary surfaces and antennas.
- computation of a least number of sampling points and their representation on arbitrary surfaces which can reduce the measurement burden to a great extent.

Chapter 2 summarizes the essentials of antenna measurements. Basic antenna parameters are revised and the necessary formulation of the standard transformation techniques i.e. planar, cylindrical, and spherical near-field transformation is described. Similarly, in chapter 3, the summary of FIAFTA is revisited. The formulation of the transmission equation along with the grouping of measurement points in an hierarchical structure for efficient computation is explained.

In chapter 4, the behavior of FIAFTA against planar near-field measurement errors is examined and is compared to the standard planar transformation technique employing two dimensional Fast Fourier Transform (2D FFT). By using synthetic modelling of the antenna under test (AUT), the effect of individual errors generated in a realistic way is quantified and the sensitivity of FIAFTA against these errors is determined. A comparative error analysis between FIAFTA and standard transformation technique employing 2D FFT showed better performance of FIAFTA against errors like scan area truncation, probe pattern inaccuracy, RF amplitude inaccuracy, etc. The error analysis is extended in chapter 5 to include errors while considering arbitrary scanning surfaces. Expressions are derived to estimate the far-field uncertainty using the available near-field data together with the measurement inaccuracy but, most importantly, without the knowledge of the reference far field. Error analysis techniques presented so far either assume a specific set of antennas or a specific measurement surface and are difficult to generalize. The error model presented in chapter 5 is generalized and can handle arbitrary antennas measured on arbitrary surfaces. Examples are provided afterwards to show the applicability of the proposed error model.

In chapter 6, adaptive near-field acquisition techniques along with scanning methodologies are presented for planar, cylindrical, and spherical near-field measurements. The near-field measurement errors practically set the number of required near-field samples which is considered in the adaptive acquisition. The presented technique applies higher sampling density in rapidly varying near-field regions and skips data points in the smoother regions. Abrupt changes in the near field are detected by comparing the extrapolated and the measured near-field values at coarser spacing during the measurements. An empirically derived decision function based on the signal-to-noise ratio of the measured value is used to determine the threshold difference between the extrapolated

and the measured near-field value for skipping the sampling point. Several test cases are then presented on the applicability of the given approach and a significant reduction in the number of measurement points is observed, thereby reducing measurement time and the computational effort.

Chapter 7 deals with the nonredundant sampling representation on arbitrary surfaces in near-field antenna measurements considering FIAFTA as the direct near-field transformation technique. The minimum number of near-field samples required is linked with the number of unknowns in the linear system of equations used in the formulation of FIAFTA. The sampling criterion is found dependent on the electrical size of the antenna and the separation between the AUT and the measurement surface. Several examples are presented afterwards showing a negligible change in the accuracy while marking a huge reduction in the number of required near-field samples.

Chapter 8 concludes all the relevant work and provides an overview of possible extensions.

Chapter 2

Overview of Antenna Measurements

Antenna measurements are used to determine the radiation characteristics of an AUT. There are various factors which cannot be considered during simulations while designing the antenna and therefore antenna behavior must be verified via measurements. Also, the behavior of the antenna is effectively changed when it is mounted on different objects e.g. vehicles after which full scale simulations become difficult to perform. Antenna measurements can then be used to ascertain the insitu performance. Commonly adapted ways for the antenna testing are direct far-field measurements, compact range measurements [7], [8], and near-field measurements [9]. Each technique has its own advantages and disadvantages. Before reviewing these techniques, we first revise the basic antenna parameters which are essential for describing the performance of an antenna. The definitions are taken from *IEEE Standard Definitions of Terms for Antennas* [11] and are shown in quotation marks.

2.1 Antenna Parameters

2.1.1 Radiation Pattern

The radiation pattern $C(\phi, \theta)$ of an antenna is defined as "a mathematical function or a graphical representation of the radiation properties of the antenna as a function of space coordinates. In most cases, the radiation pattern is determined in the far-field region and is represented as a function of the directional coordinates." The far-field distance is commonly approximated as $r_{\mathrm{FF}} = 2d^2/\lambda_o$, where d is the diameter of the minimum sphere enclosing the antenna and λ_o is the wavelength. The radiation pattern can be quantitatively written as

$$C(\phi, \theta) = \frac{E(\phi, \theta)}{E_{\max}}, \tag{2.1}$$

using the spherical coordinates ϕ and θ and it is independent of the radial distance [12]. The field pattern is commonly normalized with the maximum value to obtain the normalized field pattern. Normally, planar sections of the radiation pattern are shown instead of complete three dimensional surfaces. Among those two most important views are the E-plane and the H-plane patterns. The E-plane pattern is a view of the radiation pattern which includes the plane containing the maximum value of the radiated field and the E-field vector. Similarly, the H-plane pattern is a sectional view in which the H-field lies in the plane of the section and also contains the direction of maximum radiation [14]. Fig. 2.1 shows three dimensional (3D) radiation pattern of an horn antenna in spherical coordinates.

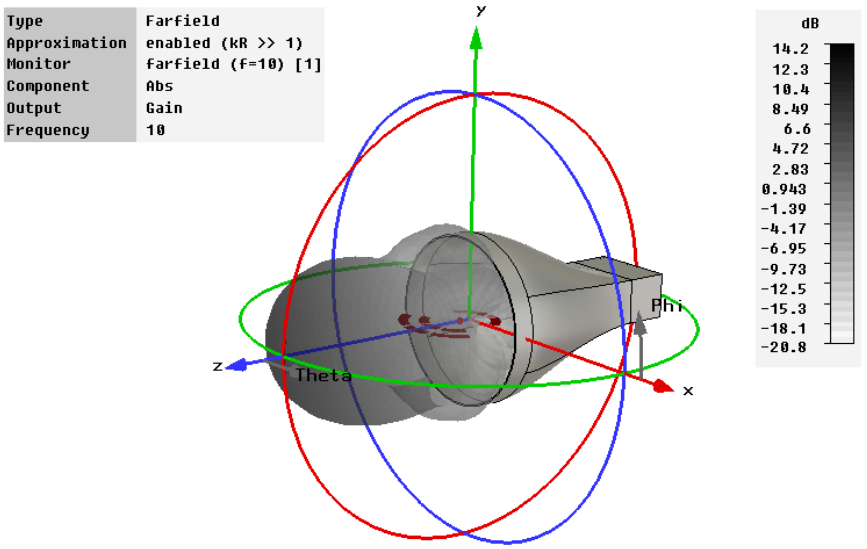

Figure 2.1: 3D Radiation pattern of a horn antenna.

2.1.2 Gain and Directivity

The directivity of an antenna D is defined as "the ratio of the radiation intensity in a given direction from the antenna to the radiation intensity averaged over all directions. The average radiation intensity is equal to the total power radiated by the antenna divided by 4π. If the direction is not specified, the direction of maximum radiation intensity is implied [11]." The directivity

$$D = \frac{4\pi}{\int_{\phi=0}^{2\pi}\int_{\theta=0}^{\pi}|C|^2(\phi,\theta)\sin(\theta)d\theta d\phi} \tag{2.2}$$

can be quantitatively written in terms of radiation pattern. It is often desirable to express the directivity in decibles (dB) instead of dimensionless quantities. The conversion of directivity from dimensionless quantity to decibles is

$$D(\text{dB}) = 10\log_{10}(D). \tag{2.3}$$

The gain of the antenna G is closely related with the directivity and takes the antenna efficiency into account. The antenna efficiency includes the effect of reflection due to mismatch between the transmission line and the antenna along with the conduction and dielectric losses of the antenna. Therefore, the gain of the antenna is defined as "the ratio of the intensity, in a given direction, to the radiation intensity that would be obtained if the power accepted by the antenna were radiated isotropically. The radiation intensity corresponding to the isotropically radiated power is equal to the power accepted (input) by the antenna divided by 4π." In simple words antenna gain

$$G = \eta D \tag{2.4}$$

is a a product of the antenna radiation efficiency $\eta = P_{\text{rad}}/P_{\text{in}}$ and the directivity, where P_{rad} is the total power radiated by the antenna and P_{in} is the total power accepted by the antenna at its input terminals.

2.1.3 Polarization

"The polarization of an antenna is the curve traced by the instantaneous electric field radiated by the antenna in a plane perpendicular to the radial direction [12]". The polarization is generally classified as elliptical of which the linear and the circular polarizations are special cases. The electric field is linearly polarized if the vector describing the electric field in space as a function of time is always directed along the line. The electric field has elliptical or circular polarization if the figure traced by the field is an ellipse or a circle. The electric field is either traced in a clockwise or anticlockwise direction and is therefore commonly referred to as right hand (RHP) or left hand polarization (LHP), respectively [15]. For circular polarization, the terms right hand circular polarization (RHCP) or left hand circular polarization (LHCP) are often used. The geometric figures traced by the sum of the E-field vectors i.e. E_x and E_y over time are shown in Fig. 2.2.

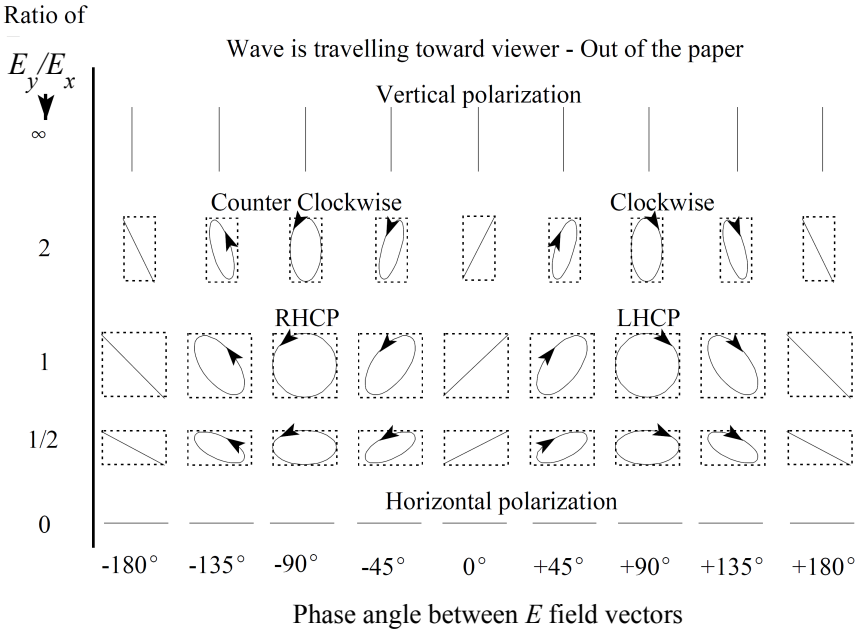

Figure 2.2: Polarization as a function of E- and H-field vector and the phase angle [13].

2.1.4 Bandwidth

The bandwidth of an antenna corresponds to "the range of frequencies within which the performance of the antenna, with respect to some characteristic, conforms to a specific standard [16]". The antenna bandwidth is a set of frequencies around the center frequency with in which the antenna characteristics do not vary significantly as compared to their values at the center frequency. The absolute bandwidth is expressed in "Hz" while the relative bandwidth is denoted in "%" with respect to the center frequency.

2.1.5 Input Impedance and Reflection Coefficient

The input impedance of the antenna is "the impedance presented by an antenna at its terminals or the ratio of the voltage to current at a pair of terminals or the ratio of the appropriate components of the electric to magnetic fields at a point." Input impedance is of prime importance and helps

in determining the power radiated by the antenna. Considering only the input terminals of the antenna without any generator, the input impedance is given as

$$Z_A = R_A + X_A, \tag{2.5}$$

where R_A and X_A are the resistance and the reactance at the input terminals of the antenna. The resistance R_A comprises two parts i.e. radiation resistance R_r and the loss resistance R_L of the antenna. The radiation resistance is responsible for radiating the power received at the input terminals while the loss resistance dissipates power in the form of heat. If a generator with input impedance $Z_g = R_g + X_g$, with R_g as the resistance of the generator impedance and X_g as the reactance of the generator impedance (see Fig. 2.3), is attached to the input terminals of the antenna then the maximum power is transferred to the antenna under conjugate matching of the impedance. In conjugate matching, the resistance of both the antenna and the generator becomes equal while the reactances have opposite signs. Half of the maximum power is transferred to the antenna during impedance matching while half of the power is dissipated as heat by the generators resistance.

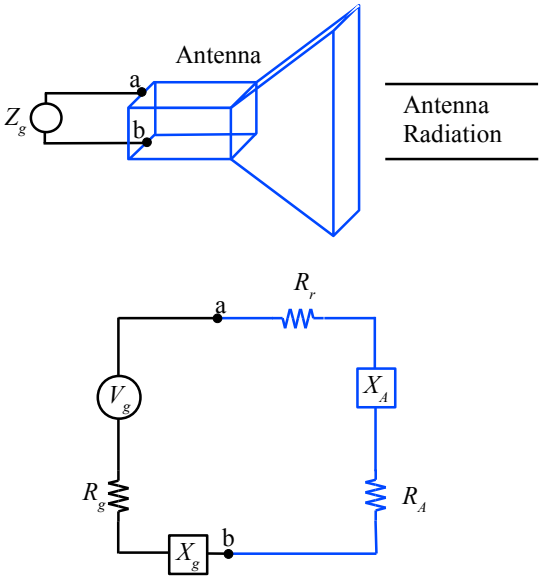

Figure 2.3: Representation of antenna input impedance and the generator impedance.

The reflection coefficient of an antenna is defined as the ratio of the amplitude of the reflected wave to the amplitude of the incident wave. In terms of impedance it can be written as

$$\Gamma_{\mathrm{A}} = \frac{Z_{\mathrm{A}} - Z_{\mathrm{L}}}{Z_{\mathrm{A}} + Z_{\mathrm{L}}}, \tag{2.6}$$

where Z_{A} and Z_{L} are the antenna impedance and the load impedance, respectively. In S-parameters formulation, the reflection coefficient is commonly denoted by S_{11} also known as input reflection coefficient. The reflection coefficient along with the input impedance can be characterised using a synthetic model of the antenna and using electromagnetic simulation software like FEKO [17] or CST [18]. In practical scenarios, vector network analyzers [19] are used to measure these factors.

2.2 Antenna Radiation Pattern Measurement Techniques

The field of an antenna is divided into three main regions i.e. reactive near field, radiating near field, and the far-field region [12], as shown in Fig. 2.4. The radiation field of the transmitting antenna can be predominantly reactive in the immediate space surrounding the antenna. The field components decays more rapidly than $1/r$, where r is the distance between the AUT and the observation point. The extent of this region is roughly $0 < r < \lambda_0/(2\pi)$, where λ_0 represents the wavelength. The radiating near-field region is bounded by $\lambda_0/(2\pi) < r < 2d^2/\lambda_0$ (approx.)

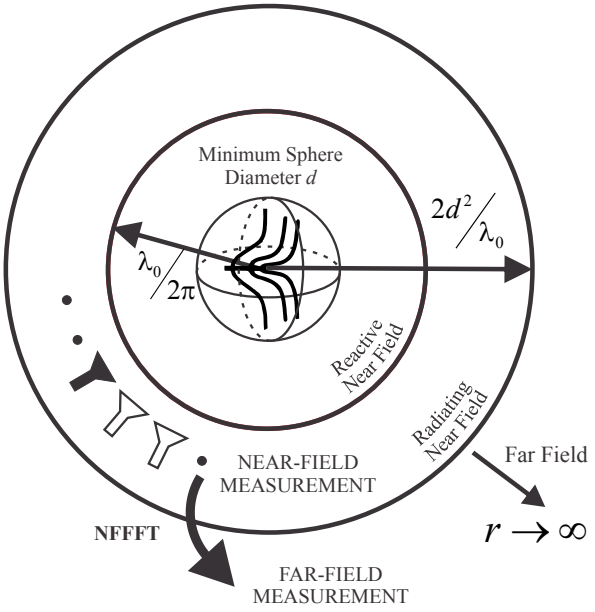

Figure 2.4: Antenna field regions.

and involves the diameter d of the minimum sphere enclosing the antenna. It is the region where the near-field measurements are performed as the mutual coupling between the AUT and the field probe is usually negligible. The radiation field starts decaying as $1/r$ near to the boundary of this region but the radiation pattern is dependent on r. The region is often referred to as "Fresnel zone". Beyond the near-field region i.e. $r > 2d^2/\lambda_o$, the radiation pattern is independent of r. The field in this region is known as the far field and is of most interest. Direct far-field measurements are performed in this region considering a maximum phase difference of $\pi/8$ between the center and the edge of the antenna for a spherical wavefront. For more accuracy larger separation between the AUT and the probe is usually desired.

2.2.1 Far-Field Measurements

Far-field measurements are the oldest and perhaps the most frequently used technique for determining the electromagnetic properties of the AUT. The radiation pattern of the AUT is directly measured in real time by the field probe placed at a distance greater than $2d^2/\lambda_o$. Quasi plane waves illuminate the probe at this distance (see Fig. 2.5) and therefore no probe correction is required.

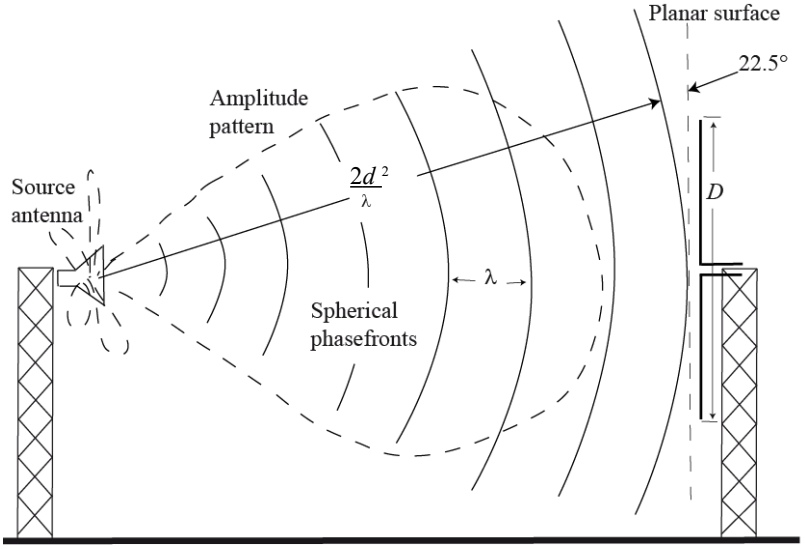

Figure 2.5: Principle of direct far-field antenna measurements.

The three major outdoor ranges include elevated ranges, slant ranges, and the reflection ranges [20]. The elevated range is suitable for areas with smooth terrain and requires a clear line-of-sight. In this configuration the source antenna and the test antenna are mounted at the same height. The directivity and the side lobe of the source antenna for the elevated range should be carefully selected in a way that the first null of the source pattern should be pointing towards the base of the test antenna. The elevated range, however, is prone to errors due to reflection of the antenna field from the ground. Slant ranges, on the other hand, do not suffer from pattern deterioration due to ground reflections and are more compact as compared to elevated ranges. In this configuration, the AUT is mounted on a non conducting tower while the sources antenna is fixed near the ground. The main beam of the source antenna is looking towards the AUT, as shown in Fig 2.6. In the ground reflection ranges, the height of source and test antennas and the distance between the two are adjusted in a way that the specular reflection from the ground has uniform phase and the amplitude distribution as that of the direct signal. The direct and the reflected signal interfere constructively provided the range surface is smooth. Since it is extremely difficult to have a very smooth outdoor surface, the reflection ranges are commonly used for measurements at lower frequencies.

Many modern devices require accurate results with very tight specifications which can only be achieved in controlled environments. The multipath propagation, weather conditions, real estate, electromagnetic interference, security concerns etc. are the major limitations which make these outdoor techniques unsuitable. However, far-field measurements can also be reliably carried out in controlled environments for small antennas.

2.2.2 Compact Range Measurements

The use of compact ranges is another effective way of determining the AUT radiation pattern in real time. Compact range measurements require a collimating surface for transforming the spherical wavefronts into planar ones in near field distance, as shown in Fig. 2.7. Collimating lenses can

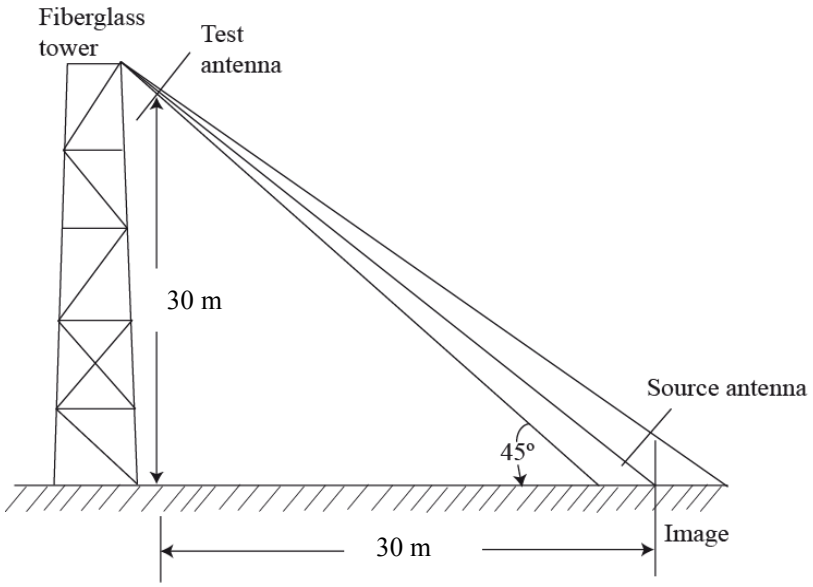

Figure 2.6: Far-field measurement setup for slant ranges.

also be used for this purpose. Due to smaller space requirements, the measurements using compact ranges are performed in a controlled environment. Therefore, higher accuracy as compared to direct outdoor far-field measurements can be achieved. The lower and the upper operational frequency is determined by the size and the surface accuracy of the reflector, respectively. A major drawback associated with compact antenna test ranges (CATR) are the high costs especially when dual curved reflectors or dual reflector compact ranges are used. The use of dual reflectors in compensated compact ranges (CCR) collimates the beam in two directions and helps to compensate the cross-polar component. The size of the required reflector increases when measurements at lower frequencies are desired which also increases the cost appreciably.

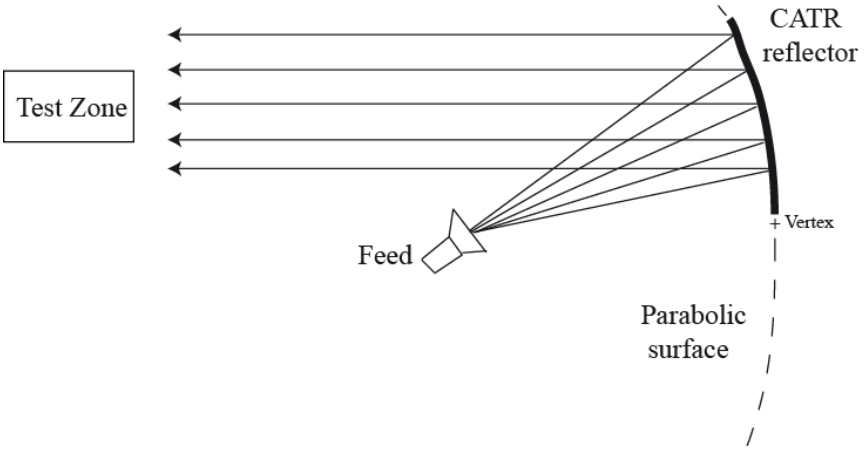

Figure 2.7: Principle of antenna measurement using compact ranges.

2.2.3 Near-Field Measurements

Near-field antenna measurements are a good alternative to space limited far-field measurements and expensive CATRs for standard antenna measurements. It involves the measurement of the radiating near-field of the AUT and post-processing the obtained near-field data using a suitable near-field far-field (NFFF) transformation algorithm. Like compact ranges, near-field measurements are carried out in a controlled environment and therefore offer higher accuracy. NFFF transformation algorithms make use of Huygens' principle which states that if the tangential field values are known on a closed test surface, the field outside the closed volume can be computed. This means that if the radiating object is replaced by the equivalent sources (as shown in Fig. 2.8) and the field distribution on a closed surface is computed, the measured near field can be used to determine the far field. Various equivalent sources can be used for reproducing the radiated AUT field and the choice of the equivalent sources ascertain the geometry of the near-field scanning surface. Planar, cylindrical, and spherical scanning surfaces are most commonly used and often make use of planar [22], cylindrical [24], and spherical [25] modal expansions, respectively. However, any other arbitrary surface can also be used [10], [2], [26] to measure the radiating near field of an AUT. Apart from the determination of the radiation pattern, near-field measurements can also be used to determine other antenna parameters like the gain of an antenna after NFFF transformation [27], [28].

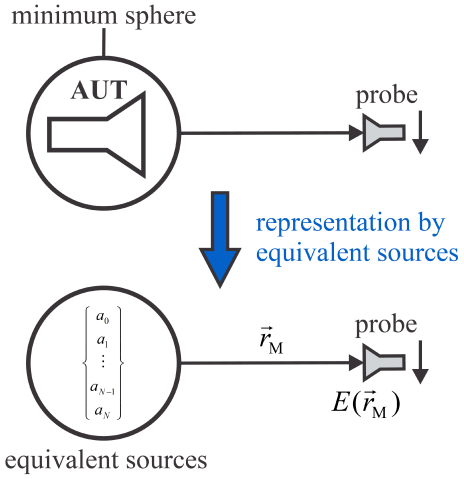

Figure 2.8: Representation of an antenna using equivalent sources.

The field probe in near-field measurements integrates the field around the measurement point r_M rather than measuring at a discrete point due to its finite extension [29], as shown in Fig. 2.9. The probe output can be represented as

$$U(\boldsymbol{r}_M) = \iiint_{V_{probe}} \boldsymbol{w}_{probe}(\boldsymbol{r}) \cdot \boldsymbol{E}(\boldsymbol{r})\, dV, \tag{2.7}$$

where V_{probe} is the volume and $\boldsymbol{w}_{probe}$ is the spatial weighting function of the probe. The effect of the probe must be considered during the transformation and is known as probe correction.

Near-field measurements have gained much importance in the last five decades due to increased accuracy, lower cost, controlled environment, antenna diagnostic capabilities [31], [32], [33], [34], [35], etc. Measurements of side lobe levels 50 dB below the maximum level have also been made

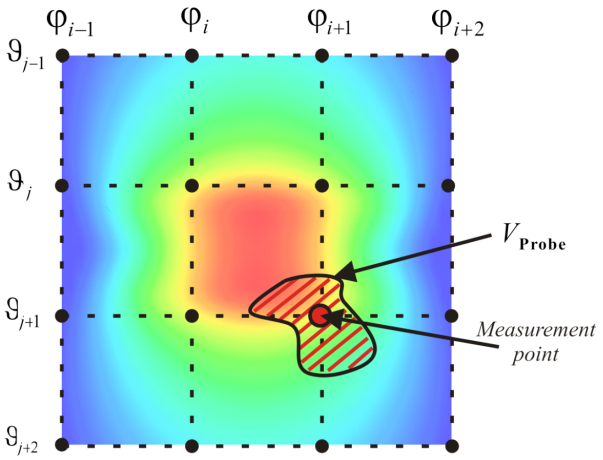

Figure 2.9: Measurement of electric near-field and probe output signal at discrete points [30].

possible using the same technique [36]. Maturely designed near-field measurement systems are already available [37], [38] and have been commonly employed at various test facilities [39], [40], [41], etc. However, the efficiency and effectiveness of near-field measurement techniques mainly depends on the accuracy of the obtained near field and the complexity of the NFFF transformation algorithm. In the following, we review the basics of near-field measurements on standard surfaces and their transformation into the far field.

Planar Near-Field Measurements:

Planar near-field measurement is, perhaps, the most simplified technique in terms of NFFF transformation. It is suitable for medium and high gain antennas. Measurements are performed on a finite scan plane placed at a suitable distance from the AUT. The AUT is normally fixed and the probe moves on a planar surface by stepping in one direction and sweeping in the orthogonal direction. High planarity is usually required and is of the order of $0.01\lambda_o$-$0.02\lambda_o$. Due to such strict requirements, highly sophisticated mechanical equipment is required which comprises cables, moving parts, receiver, etc. Commonly used planar scanners are either vertical or horizontal. In an ideal case, measurements on an infinite scan plane are desired. However, practical concerns such as the size of the scanner or the anechoic chamber limit the coverage area. Therefore, measurements are carried out until a certain boundary which limits the reliable region in the transformed far-field pattern as well. The boundary of the scan plane is normally chosen in a way that it provides less than -35 dB pattern level at edges so that the error in the transformed pattern can be reduced. The valid far-field angular region can be computed by using simple formulas which are already theoretically analyzed and experimentally validated [42]. Fig. 2.10 shows the setup of planar measurements with limited angular region in ϕ and θ. The valid angles

$$\phi_{\text{valid}} = \tan^{-1}\left(\frac{L_\phi - d_\phi}{2a}\right), \tag{2.8}$$

$$\theta_{\text{valid}} = \tan^{-1}\left(\frac{L_\theta - d_\theta}{2a}\right) \tag{2.9}$$

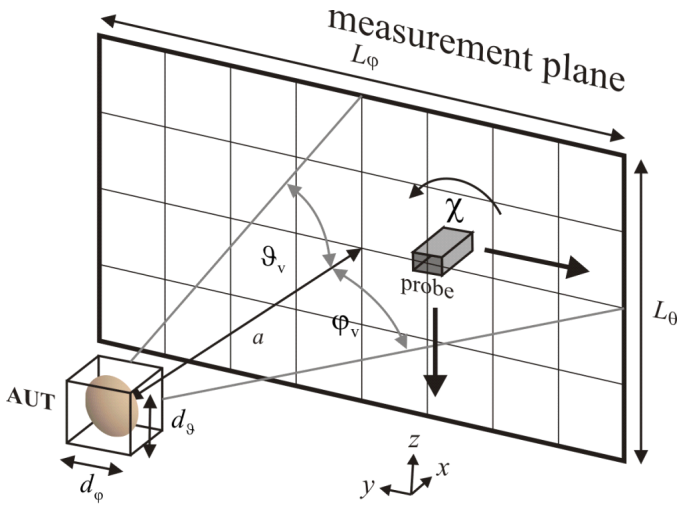

Figure 2.10: Planar near-field measurement setup with limited scan plane dimensions [42].

can be written in terms of the length L_θ and the width L_ϕ of the scan plane, where a is the separation between the AUT and the measurement surface and d_ϕ and d_θ are the dimensions of the AUT.

Another important consideration in planar measurements is that the probe does not always point towards the AUT. When shifted away from the AUT, the main signal of AUT can be received by a side lobe. However, when the probe faces the AUT, the main signal is received by the main beam of the probe, as shown in Fig. 2.11. Therefore, the probe signal should be correctly weighted by the radiation pattern of the probe.

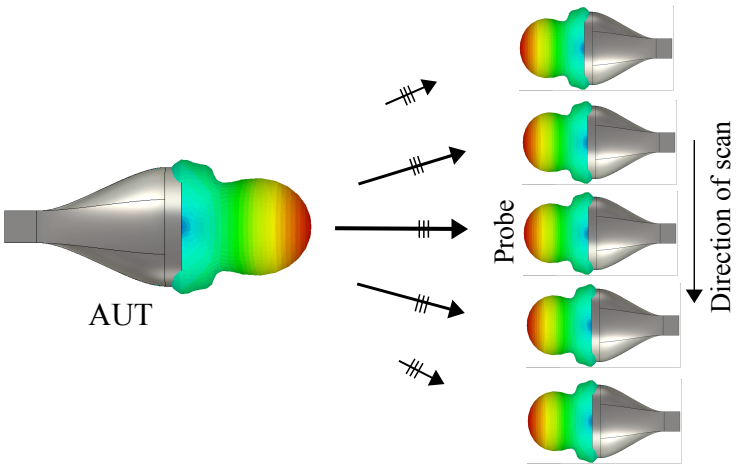

Figure 2.11: Probe influence in planar near-field antenna measurements.

The planar near-field transformation mostly makes use of plane waves for the expansion of radiated AUT fields. The transmission equation for planar measurements

$$U^{1,2}(\boldsymbol{P}) = F^{1,2}V_0 \iint \boldsymbol{t}_{10}(\boldsymbol{K}) \cdot \boldsymbol{s}_{02}^{1,2}(\boldsymbol{K}) e^{\mathrm{j}\gamma d} e^{\mathrm{j}\boldsymbol{K}\cdot\boldsymbol{P}} \mathrm{d}\boldsymbol{K} \tag{2.10}$$

relates the measured near-field data $U^{1/2}(\boldsymbol{P})$ in terms of transmitting parameter $\boldsymbol{t}_{10}(\boldsymbol{K})$ of the AUT and the receiving parameters $\boldsymbol{s}_{02}^{1}(\boldsymbol{K})$ and $\boldsymbol{s}_{02}^{2}(\boldsymbol{K})$ of two independent probes [22], as shown in Fig. 2.12. $\boldsymbol{P}$ is the transverse position vector at $z = d$ plane and V_0 is the input voltage of the AUT. F^1, F^2 are the impedance mismatch factors between the respective probes and the load port connected to the probes and are given as

$$F^1 = \frac{1}{1 - \Gamma_l \Gamma_p^1}, \quad F^2 = \frac{1}{1 - \Gamma_l \Gamma_p^2} \tag{2.11}$$

where Γ_l, Γ_p^1, and Γ_p^2 are the reflection coefficients of the load, the first probe, and the second probe, respectively. $\boldsymbol{K}$ is the transverse part of the propagation vector $\boldsymbol{k}$

$$\boldsymbol{K} = k_x\hat{x} + k_y\hat{y} = \boldsymbol{k} - \gamma\hat{z} \tag{2.12}$$

with γ representing the z-component of $\boldsymbol{k}$.

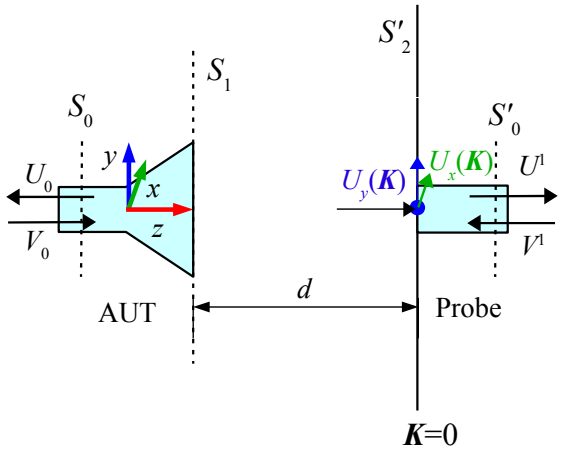

Figure 2.12: Scattering matrix representation for planar near-field measurements.

Fourier transform of the measured near-field data is performed to determine the angular spectra

$$D^{1,2}(\boldsymbol{K}) = \boldsymbol{t}_{10}(\boldsymbol{K}) \cdot \boldsymbol{s}_{02}^{1,2}(\boldsymbol{K}) = \frac{e^{-\mathrm{j}\gamma d}}{4\pi^2 F^{1,2} V_0} \iint U^{1,2}(\boldsymbol{P}) e^{-\mathrm{j}\boldsymbol{K}\cdot\boldsymbol{P}} \mathrm{d}\boldsymbol{P} \tag{2.13}$$

which can be written in the discrete form as

$$D^{1,2}(\boldsymbol{K}) = \frac{e^{-\mathrm{j}\gamma d}\delta x \delta y}{4\pi^2} \sum_m \sum_n U^{1,2}(x_m, y_n) e^{-\mathrm{j}(k_x x_m + k_y y_n)} \tag{2.14}$$

with proper sample spacing δx and δy in x and y direction, respectively. Probe correction can then be performed to obtain probe corrected "main" and "cross" components of AUT transmitting coefficients

$$t_{10\mathrm{m}}(\boldsymbol{K}) = \frac{\frac{D^1(\boldsymbol{K})}{s_{02\mathrm{m}}^1(\boldsymbol{K})} - \frac{D^2(\boldsymbol{K})}{s_{02\mathrm{c}}^2(\boldsymbol{K})} \rho_{\mathrm{s}}^1(\boldsymbol{K})}{1 - \frac{\rho_{\mathrm{s}}^1(\boldsymbol{K})}{\rho_{\mathrm{s}}^2(\boldsymbol{K})}}, \tag{2.15}$$

$$t_{10c}(\boldsymbol{K}) = \frac{\frac{D^2(\boldsymbol{K})}{s^2_{02c}(\boldsymbol{K})} - \frac{D^1(\boldsymbol{K})}{s^1_{02m}(\boldsymbol{K})\rho^2_s(\boldsymbol{K})}}{1 - \frac{\rho^1_s(\boldsymbol{K})}{\rho^2_s(\boldsymbol{K})}}, \tag{2.16}$$

where $\rho^1_s(\boldsymbol{K})$ and $\rho^2_s(\boldsymbol{K})$ are the polarization ratios of both orthogonal probes. The terms "main" and "cross" are chosen to denote two orthogonal components of vectors $\boldsymbol{t}_{10}$ or $\boldsymbol{s}_{02}$. The probes are chosen such that the first probe couples primarily to the m-component while the second probe couples to the orthogonal c-component. It should be noted that above relations are derived by considering negligible multiple reflections between the AUT and the probe. Once the AUT transmission coefficients are characterized, the electric far field of the AUT can be computed as [43]

$$\boldsymbol{E}_{\mathrm{FF}}(r, \boldsymbol{K}) = \frac{\mathrm{j}kV_0 e^{\mathrm{j}kr}}{r} \boldsymbol{t}_{10}(\boldsymbol{K}) \cos\theta. \tag{2.17}$$

Fig. 2.13 shows the schematic of a near-field far-field transformation for a medium gain horn antenna operating at 10 GHz.

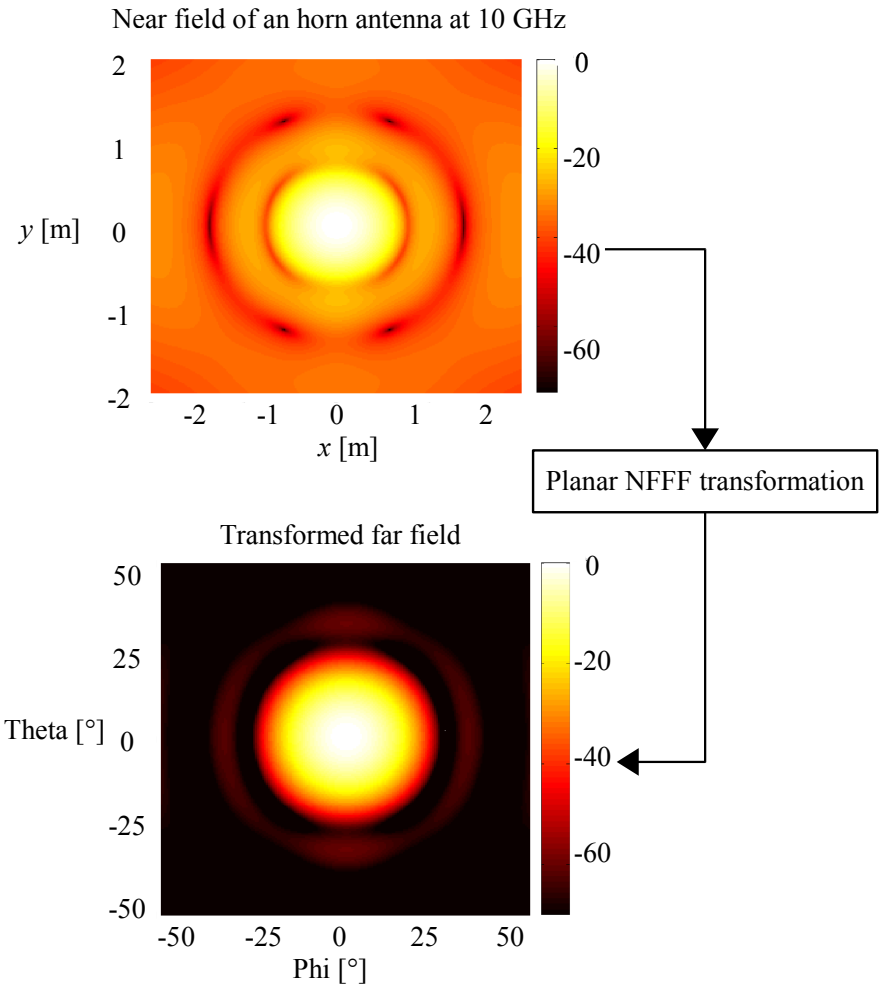

Figure 2.13: Planar near-field far-field transformation.

Cylindrical Near-Field Measurements:

Cylindrical near-field measurements are suitable for fan beam antennas having a broad beam in one plane and a narrow beam in the orthogonal plane. The NFFF transformation often makes use of a cylindrical modal expansion for representing the radiated AUT fields. Measurements are performed on a cylindrical surface by either sweeping the probe in a vertical direction (step in ϕ)(see Fig. 2.14) or by rotating the AUT in ϕ direction (step in vertical direction).

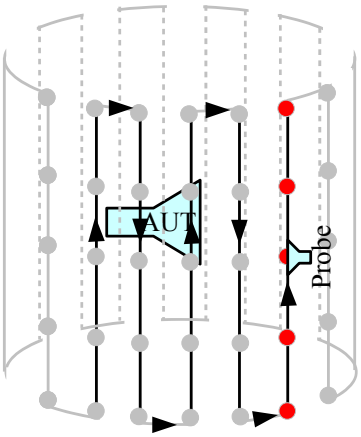

Figure 2.14: Cylindrical near-field measurement setup. The probe is moving in vertical direction while stepping in ϕ-direction.

Due to practical limitations, a cylindrical surface of finite height can be traversed by the probe. Therefore, truncated near field data is obtained which limits the transformed far-field to a certain valid region, similar to the planar case. The angular region is defined by

$$\theta_{\text{valid}} = \tan^{-1}\left(\frac{L_\theta - d_\theta}{2a}\right) \tag{2.18}$$

and

$$\phi_{\text{valid}} = \phi_{\text{t}} - \arcsin\left(\frac{\rho_0}{a}\right), \tag{2.19}$$

where a and L_θ are the radius and length of the cylindrical surface, respectively, while ρ_0 is the radius of the minimum cylinder enclosing the AUT. The diameter of the minimum cylinder enclosing the AUT is represented by d_θ and ϕ_{t} is the angle for the near-field measurement. The suitable size of the cylindrical measurement surface is chosen in relation with the truncation level of the near field at the edges. The commonly accepted value for the truncation level at the edges is -35 dB. Although performing measurements at a smaller distance from the AUT increases the SNR and the valid angular region but it also results in increased multiple reflections. Multiple reflections involve interactions of AUT and probe fields which results in the reflection of signals back and forth. This phenomenon is considered in more detail in coming chapters. Fig. 2.15 shows the variation in the valid angular region of a cylinder by varying the radius.

As stated earlier, the cylindrical NFFF transformation often makes use of a cylindrical modal expansion and the electric field is represented by superposition of the cylindrical waves. The

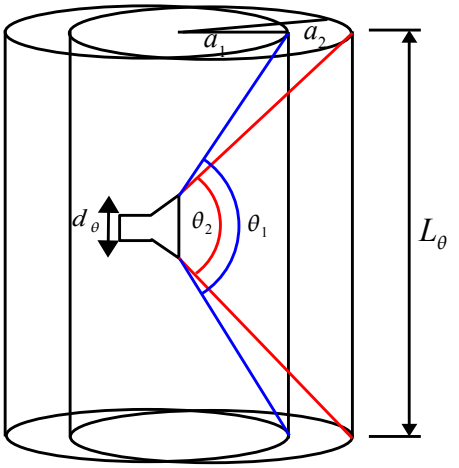

Figure 2.15: Representation of valid angle in cylindrical measurements.

transmission equation

$$U^{1,2}(\phi_0, z_0) = F^{1,2} V_0 \int_{-\infty}^{\infty} \sum_{n=-\infty}^{\infty} \sum_{s=1}^{2} R_n^{(1,2)s}(\gamma) T_n^s(\gamma) e^{\mathrm{j}n\phi_0} e^{\mathrm{j}\gamma z_0} \mathrm{d}\gamma \tag{2.20}$$

using scattering matrix theory [24] is derived, where $T_n^s(\gamma)$ and $R_n^{(1/2)s}(\gamma)$ are the AUT cylindrical wave transmitting coefficients and probe cylindrical receiving coefficients, respectively. The first probe data

$$I_n^1(\gamma) = \sum_{s=1}^{2} R_n^{1s}(\gamma) T_n^s(\gamma) = \frac{1}{4\pi^2 V_0} \int_{-\infty}^{\infty} \int_{0}^{2\pi} U^1(\phi_0, z_0) e^{-\mathrm{j}n\phi_0} e^{-\mathrm{j}\gamma z_0} \mathrm{d}\phi_0 \mathrm{d}z_0 \tag{2.21}$$

and the second probe data

$$I_n^2(\gamma) = \sum_{s=1}^{2} R_n^{2s}(\gamma) T_n^s(\gamma) = \frac{1}{4\pi^2 V_0} \int_{-\infty}^{\infty} \int_{0}^{2\pi} U^2(\phi_0, z_0) e^{-\mathrm{j}n\phi_0} e^{-\mathrm{j}\gamma z_0} \mathrm{d}\phi_0 \mathrm{d}z_0 \tag{2.22}$$

can be rewritten using Fourier series for n and Fourier integral for γ. For both vertical and horizontal polarization represented by s=1 and s=2 the probe data

$$I_n(\gamma) = \sum_{s=1}^{2} R_n^s(\gamma) T_n^s(\gamma) = R_n^1(\gamma) T_n^1(\gamma) + R_n^2(\gamma) T_n^2(\gamma) \tag{2.23}$$

can be reformulated to determine the AUT cylindrical wave transmitting functions

$$T_n^1(\gamma) = \frac{\frac{I_n^1(\gamma)}{R_n^{(1)1}(\gamma)} + \frac{I_n^2(\gamma)}{R_n^{(2)2}(\gamma)} \frac{R_n^{(1)2}(\gamma)}{R_n^{(1)1}(\gamma)}}{1 - \frac{R_n^{(1)2}(\gamma)}{R_n^{(1)1}(\gamma)} \frac{R_n^{(2)1}(\gamma)}{R_n^{(2)2}(\gamma)}} \tag{2.24}$$

and

$$T_n^2(\gamma) = \frac{\frac{I_n^2(\gamma)}{R_n^{(2)2}(\gamma)} + \frac{I_n^1(\gamma)}{R_n^{(1)1}(\gamma)} \frac{R_n^{(2)1}(\gamma)}{R_n^{(2)2}(\gamma)}}{1 - \frac{R_n^{(1)2}(\gamma)}{R_n^{(1)1}(\gamma)} \frac{R_n^{(2)1}(\gamma)}{R_n^{(2)2}(\gamma)}}. \tag{2.25}$$

Once the transmitting coefficients are characterised the far electric field is determined using

$$\boldsymbol{E}_{\mathrm{FF}}(\phi, \theta, r) = \frac{-2kV_0 \sin\theta e^{\mathrm{j}kr}}{r} \sum_{n=-\infty}^{\infty} (-\mathrm{j})^n \begin{bmatrix} T_n^1(k\cos\theta)\boldsymbol{e}_\phi \\ -\mathrm{j}T_n^2(k\cos\theta)\boldsymbol{e}_\theta \end{bmatrix} e^{\mathrm{j}n\phi}. \tag{2.26}$$

The near field of an elongated antenna operating at 3 GHz is measured and transformed using a cylindrical transformation for representation purposes, as shown in Fig. 2.16.

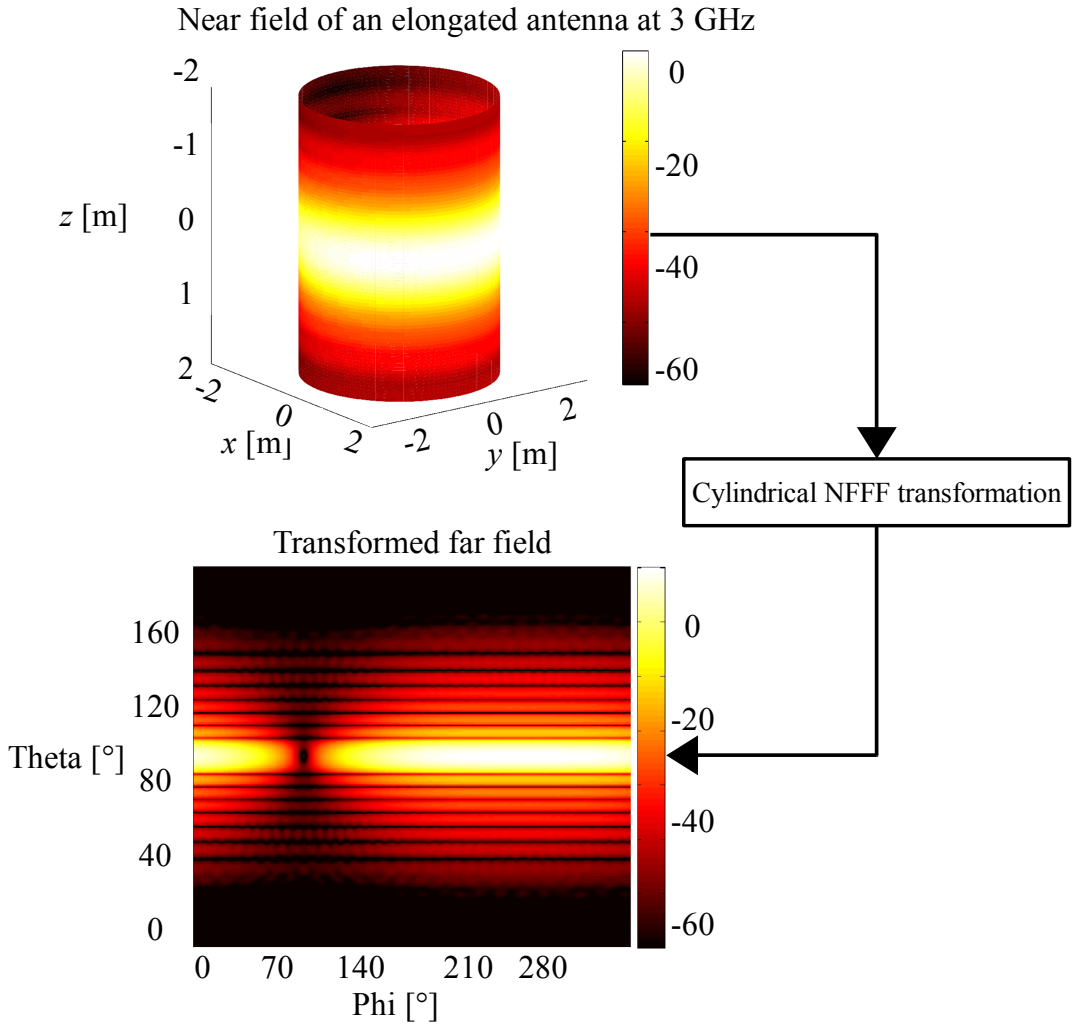

Figure 2.16: Cylindrical near field of an elongated antenna operating at 3 GHz processed using NFFF transformation and the transformed far-field.

Spherical Near-Field Measurements:

Spherical near-field antenna measurements are theoretically suitable for all kinds of antennas and often make use of spherical modes for reconstructing the radiated AUT field. The near field is

collected on a spherical surface by traversing the AUT in one direction (θ or ϕ) while stepping in the other direction (ϕ or θ). The probe is usually fixed and points towards the AUT, as shown in Fig. 2.17. The spherical near-field measurement is occasionally carried out on a non-closed surface

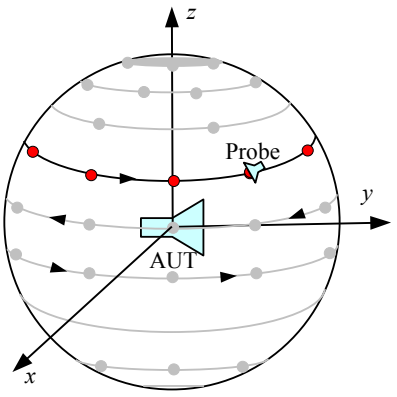

Figure 2.17: Spherical near-field measurement setup. The probe sweeps in ϕ-direction while stepping in θ-direction.

when the complete radiation pattern is not desired or due to practical limitations. Therefore, the reliable region in the transformed far-field is limited and can be determined by computing

$$\phi_{\text{valid}} = \phi_{\text{t}} - \arcsin\left(\frac{a}{d_{\text{s}}}\right) \tag{2.27}$$

and

$$\theta_{\text{valid}} = \theta_{\text{t}} - \arcsin\left(\frac{a}{d_{\text{s}}}\right), \tag{2.28}$$

where a and d_s are the radii of the minimum spheres enclosing the AUT and the measurement surface, respectively. θ_{t} and ϕ_{t} are angles for the near-field measurement, as shown in Fig. 2.18.

There are several possible ways of spherical near-field scanning. The most common scanning techniques involve ϕ over θ scanning, θ over ϕ scanning, and scanning using spherical arch roll. The AUT can be mounted on the scanner according to its design. Factors like gravity in space born antennas should be considered while mounting. The two possible ways include polar pointing and equator pointing. In θ scanning of a polar pointing setup, each scan passes through the aperture region and contributes to the aperture field. The signal is rapidly varying and therefore, high receiver bandwidth is required. The ϕ scanning, on the other hand, involves scanning within the aperture or outside the aperture with slowly varying signals. Similarly, in the equator pointing setup, θ and ϕ scanning involve some scans through the equator region with rapidly varying signal. Therefore, the spherical scanning setup is majorly dependent upon the design of the antenna, scan area of interest, and other practical limitations.

The spherical transmission equation

$$U(\phi,\theta,r,\chi) = \frac{1}{2}\sum_{\substack{smn\\ \sigma\mu\nu}} Q^{(3)}_{smn} e^{\mathrm{j}m\phi} d^{n}_{\mu m}(\theta) e^{\mathrm{j}\mu\chi} C^{sn}_{\sigma\mu\nu}(kr) R_{\sigma\mu\nu} \tag{2.29}$$

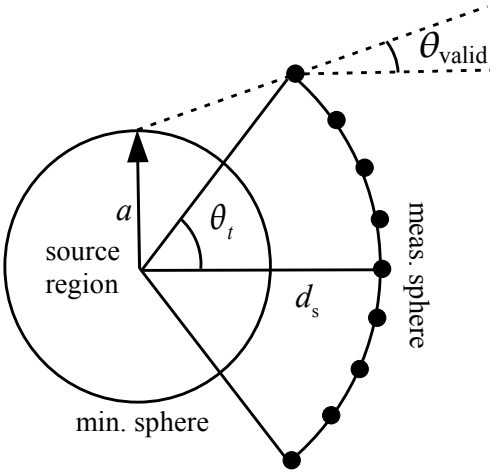

Figure 2.18: Cross-sectional view of spherical near field measurement surface truncation.

is formulated by considering spherical mode coefficients $Q^{(3)}_{smn} = V_0 T_{smn}$, where T_{smn} is the AUT spherical wave transmitting coefficient [25]. The other parameters used in the transmission equation represent

- $e^{\mathrm{j}m\phi} \rightarrow$ rotation of spherical wave function in ϕ
- $d^n_{\mu m}(\theta) \rightarrow$ rotation coefficient for rotation of spherical wave function in θ
- $e^{\mathrm{j}\mu\chi} \rightarrow$ rotation of spherical wave function in χ
- $C^{sn}_{\sigma\mu\nu}(kr) \rightarrow$ translation coefficient.

Full probe correction using the spherical transmission equation can be performed via matrix inversion and is computationally cumbersome [25]. To reduce the complexity, either first order or odd order probe correction [56] are normally applied. After a tedious mathematical analysis [43], [25] which employs Fast Fourier Transform, the transmitting behavior of the AUT is characterized and the electric far field

$$\boldsymbol{E}_{\mathrm{FF}}(\phi,\theta,r) = \sqrt{Z_{F0}}\frac{1}{\sqrt{4\pi}}\frac{e^{\mathrm{j}kr}}{r}V_0\sum_{smn} T_{smn}\boldsymbol{L}_{smn}(\phi,\theta) \tag{2.30}$$

can be represented using the far-field pattern function

$$\boldsymbol{L}_{smn}(\phi,\theta) = \lim_{kr\rightarrow\infty}\left[\sqrt{4\pi}\frac{e^{\mathrm{j}kr}}{r}\boldsymbol{F}^{(3)}_{smn}(\phi,\theta,r)\right], \tag{2.31}$$

where $\boldsymbol{F}_{smn}$ represents spherical wave functions. Fig. 2.19 shows the spherical near-field distribution of an horn antenna operating at 10 GHz along with the transformed far field processed using spherical NFFF transformation.

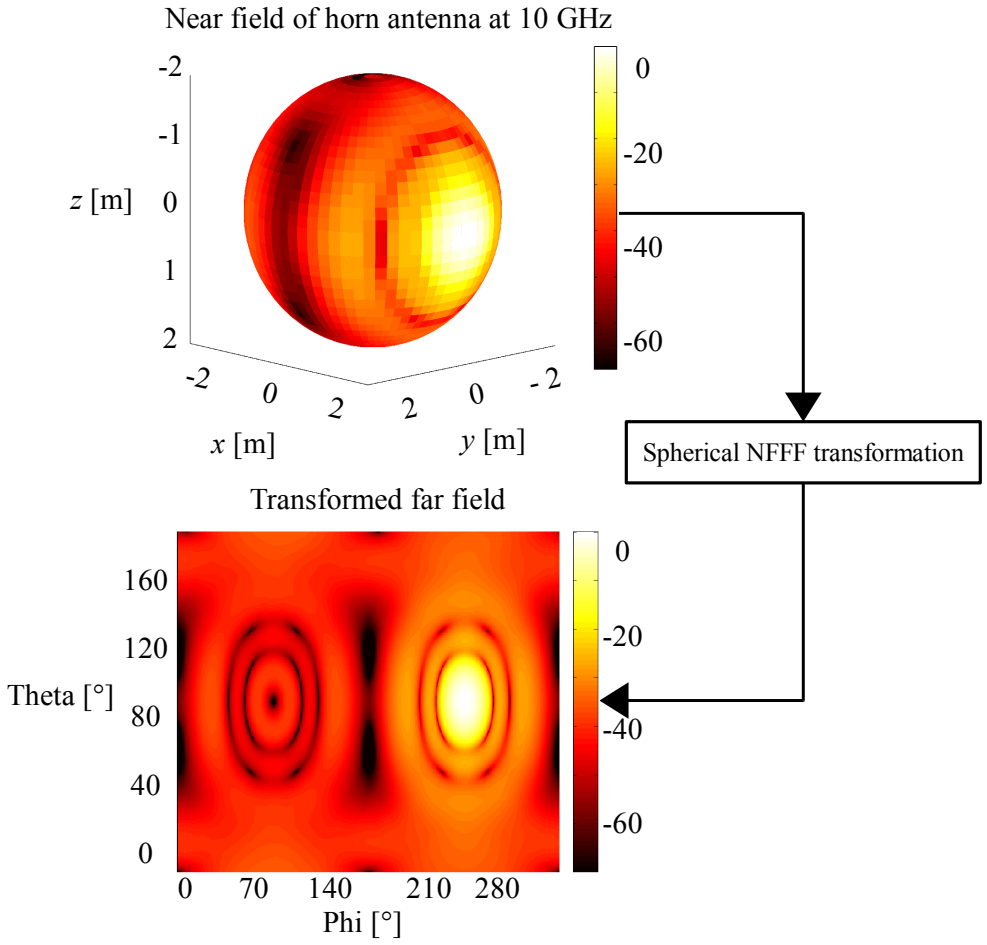

Figure 2.19: Representation of spherical near-field measurement of an horn antenna operating at 10 GHz and the transformed far-field pattern.

Arbitrary Near-Field Measurements

Near-field measurements can be performed on arbitrary surfaces as well but will required a suitable transformation algorithm. The use of 2D FFT in the traditional modal expansion based transformation techniques can not be utilized due to their limitation of using only canonical surfaces. Transformation techniques based on equivalent sources can, however, be utilized to post-process the near-field data collected on arbitrary grids. Equivalent sources like electric or magnetic currents [2],[3],[1],[52] or plane waves [10], [4] can be used to regenerate the radiation pattern of the AUT. These methods use Fast Multipole Method (FMM) like procedure to optimize the computational complexity of the algorithm which is further accelerated using Multilevel FMM [46]. Though the computational cost is still more than the FFT but advantages like full probe correction and the ability to process near-field data collected on arbitrary grids makes these techniques more attractive.

The fundamental principle of equivalent sources based transformation techniques is based on the fact that The AUT can be represented by an equivalent electric source current distribution $\boldsymbol{J}(\boldsymbol{r})$

and the resultant electric field

$$\boldsymbol{E}(\boldsymbol{r}) = \iiint\limits_{V_{\mathrm{AUT}}} \bar{\boldsymbol{G}}(\boldsymbol{r}, \boldsymbol{r}') \cdot \boldsymbol{J}(\boldsymbol{r}') dV' \tag{2.32}$$

is obtained by utilizing the volume of the AUT i.e. V_{AUT} and the dyadic Green's function of free space [48]

$$\bar{\boldsymbol{G}}(\boldsymbol{r}, \boldsymbol{r}') = -\mathrm{j}\frac{\omega\mu}{4\pi}\left(\bar{\boldsymbol{I}} + \frac{1}{k^2}\nabla\nabla\right)\frac{e^{-\mathrm{j}k|\boldsymbol{r}-\boldsymbol{r}'|}}{|\boldsymbol{r}-\boldsymbol{r}'|}. \tag{2.33}$$

The angular frequency ω, free space wavenumber k, and unit dyad $\bar{\boldsymbol{I}}$ are used in the computation of the Green's function. In the near-field region, the field probe takes the weighted average of the field around the measurement point and together with its receiving characteristics the output signal

$$U\left(\boldsymbol{r}_{\mathrm{M}}\right) = \iiint\limits_{V_{\mathrm{probe}}} \boldsymbol{w}_{\mathrm{probe}}\left(\boldsymbol{r}\right) \cdot \ \boldsymbol{E}\left(\boldsymbol{r}\right) dV \tag{2.34}$$

is acquired at the measurement point $\boldsymbol{r}_{\mathrm{M}}$. V_{probe} is the probe volume and $\boldsymbol{w}_{\mathrm{probe}}$ contains the spatial weighting function of the probe. In this way, the probe output and the field generated by the equivalent current sources can be related. Now the appropriate selection and distribution of the equivalent sources i.e. electric currents in this case will generate the same field as it is generated by the AUT. Once the equivalent sources have been characterized, the AUT field can be determined at any arbitrary distance.

It should be mentioned here that the MLFMM acceleration of the equivalent current method first requires generation of plane waves from the equivalent currents in order to perform the translations. The direct use of plane waves as equivalent sources avoids this mentioned step and also offers reduced computational complexity, thus making it an excellent choice for direct near-field transformation. In the next chapter, we revisit the essentials for plane wave based NFFF transformation.

Summarizing the discussion on near-field measurements, it has been seen that the standard transformation algorithms are based on scattering matrix theory of antenna-antenna interactions and employ FFT to compute the transmission coefficients of the AUT. Planar, cylindrical and spherical modal functions are used for representing the radiation characteristics and make use of canonical surfaces. The sample spacing required for acquiring near-field data on these surfaces is determined in a way to avoid aliasing errors. The aliasing errors become apparent if the sample spacing is lower than the Nyquist sampling criterion while using the FFT for the near-field transformation. The measurement industry is still reluctant to adopt NF transformation techniques which can transform the near-field data acquired on arbitrary measurement grids. Also, probe correction can get computationally inefficient if higher order probes are used.

Chapter 3

Fast Irregular Antenna Field Transformation Algorithm

In this chapter, a plane wave based near-field transformation technique which is also known as Fast Irregular Antenna Field Transformation Algorithm (FIAFTA) [10][4] is reviewed. The technique is derived from a spherical expansion of radiated AUT fields but the spherical modes are not directly used. Spherical modes are expanded into propagating plane waves using a similar procedure as described in the Fast Multipole Method (FMM) [46][47]. Therefore, the algorithm directly works with the far-field pattern of the AUT and translates the radiated plane waves of the AUT into incident plane waves at the probe. Afterwards, the far-field pattern of the probe can be directly used to weight the individual plane waves to obtain the probe output. In this unique way, full probe correction can be achieved in an efficient way in contrast to significant computational complexity required for higher order probes in classical transformation algorithms. Additionally, plane wave translations can be carried out to any arbitrary measurement grid with high efficiency after computing FMM translation operators. In the following, we review the essentials of FIAFTA.

As discussed in the Chap. 2, the electric field can be computed by utilizing equivalent electric source current distribution and the dyadic Green's function of free space. The probe output signal

$$U\left(\boldsymbol{r}_{\mathrm{M}}\right)=\iiint\limits_{V_{\mathrm{probe}}} \boldsymbol{w}_{\mathrm{probe}}\left(\boldsymbol{r}\right)\cdot\ \boldsymbol{E}\left(\boldsymbol{r}\right)dV \tag{3.1}$$

is acquired by considering spatial weighting function of the probe taking the weighted average of the field around the measurements point. The Gegenbauer's addition theorem is then used together with an expansion in propagating plane waves, as described in [46][47] to project the spatial integral into a spectral integral over the Ewald sphere according to

$$\boldsymbol{U}(\boldsymbol{r}_{\mathrm{M}})=-\mathrm{j}\frac{\omega\mu}{4\pi}\iint T_L(\hat{k},\boldsymbol{r}_{\mathrm{M}})\bar{\boldsymbol{P}}(\hat{k},\hat{r}_{\mathrm{M}})\cdot(\bar{\boldsymbol{I}}-\hat{k}\hat{k})\cdot\tilde{\boldsymbol{J}}(\hat{k})d\hat{k}^2, \tag{3.2}$$

where $\bar{\boldsymbol{P}}(\hat{k},\hat{r}_{\mathrm{M}})$ contains the far-field pattern of the probe for probe correction, $(\bar{\boldsymbol{I}}-\hat{k}\hat{k})\cdot\tilde{\boldsymbol{J}}(\hat{k})$ are the equivalent plane wave sources, and $T_L(\hat{k},\boldsymbol{r}_{\mathrm{M}})$ is the translation operator known from FMM [46]. Unlike the classical plane wave based approaches for planar scan surfaces, the subjected FIAFTA technique utilizes the complete Ewald sphere of propagating plane waves. Fig. 3.1 shows the plane wave representation of the AUT and the probe along with the translation of plane waves from the AUT to the field probe employing the translation operator $T_L(\hat{k},\boldsymbol{r}_{\mathrm{M}})$. The translation operator

$$T_L(\hat{k},\boldsymbol{r}_{\mathrm{M}})=-\mathrm{j}\frac{k}{4\pi}\sum_{l=0}^{L}\left(-\mathrm{j}\right)^l\left(2l+1\right)\mathrm{h}_l^{(2)}\left(kr_{\mathrm{M}}\right)\mathrm{P}_l(\hat{k}\cdot\hat{r_{\mathrm{M}}}), \tag{3.3}$$

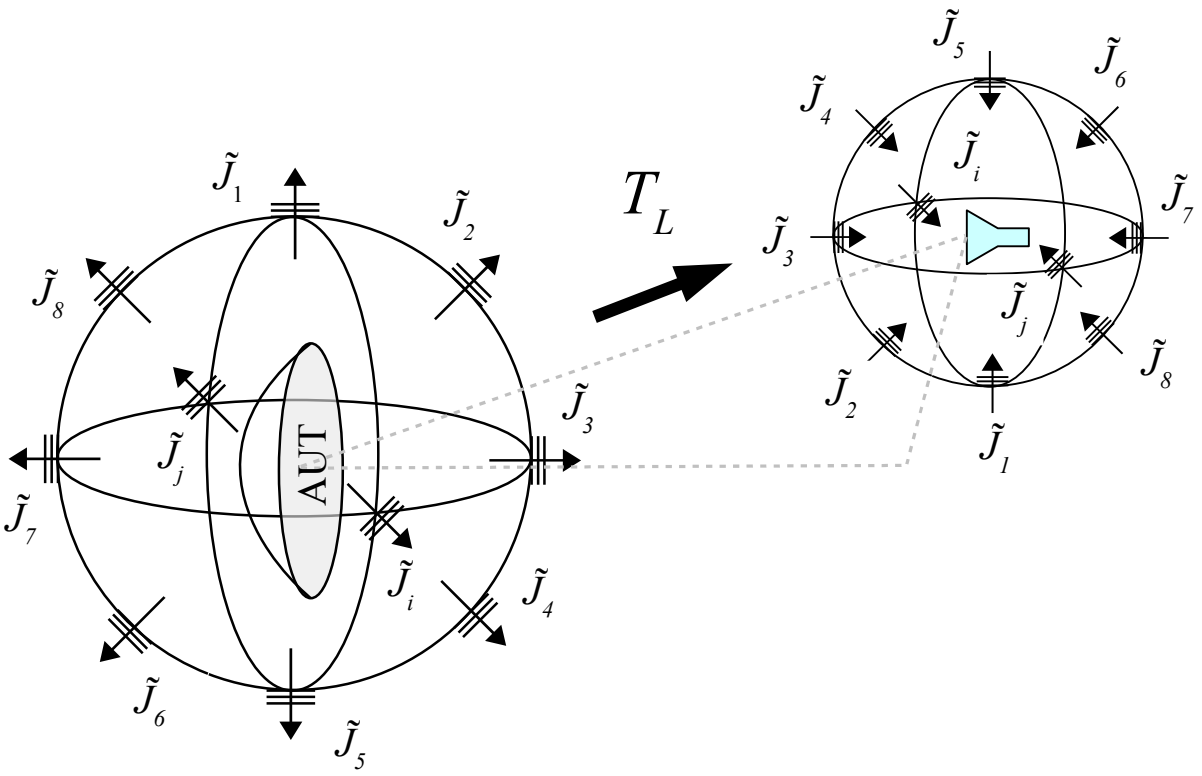

Figure 3.1: Equivalent plane wave sources representing AUT field and their translation to field probe by employing translation operator T_L.

simply converts the radiating plane waves from the AUT to the incident plane waves at the field probe residing at observation point $\boldsymbol{r}_{\mathrm{M}}$, where $\mathrm{h}_l^{(2)}$ is the spherical Hankel function of second kind and P_l is a Legendre polynomial. The multipole order L for the diagonal translation operator is dependent on the electrical size of the AUT and of the probe [50].

Two orthogonal polarizations of radiated AUT fields are commonly required [49]. Therefore, two complex voltages are introduced and the spectral integral over the Ewald sphere is evaluated by numerical quadrature [46] with discrete representation according to

$$\begin{aligned} U^{1,2}\left(\phi_m, \theta_n, r_{\mathrm{M}}\right) = -\mathrm{j}\frac{\omega\mu}{4\pi} \sum_{k_\phi} \sum_{k_\theta} T_L(\hat{k}, \boldsymbol{r}_{\mathrm{M}}) W(k_\theta) \\ P^{1,2}\left(k_\phi, k_\theta, \phi_m, \theta_n\right) \cdot (\bar{\boldsymbol{I}} - \hat{k}\hat{k}) \cdot \tilde{\boldsymbol{J}}\left(k_\theta, k_\phi\right), \end{aligned} \tag{3.4}$$

where $W(k_\theta)$ is a weighting factor. For several measurement poinst, it is possible to set up a linear system of equations

$$\boldsymbol{U}' = -\mathrm{j}\frac{\omega\mu}{4\pi} ||C|| \cdot \tilde{\boldsymbol{J}}' \tag{3.5}$$

from the discrete representation. The measured voltage vector

$$\boldsymbol{U}' = \begin{pmatrix} U^1(\phi_1, \theta_1, r_M) \\ . \\ . \\ . \\ U^1(\phi_M, \theta_N, r_M) \\ \hline U^2(\phi_1, \theta_1, r_M) \\ . \\ . \\ . \\ U^2(\phi_M, \theta_N, r_M) \end{pmatrix} \tag{3.6}$$

and the plane wave amplitudes of the AUT

$$\tilde{\boldsymbol{J}}' = \begin{pmatrix} \tilde{J}_\phi(k_{\phi 1}, k_{\theta 1}) \\ \tilde{J}_\theta(k_{\phi 1}, k_{\theta 1}) \\ . \\ . \\ . \\ \tilde{J}_\phi(k_{\phi P}, k_{\theta Q}) \\ \tilde{J}_\theta(k_{\phi P}, k_{\theta Q}) \end{pmatrix} \tag{3.7}$$

are related with the coupling matrix

$$||C|| = \begin{pmatrix} C_\phi^1(k_{\phi 1}, k_{\theta 1}, \phi_1, \theta_1) & . & . & . & C_\theta^1(k_{\phi P}, k_{\theta Q}, \phi_1, \theta_1) \\ . & & . & & . \\ . & & . & & . \\ . & & & . & . \\ C_\phi^1(k_{\phi 1}, k_{\theta 1}, \phi_M, \theta_N) & . & . & . & C_\theta^1(k_{\phi P}, k_{\theta Q}, \phi_M, \theta_N) \\ \hline C_\phi^2(k_{\phi 1}, k_{\theta 1}, \phi_1, \theta_1) & . & . & . & C_\theta^2(k_{\phi P}, k_{\theta Q}, \phi_1, \theta_1) \\ . & & . & & . \\ . & & . & & . \\ . & & & . & . \\ C_\phi^2(k_{\phi 1}, k_{\theta 1}, \phi_M, \theta_N) & . & . & . & C_\theta^2(k_{\phi P}, k_{\theta Q}, \phi_M, \theta_N) \end{pmatrix} \tag{3.8}$$

in the system of linear equations. The coupling matrix elements are given as:

$$C_{\phi,\theta}^{1,2}(k_{\phi p}, k_{\theta q}, \phi_m, \theta_n) = T_L(\hat{k}, \hat{r}_M) W(k_{\theta q}) P_{\phi,\theta}^{1,2}(k_{\phi p}, k_{\theta q}, \phi_m, \theta_n), \tag{3.9}$$

where

- m = 1,...,M: no. of observation points (ϕ-direction),
- n = 1,...,N: no. of observation points (θ-direction)
- p = 1,...,P: no. of integration points (ϕ-direction),
- q = 1,...,Q: no. of integration points (θ-direction).

The equation system is solved by employing the Generalized Minimum Residual Solver (GMRES) [51] in a least mean square sense (LMS) [77] as

$$\|C\|^H \cdot \boldsymbol{U}' = -\mathrm{j}\frac{\omega\mu}{4\pi} \|C\|^H \cdot \|C\| \cdot \tilde{\boldsymbol{J}}', \tag{3.10}$$

where $\|C\|^H$ is the complex conjugate transpose of the coupling matrix. It is worth mentioning here that the coupling matrix $\|C\|$ is typically not explicitly computed. It is rather constructed in an on-the-fly manner. Once the plane wave spectrum has been obtained, the AUT is completely characterized and the field values at any arbitrary distance can be evaluated. The residuum of the GMRES solver

$$\tau = \frac{\text{norm}(\|C\|^H \|C\| \tilde{\boldsymbol{J}}'_{\text{final}} - \|C\|^H \boldsymbol{U}')}{\text{norm}(\|C\|^H \boldsymbol{U}')} \tag{3.11}$$

determines the relative residual error during the computation while the near-field error

$$\epsilon = \text{norm}(\tilde{\boldsymbol{J}}'_{\text{final}} - \|C\|^H \boldsymbol{U}') \tag{3.12}$$

helps in determining that how well the radiated fields of the equivalent plane wave sources reproduce the given near-fields.

For enhanced computational complexity, near-field measurement points are grouped together to form a hierarchical structure similar to the Multilevel Fast Multipole Method (MLFMM) [47] as described in [4]. The grouping of measurement points in an hierarchical structure decreases the complexity from $O(N^2)$ to $O(N \log N)$, where N is the number of measurement points. Field translations can now be carried out on the coarsest level contrary to the single level case. The plane wave spectra

$$\tilde{\boldsymbol{J}}_N^{i_N}\left(\hat{k}\right) = T_L\left(\hat{k}, \boldsymbol{r}_{\text{box}}\right)\left(\bar{\boldsymbol{I}} - \hat{k}\hat{k}\right) \cdot \tilde{\boldsymbol{J}}\left(\hat{k}\right), \tag{3.13}$$

are received at the highest level boxes i_N and are processed using disaggregation and anterpolation to the lower levels as shown in Fig. 3.2. The combined anterpolation and disaggregation operator

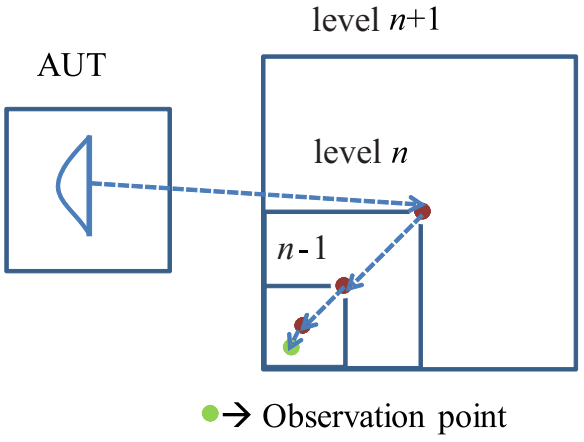

Figure 3.2: Cross-section of hierarchical multilevel measurement setup.

$\bar{\boldsymbol{D}}_n^{i_n}\left(\boldsymbol{k}, \boldsymbol{r}_n^{i_n}\right)$ is used in

$$\tilde{\boldsymbol{J}}_n^{i_n}\left(\hat{k}\right) = \bar{\boldsymbol{D}}_n^{i_n}\left(\boldsymbol{k}, \boldsymbol{r}_n^{i_n}\right) \cdot \left(\bar{\boldsymbol{I}} - \hat{k}\hat{k}\right) \cdot \tilde{\boldsymbol{J}}_{n+1}^{i_{n+1}}\left(\hat{k}\right) \tag{3.14}$$

for the recursive operation and to obtain the plane wave spectra at the lower level box center i_n. Disaggregation implies a phase shift from coarser to finer level box centers until the measurement point is reached while anterpolation is an adjoint operation of interpolation and is used for reducing the sampling rate, as explained in [4]. After the completion of the disaggregation and anterpolation process, the probe output

$$\boldsymbol{U}\left(\boldsymbol{r}_{\mathrm{M}}\right) = -\mathrm{j}\frac{w\mu}{4\pi}\sum_{\hat{k}} \boldsymbol{W}\left(\hat{k}\right) e^{-\mathrm{j}\tilde{\boldsymbol{r}}_{\mathrm{M}}\cdot\boldsymbol{k}} \bar{\boldsymbol{P}}\left(\hat{k}, \hat{r}_{\mathrm{M}}\right) \cdot \left(\bar{\boldsymbol{I}} - \hat{k}\hat{k}\right) \cdot \tilde{\boldsymbol{J}}_0^{i_0}\left(\hat{k}\right) \tag{3.15}$$

is obtained by utilizing the probe correction coefficient. Gauss-Legendre quadrature is used for the evaluation of the integrals along with the corresponding weight factors $\boldsymbol{W}\left(\hat{k}\right)$ and the algorithm is implemented in an iterative manner using the Generalized Minimum Residual Solver (GMRES) [51] in an on-the-fly manner.

FIAFTA has already been verified using simulations as well as using measurement data [4]. However, an employment of FIAFTA in the antenna measurement industry requires a more rigorous analysis to determine its performance maturity. The behavior of FIAFTA against measurement errors must be determined to find out how robust FIAFTA is against these errors. Therefore, in the following chapters the error behavior of FIAFTA against measurement errors is thoroughly investigated and is compared to the traditional transformation techniques.

Chapter 4

Comparative Planar Near-Field Measurement Error Analysis

The development of FIAFTA opened new possibilities of using a sole algorithm for the standard as well as arbitrary near-field measurement grids. The reduced computational complexity makes it suitable for electrically large antennas and above all full probe correction can be achieved for any arbitrary grid without any major increase in the complexity. It is emphasized here that transformation techniques employing equivalent current sources e.g. [1], [2], [3], [52], etc. can also handle measurements on arbitrary grids and with arbitrary probes but with bad numerical complexity and they will require huge computation times for large problems. The available computational complexity of integral equation based approaches utilizing equivalent currents is $O((ka)^4)$, where k is the wavenumber and a is the radius of the minimum sphere enclosing the AUT. The multilevel fast multipole method (MLFMM) acceleration reduces the computational cost to $O((ka)^2\log(ka)^2)$, as reported in [53] and [54]. However, the MLFMM acceleration of the equivalent current method first requires generation of plane waves from the equivalent currents in order to perform the translations. The direct use of plane waves as equivalent sources avoids this mentioned step and also offers reduced computational complexity i.e. $O((ka)^2\log(ka)^2)$, thus making it an excellent choice for direct near-field transformation. Other economical approaches may involve a recently proposed spherical NFT [55] which takes higher order probe correction into account and makes use of a renormalized least square approach in two ways. It either applies an iterative approach using conjugate gradient method or a normal method where the matrix is inverted explicitly. In both cases, $O((ka)^3)$ complexity with little overhead is observed. Nevertheless, along with higher computational cost, the approach is only applicable to spherical grids. Spherical $1^{\text{st}}/3^{\text{rd}}$ order probe correction reported in [56] can also be achieved with $O((ka)^3)$ computational complexity but with an additional probe orientation, which requires more measurement time. Table 4.1 summarizes the complexities of near-field transformation algorithms providing economical computational cost.

As stated earlier, apart from the computational cost, the behavior of FIAFTA against measurement errors along with its comparison with already established techniques is essentially required to determine its performance maturity. Therefore, this is the main focus of this chapter. Planar near-field measurement errors are generated individually in a realistic manner and their exclusive effect on the transformed far-field is determined. The error behavior is then compared with the traditional planar transformation technique employing 2D FFT.

In practice, several measurement and environmental errors occur during near-field measurements whose effect is carried in the transformation and, therefore, cause errors in the resulting radiation pattern. It is extremely important for an accurate measurement to identify the individual

Table 4.1: Complexity of Near-Field Transformation Algorithms

Algorithm	**Complexity**
Multilevel plane wave based NFT	$O((ka)^2\log(ka)^2)$
Spherical NFT with higher order probes [55]	$O((ka)^3)$
Equivalent electric current based NFT [2]	$O((ka)^4)$
Spherical $1^{st}/3^{rd}$ order probe correction [56]	$O((ka)^3)$
Planar scanning with arbitrary probe	$O((ka)^2\log(ka)^2)$

sources of errors and their exclusive effect on the far-field pattern of the AUT. An error model consisting of 18 errors is defined by the National Institute of Standards and Technology (NIST) (formerly called National Bureau of Standards) for planar near-field measurements [42]. The planar measurement errors are classified into three major categories i.e. general errors [1], instrumentation errors [2], and probe parameter errors [3][4] according to the way they influence the near field. All the errors are generated in a realistic manner using the measurement equipment specifications and are introduced in the near-field data which is synthetically generated using electric dipoles. Using the synthetic data approach, the effect of most of the measurement errors can be analyzed without the influence of other errors. It helps in determining the sensitivity of the transformed radiation pattern against the specific measurement error. Thus, a more reliable error estimate in the actual far-field pattern can be achieved. The perturbed near-field is then processed using both 2D FFT based approach and FIAFTA.

4.1 Synthetic Antenna Modeling

The AUT used in the error analysis is a synthetically modeled electrically large (64λ) parabolic reflector operating at 40 GHz. Electric dipoles are used to model the AUT using a proper magnitude profile and geometrical arrangement of electric dipoles, as described in [60]. The dipole distribution is shown in Fig. 4.1. The dipoles are distributed in two different planes separated by $\lambda/4$ distance. Additionally, 90° phase difference between the dipoles of the two planes produces the antenna field only in the forward direction. The arrow thickness represents the magnitude and the phase information is provided by the arrow color. The dipoles are arranged in concentric equidistant circles with exponential decay in the magnitude from inner to the outer circle. The magnitude, however, remains the same within one circle. The antenna aperture is 0.48 m. The cumulative fields of all source dipoles determine the electric field

$$\boldsymbol{E}\left(\boldsymbol{r}_{\mathrm{M}}\right) = -\mathrm{j}\frac{w\mu}{4\pi}\sum_{i=1}^{i_{\mathrm{AUT}}}\left(\tilde{\boldsymbol{I}} + \frac{1}{k^2}\nabla\nabla\right)\cdot\boldsymbol{d}_i\frac{e^{-\mathrm{j}k\left|\boldsymbol{r}_{\mathrm{M}}-\boldsymbol{r}_{\mathrm{d,i}}\right|}}{\left|\boldsymbol{r}_{\mathrm{M}}-\boldsymbol{r}_{\mathrm{d,i}}\right|}, \tag{4.1}$$

at the measurement point r_{M} by evaluating the Green's function of free space, whereas $\boldsymbol{r}_{\mathrm{d},i}$ represents the position of source dipoles and $\boldsymbol{d}_i$ represents their complex amplitude and orientation.
The near-field of the parabolic reflector is collected on the *xz*-plane placed at $y = -2$ m, as shown in Fig. 4.2.

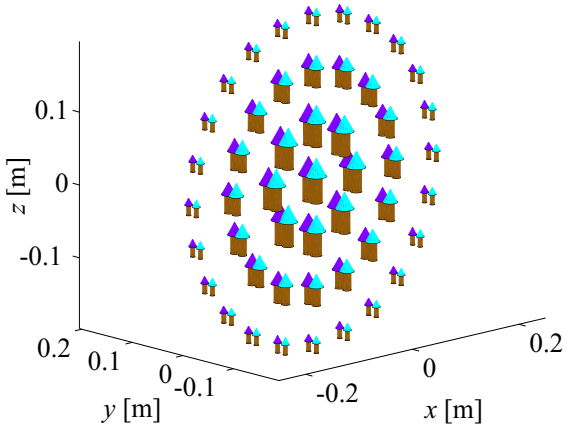

Figure 4.1: Electric dipole distribution synthesizing a 40 GHz parabolic reflector. The size and the color of the dipoles represent magnitude and phase information, respectively.

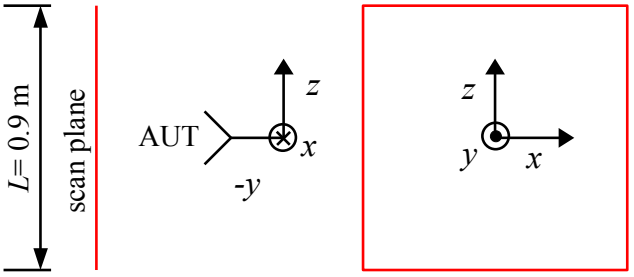

Figure 4.2: Planar near-field measurement setup.

With a similar modeling of the probe like the AUT, the probe signal

$$U(\boldsymbol{r}_{\mathrm{M}}) = \sum_{i=1}^{i_{\mathrm{probe}}} \boldsymbol{E}(\boldsymbol{r}_{\mathrm{M}} - \boldsymbol{r}_{\mathrm{p},i}) \cdot \boldsymbol{p}_i \tag{4.2}$$

is received by the probe dipoles, as shown in Fig. 4.3. As can be seen, the probe output is just a superposition of electric fields received by various probe dipoles constituting a more realistic probe. The resulting orthogonal near-field distributions i.e. containing $\boldsymbol{e}_{\mathrm{x}}$ and $\boldsymbol{e}_{\mathrm{z}}$ components using above mentioned arrangements are shown in Fig. 4.4.

4.2 Planar Near-Field Measurement Errors

In this section, the error behavior of FIAFTA against planar near-field measurement errors is described. The effect of each individual error is discussed[1] assuming all the other errors either zero or having negligible effect on the transformed pattern due to utilization of the synthetic data. It is

[1]The effect of measurement area truncation error is inevitable and will be inherent in the analysis.

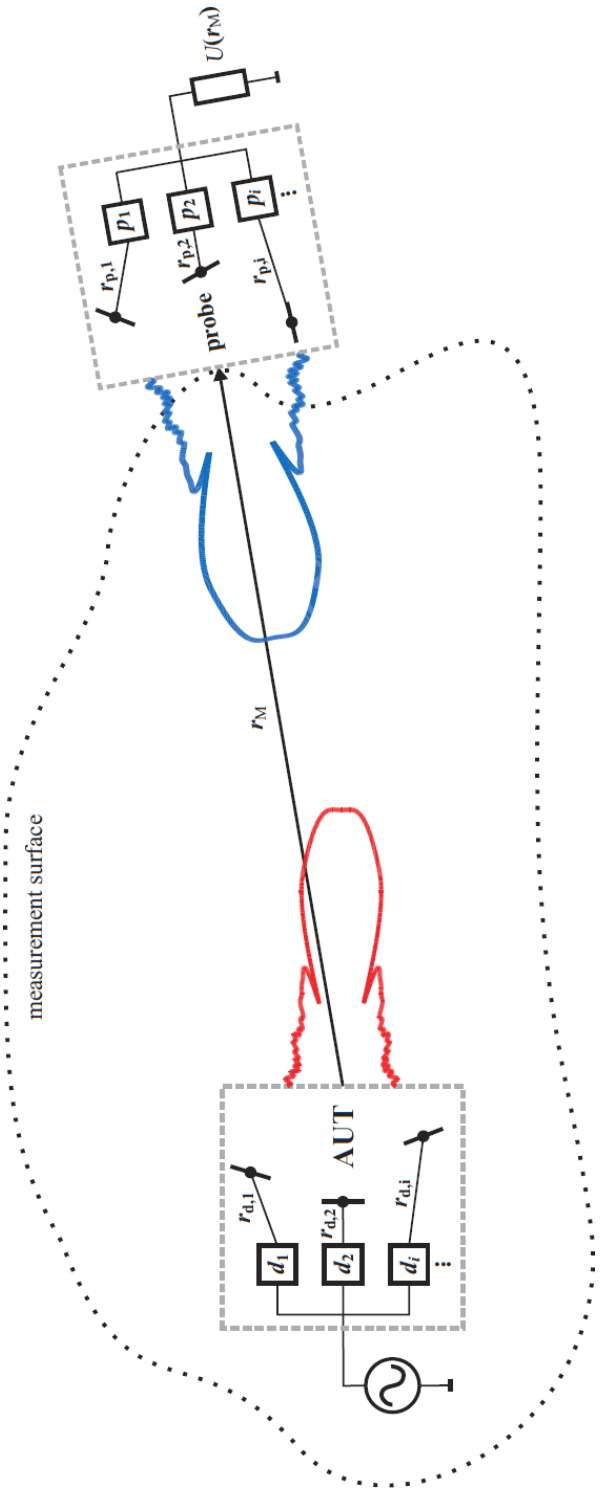

Figure 4.3: Near-field data collection using electric dipole distribution [60].

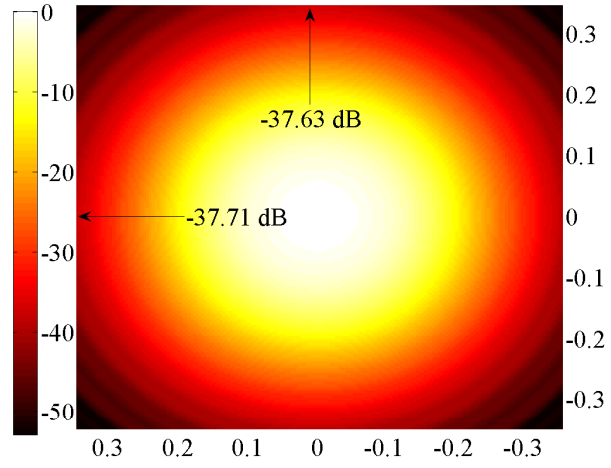

(a)

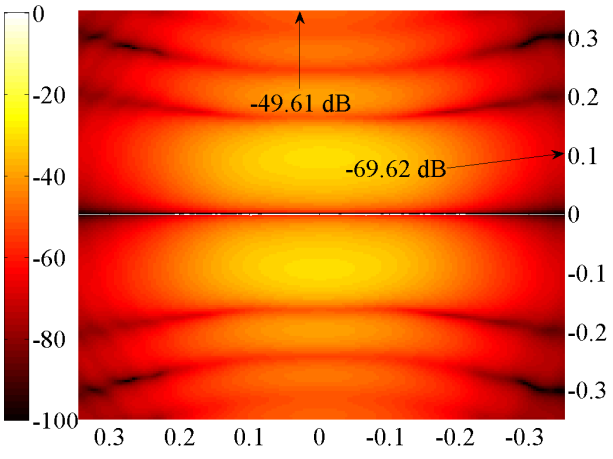

(b)

Figure 4.4: Near field $\boldsymbol{e}_{\mathrm{x}}$ (a) and $\boldsymbol{e}_{\mathrm{z}}$ (b) distribution [dB] of parabolic reflector operating at 40 GHz.

important to mention that the accuracy of the transformed pattern can be controlled via parameters[2] like residuum of the iterative GMRES solver, number of box levels, grouping scheme, etc. However, better accuracy also results in increased runtime. The following parameter values are used for all transformations

- Residuum = 0.000034,
- AUT multipole number = 219,
- Number of box levels = 4.

4.2.1 General Errors

Scan Area Truncation

The finite scan plane is one of the unavoidable sources of error in planar measurements and limits the reliability of the radiation pattern to a certain angular region bounded by

$$\theta_{\text{valid}} = \tan^{-1}\left(\frac{L_\theta - d}{2s}\right) \tag{4.3}$$

$$\phi_{\text{valid}} = \tan^{-1}\left(\frac{L_\phi - d}{2s}\right), \tag{4.4}$$

where L_ϕ and L_θ are the length and the width of the scan plane, respectively, and s is the separation between the AUT and the measurement surface. A cross-sectional view of the scan plane is shown in Fig. 4.5 for the reliable region in θ-direction. Equations (4.3) and (4.4) are both theoretically

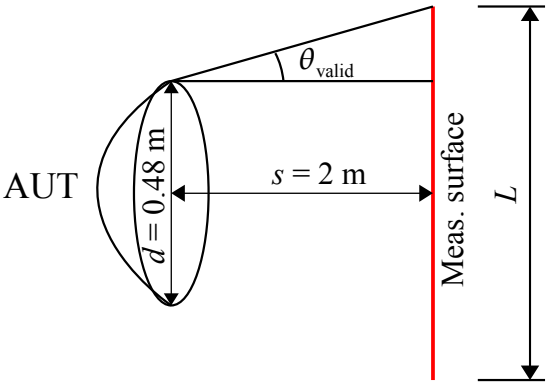

Figure 4.5: Measurement area truncation.

analyzed and validated by extensive measurements conducted by NIST [61][62]. The near-field discontinuity due to a finite scan plane introduces errors within the valid region as well. To estimate the error, the near field is computed on different square shaped scan planes with side lengths 0.5 m, 0.6 m, 0.7 m, 0.9 m, and 1.1 m. The centerline near-field data for 1.1 m $*$ 1.1 m scan surface is shown in Fig. 4.6.

[2]The detailed analysis about these parameters is carried out in the next chapter dealing with error estimation for arbitrary grids. Here we will only focus on the measurement errors rather than on computational errors.

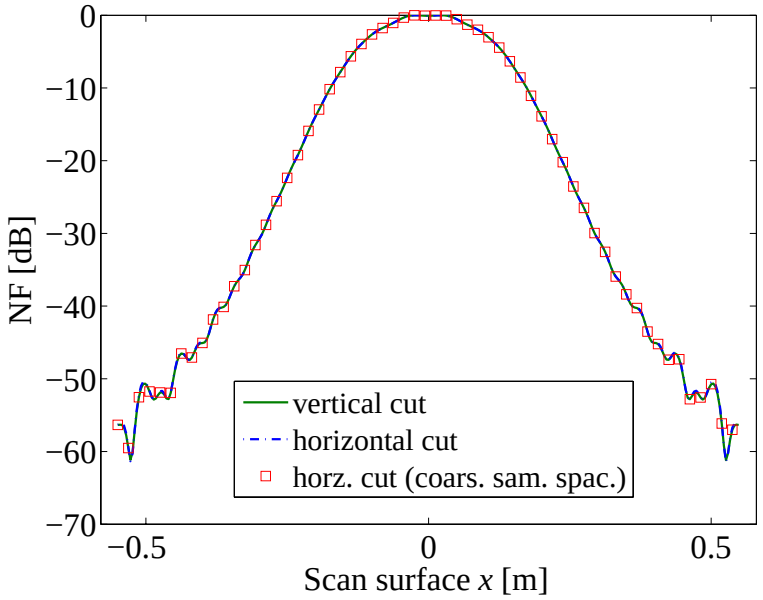

Figure 4.6: Centerline near-field data on 1.1 m ∗ 1.1 m measurement surface.

A smooth decaying curve is observed with some ripples near the edges. The collected near field is transformed to the far field using FIAFTA and the classical technique employing 2D FFT. The error in the side lobe level (SLL) of resulting patterns is shown in Fig. 4.7 (a). It may seem strange that the SLL error increases on increasing the scan plane from 0.6 m to 0.7 m for 2D FFT but Fig. 4.7 (b), showing a part of the enlarged radiation pattern at side lobe region for 0.5 m, 0.6 m, and 0.7 m, explains the behavior. It is merely a coincidence that 0.6 m scan length shows a better performance at the first side lobe whereas the whole pattern is worse than for 0.7 m. Thus, for more insight the complete radiation pattern should be compared.

Fig. 4.8 shows the transformed far-field E-plane cut for 0.7 m ∗ 0.7 m scan plane along with the reference. The reference far field is directly computed at a far field distance approaching 10 km by accumulating electric dipole fields. The maximum observed error, within the valid region, for FIAFTA and 2D FFT approaches is -72.62 dB and -55.862 dB, respectively. The error level increases as we move away from the valid region. If the scan plane size is further reduced from 0.7 m ∗ 0.7 m, the difference in the error levels of both techniques increases i.e. the transformed pattern for the 2D FFT technique becomes worse. The error levels become comparable if the scan plane size is further increased from 0.7 m ∗ 0.7 m.

The dominant performance of FIAFTA against area truncation error comes from the fact that FIAFTA first determines equivalent plane wave sources on the complete Ewald sphere from the given measurement data and, in the second step, it utilizes equivalent sources to ascertain the far field. This is in contrast to the traditional technique in which the truncated measurement data is transformed to the far field by performing 2D Fourier transform in the first step. FIAFTA does not assume/utilize zero fields or periodic repetition outside the scan plane which results in a systematic error in the computations involved in the modal expansion theory. The use of complete Ewald sphere and the fact that FIAFTA does not transform the measured data in the first step helps in reducing the truncation error and avoids ripples in the far-field pattern, as described in [63].

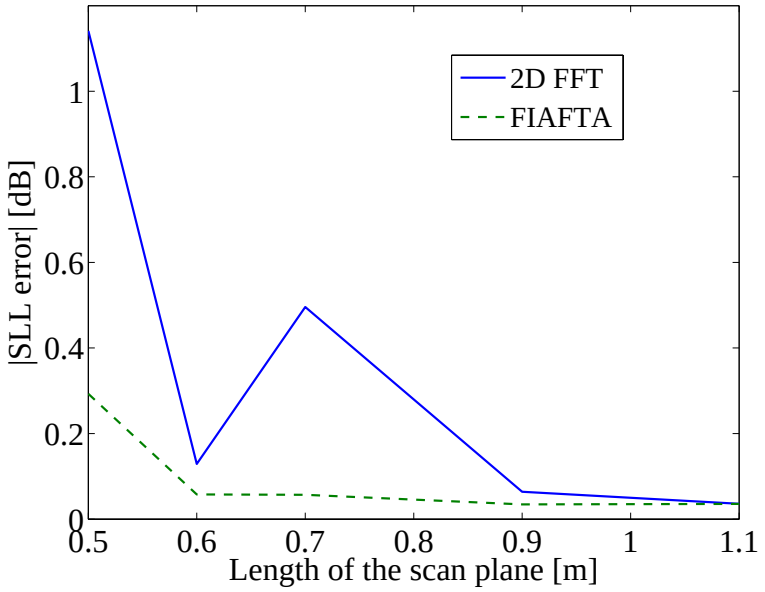

(a)

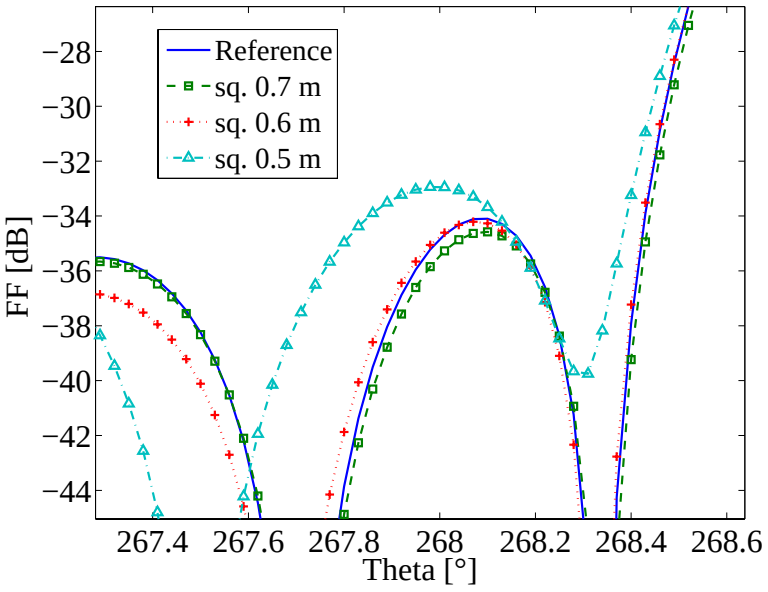

(b)

Figure 4.7: Length of the scan area vs SLL error (a) and enlarged reference and transformed E-plane cut with 0.5 m , 0.6 m, and 0.7 m scan length 2D FFT (b).

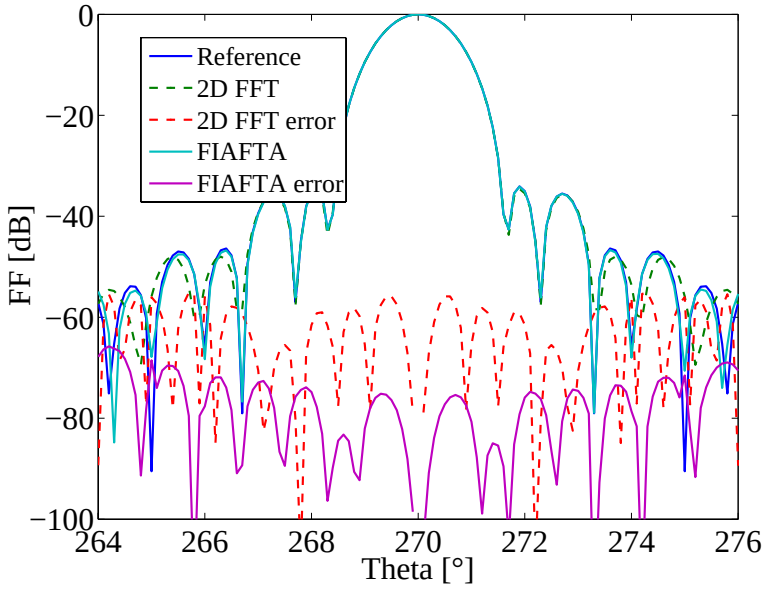

Figure 4.8: E-plane cut for 0.7 m $*$ 0.7 m scan plane.

Data Point Spacing

The distance between near-field sampling points greatly controls the accuracy of the transformed pattern. In the 2D FFT based approach, the incremental data going from the integral of Eq. (1.5) to the discrete Fourier Transform Eq. (1.6) is exact if the Fourier Transform of the measurement data is band-limited between band limits k_x and k_y, and the data point spacing specify the sampling criteria

$$\delta_x \leq \frac{\pi}{k_x}, \quad \delta_y \leq \frac{\pi}{k_y} \tag{4.5}$$

corresponding to those band limits [42][64]. If the measurement plane is located at a region in space where there are no evanescent waves, then the maximum wave numbers are $k_x = k_y = k_0 = 2\pi/\lambda$ and therefore $\delta_x = \delta_y = \lambda/2$ [64]. If the given sampling criteria is violated, it directly results in an aliasing error, thus deteriorating the far-field. It must be noted here that the given sampling criterion is independent of the size of the antenna and requires equidistant spacing between the measurement points. FIAFTA, on the other hand, gives the freedom of using irregular grid and the sampling criterion for FIAFTA is dependent on the size of the antenna and the separation between the AUT and the measurement plane[3]. To demonstrate the effect of irregular spacing between measurement points, a normally distributed sampling error with standard deviation $\sigma = 2.5\lambda$ is superimposed in the position data of a $\lambda/2$ measurement grid. The resulting position distribution is shown in Fig. 4.9 with white pixels marking the position of measurement points. The spacing between the consecutive rows in x or z equals $\lambda/2$. It can be seen in Fig. 4.9 that the scattered black spots between the white pixels represent larger measurement point spacing compared to $\lambda/2$. The near field is computed using the irregular position data and is transformed using FIAFTA. The resulting E-plane cut is shown in Fig. 4.10 (a). The negligible change in the error level confirms the insensitivity of the FIAFTA against the irregularity. In addition, the effect of coarser sampling on transformed patterns is analyzed. The near-field data is again collected on an equally spaced

[3]Extensive analysis regarding the derivation of sampling criterion of FIAFTA is explained in Chap. 6, for current error analysis $\lambda/2$ sample spacing is considered for fair comparison between FIAFTA and the traditional technique employing 2D FFT.

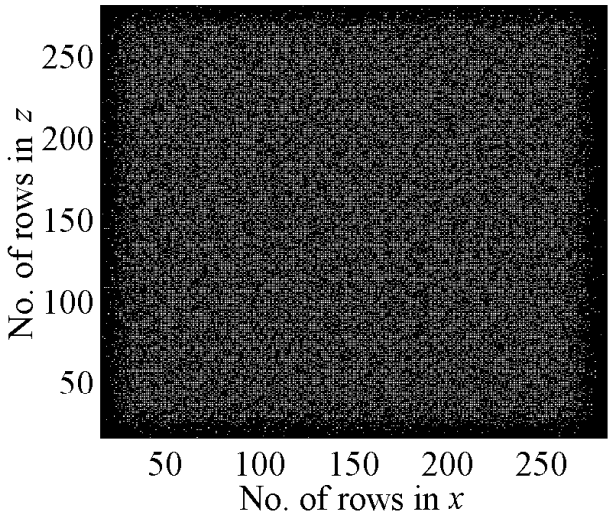

Figure 4.9: Scan plane representing the distribution of measurement points (white pixels denote the position of sampling points and the consecutive distance between two rows is $\lambda/2$).

measurement grid but, with coarser sampling i.e. 2.5λ and the near-field horizontal cut is shown in Fig. 4.6. The transformed patterns are shown in Fig. 4.10 (b) for both FIAFTA and 2D FFT approaches. Apart from the boresight region, where the accuracy of FIAFTA approach can be increased by more number of interpolation points, the error level of 2D FFT increases probably due to the aliasing effect.

Position Inaccuracy

In an ideal near-field measurement, the radiated field of the antenna should be measured on the scan plan with exact information about the position of the data points. However, in reality, the measurement position is not exactly known and no matter how small the position error is, it results in erroneous phase and magnitude information. Although, in state-of-the-art measurement setups, laser interferometers are used to control the position but with accuracy of several tens of μm. To account for the effect of the position inaccuracy, we generate an erroneous measurement grid by superimposing a normally distributed error in the position data similar to the previous sub-section but now with $\sigma = 100\,\mu$m. Afterwards, the near field is collected on the erroneous grid and is then transformed using correct positions of the measurement points thus incorporating the position inaccuracy effect. In the first step, the displacement is introduced in the in-plane coordinates i.e. x and z (refer to Fig. 4.2) and the transformed E-plane cuts are shown in Fig. 4.11 for FIAFTA and 2D FFT based approaches, respectively. The transformed patterns for transverse position inaccuracy show a negligible change in the error level and thus suggest the fact that in-plane position inaccuracy of $100\,\mu$m at 40 GHz frequency does not contribute a major error in the radiation pattern.

The second step involves the inaccuracy introduced in the longitudinal i.e. y-position (refer to Fig. 4.2). In this case, the in-plane coordinates are kept at their original position while using the erroneous longitudinal position in the computation of the radiating near field. The transformed patterns in Fig. 4.12 shows the effect of the longitudinal position inaccuracy. The error level increases to maximum values of -54.62 dB and -53.89 dB for 2D FFT and FIAFTA techniques, respectively.

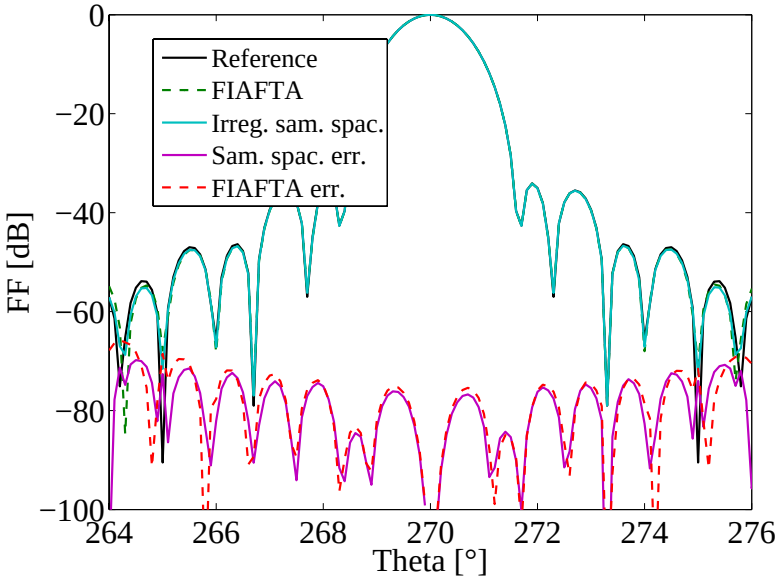

(a)

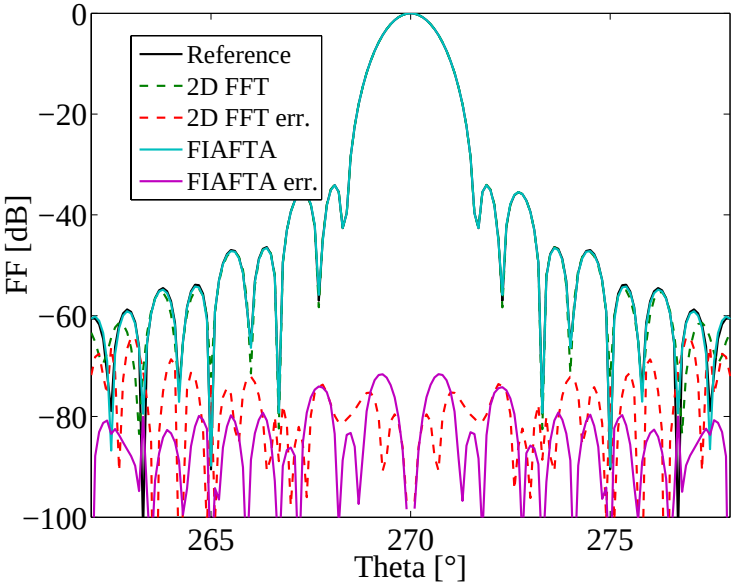

(b)

Figure 4.10: E-plane cut for $0.9\,\mathrm{m} * 0.9\,\mathrm{m}$ scan plane with irregular sample spacing (a) and with $2.5\,\lambda$ sample spacing (b).

It clearly shows that both approaches are equally sensitive to the phase inaccuracy produced by the error in the longitudinal position. Any error in the position of the measurement points in the direction of propagation results in an inaccurate phase measurements and thus results in deteriorated transformed far field for both cases.

4.2.2 Instrumentation Errors

One of the major set of errors during near-field measurements is introduced by the measurement equipment itself. The probe signal is measured using a receiver i.e. a vector network analyser

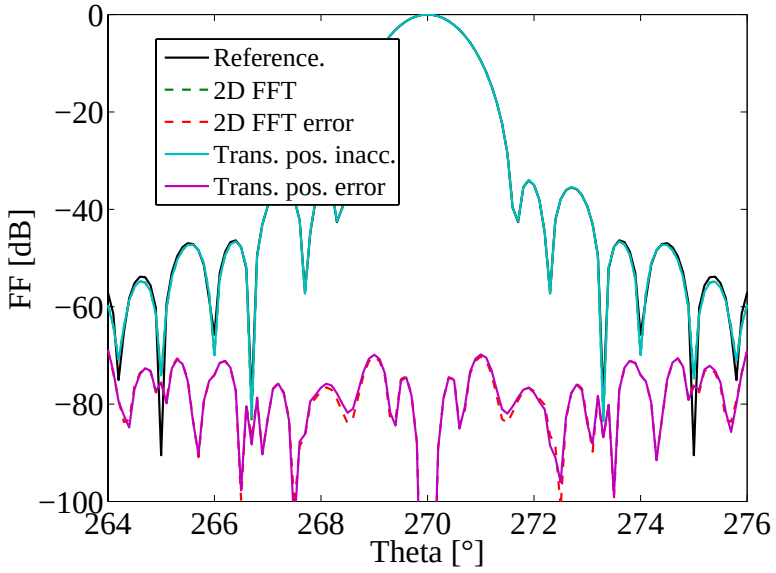

(a)

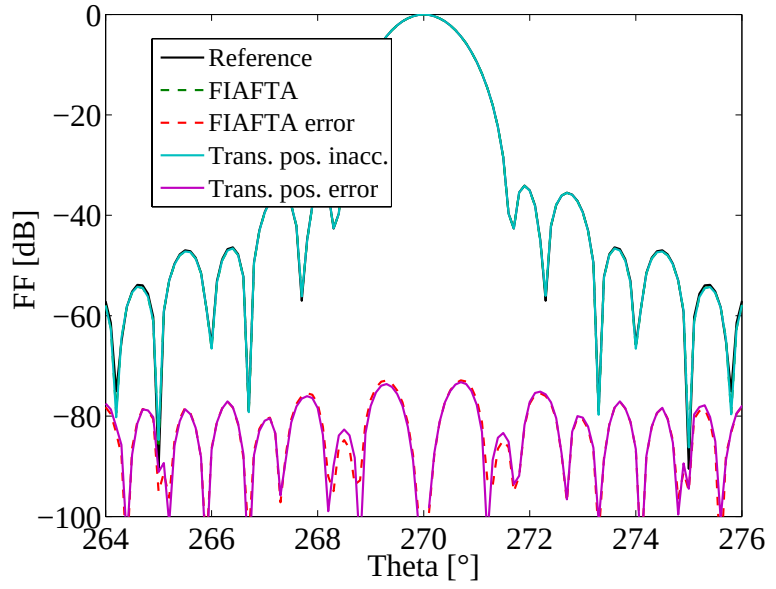

(b)

Figure 4.11: Transformed E-plane using erroneous transverse position in 2D FFT based transformation (a) and FIAFTA (b).

by connecting it with the probe using a RF cable. The inherent noise of the receiver and the movement of the probe along with the cable introduce errors in the magnitude and phase of the RF signal. The effect of instrumentation errors which limit the accuracy of measured amplitude and phase is analyzed using both FIAFTA and the traditional approach. Random as well as systematic phase errors due to the receiver and flexing cables are considered, respectively. The errors are superimposed on synthetically generated error free near-field data. The deterioration in the far field then directly indicates the influence of the imposed errors.

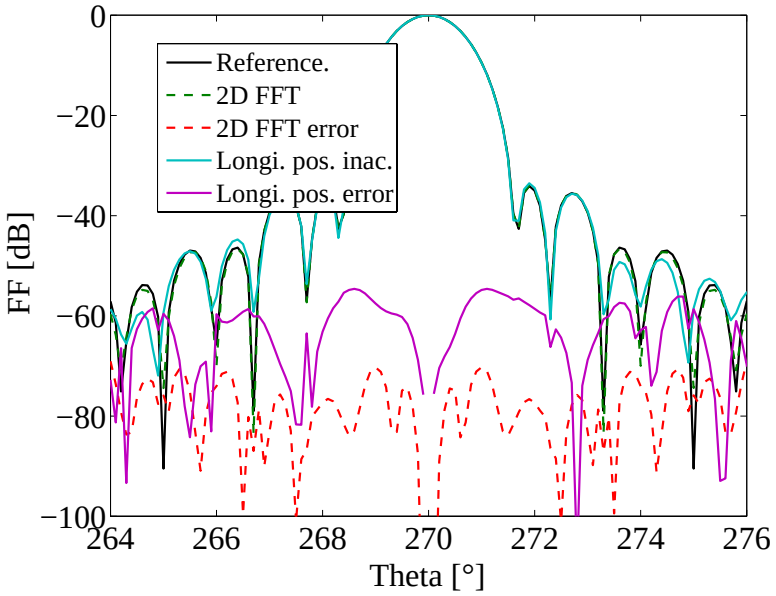

(a)

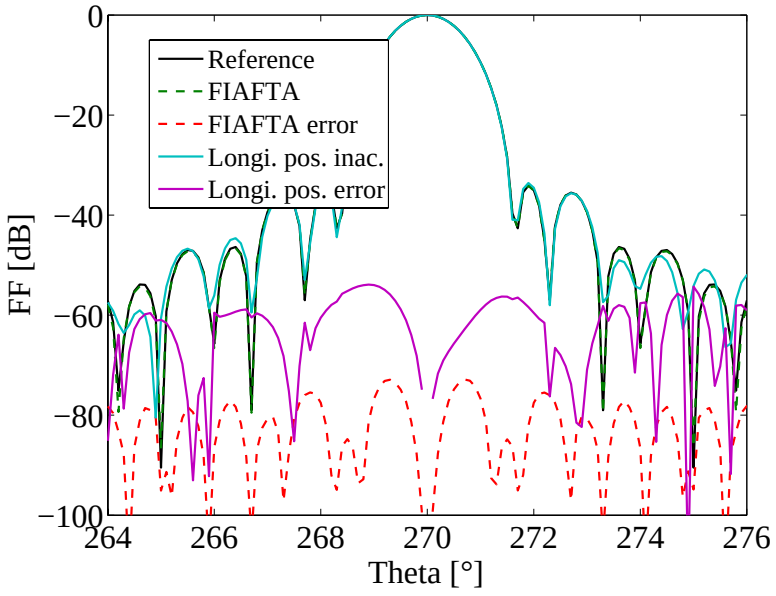

(b)

Figure 4.12: Transformed E-plane using erroneous longitudinal position in 2D FFT based transformation (a) and FIAFTA (b).

RF Amplitude Inaccuracy

Inaccuracy in the measured RF amplitude is greatly dependent on the signal-to-noise ratio (SNR) of the measured signal. Therefore, a unique way of introducing the amplitude error is applied in relation with SNR. Normally distributed magnitude error based on SNR of the received signal is superimposed on the near-field data. An assumed SNR value (x dB) is assumed at the normalized 0 dB pattern level and is decreased down to (x-30) dB at 30 dB below the maximum pattern

level. The intermediate points are linearly interpolated and the standard deviation

$$\sigma = 20\log_{10}\left(\frac{1}{3}\left(1+\sqrt{\frac{0.5}{10^{(\mathrm{SNR}/10)}}}\right)\right) \tag{4.6}$$

is computed empirically with the assumed SNR. The random error obtained using the given standard deviation is added to the near-field data. Fig. 4.13 (a) shows the horizontal near-field cut of a $0.9\,\mathrm{m} * 0.9\,\mathrm{m}$ planar scan plane with and without error clearly showing the error level as well. This unique way of introducing magnitude error in the near field incorporates the effect of absolute noise added by the receiver. The SNR is decreased when the signal strength is decreased while the absolute noise of the receiver is assumed constant. The assumed SNR value at the maximum pattern level can be varied according to the given specifications of the receiver. The SNR is varied from 60 dB to 20 dB at 0 dB normalized pattern level with corresponding decrease at the lower pattern levels. The collected erroneous near-field data are processed using FIAFTA and the classical approach utilizing 2D FFT. E-plane cuts of both transformed patterns are compared with the reference, as shown in Fig. 4.13 (b). Due to symmetry of the near field (see Fig. 4.6), similar results have been seen in the H-plane pattern.

Afterwards, the maximum error in the valid side lobe region and in the main beam of the transformed far field is obtained and the error level comparison with the reference is shown in Fig. 4.14. The difference in the maximum error for both transformation techniques increases with increase in SNR at 0 dB normalized pattern level. As observed, FIAFTA works better as compared to 2D FFT technique at higher SNR while the performance becomes comparable at lower SNR in the valid region. The dominant performance in the side lobe region mainly comes from the reduced scan area truncation error in the FIAFTA approach. The use of the entire Ewald sphere of propagating plane waves facilitates a reduction of the scan area truncation error as compared to 2D FFT technique as explained in the scan area truncation error.

Receiver Phase Error

The error in the measured phase can be both random or systematic due to receiver's limitation of accurate measurement and flexing cables/rotary joints, respectively. Both errors are considered as independent errors and are generated using a normally distributed phase error with 3σ varying from 1° to 10°. The error is superimposed on the phase values of the acquired near-field data. The transformed patterns using classical and the FIAFTA technique show similar sensitivity against random phase errors, as shown in Fig. 4.15. A similar conclusion was made against longitudinal position inaccuracy. The random inaccuracy in longitudinal position used to compute the near field data also results in random phase errors and thus supports the current observation.

Systematic Phase Error

The use of flexing cables in the vertical direction of the scan plane results in a linear increase in the phase error. A simple model is used to replace the effect of phase errors produced by flexing cables. A systematic phase error increasing from 0° to 10° in equal steps along the vertical points of the measurement grid is superimposed in the near-field data, hence accommodating the effect of flexing cables. The proposed model representing the systematic increase in the phase error up to 5° is shown in Fig. 4.16 (a). As expected, the E-plane transformed pattern gets worse while a negligible change in the H-plane transformed pattern is observed for the systematic errors. The maximum error level with systematic phase errors for the valid region of the transformed E-plane pattern is shown for both the FIAFTA approach and the standard 2D FFT technique in Fig. 4.16 (b). It can be observed that FIAFTA shows more stability in the side lobe region.

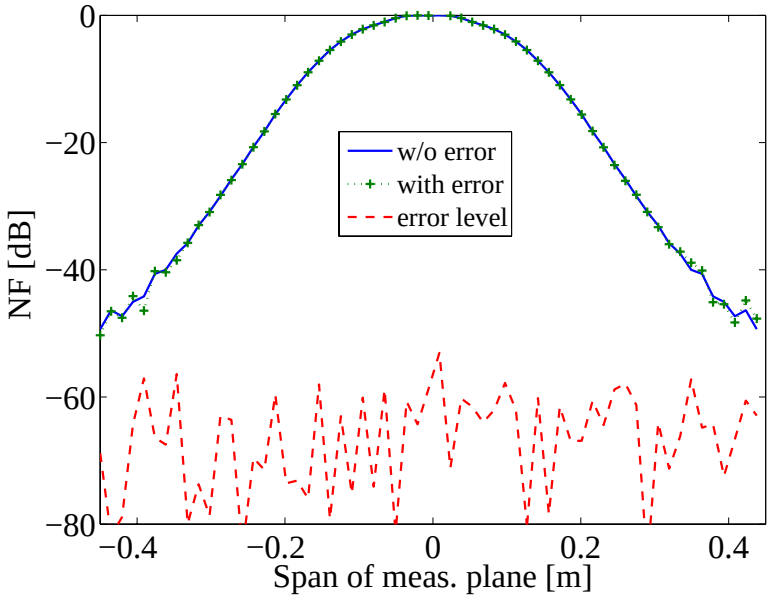

(a)

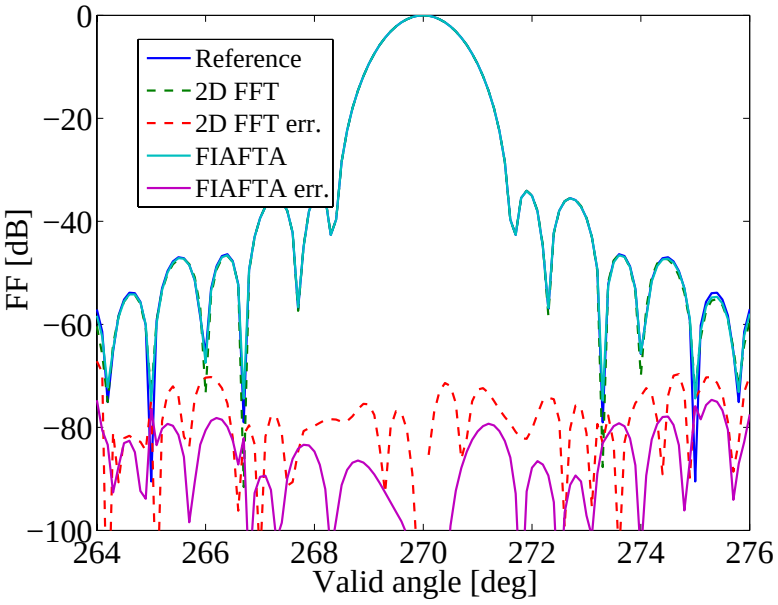

(b)

Figure 4.13: Horizontal cut of near-field data considering 50 dB and 20 dB SNR at 0 dB and -30 dB normalized pattern level, respectively (a) and transformed far-field E-plane cut using erroneous near-field (b).

4.2.3 Probe Parameter Errors

In FIAFTA, the radiating plane waves from the AUT are translated into incident waves at the probe (see Fig. 3.1). Therefore, any error in the position would directly result in a wrong translation of the plane waves. Also, errors in the probe far-field pattern would affect probe correction during the transformation while in case of probe alignment errors, misaligned values of the probe pattern will be utilized. The probe-AUT interaction at small separation distance results in an erroneous near

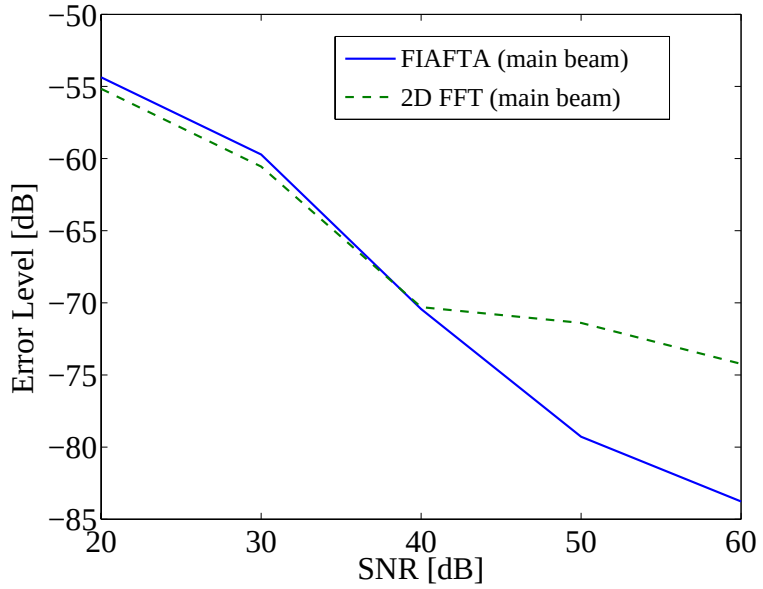

(a)

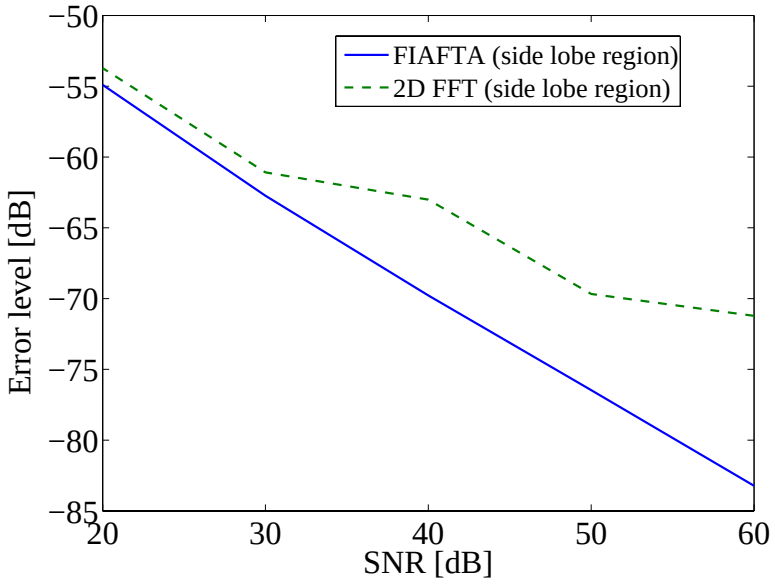

(b)

Figure 4.14: SNR at 0 dB normalized pattern level (used to generate random amplitude error) vs. max. error level in the main beam (a) and max. error level in the valid side lobe region (b).

field due to superposition of reflected fields. In this section, the effect of each individual probe error is analyzed using FIAFTA and the results are compared with those from the traditional 2D FFT technique.

In order to incorporate the effect of probe parameter errors, a medium gain horn like antenna is modeled using electric dipoles in a similar way to the AUT. Electric dipoles are arranged in concentric circles and the diameter of the probe is 0.029 m. The far field of the horn antenna is shown in Fig 4.17. The designed antenna has a relatively lower beam-width as compared to

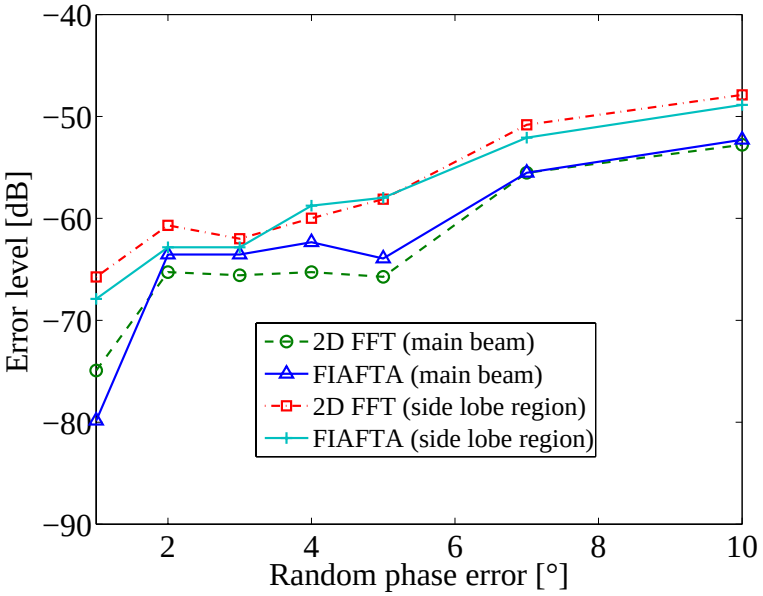

Figure 4.15: Maximum error level in the main beam and the side lobe region of transformed E-plane pattern cut using the 2D FFT and FIAFTA for random phase errors.

standard probes normally used at 40 GHz to visualize even the minute effect of probe errors on the transformed far field of the AUT.

Probe Pattern Inaccuracy

The measured or the transformed far-field pattern normally used for the probe correction contains uncertainty due to instrumentation errors. The corrupted values of the probe far field are realized by introducing a SNR based amplitude error in a similar way as that for the RF amplitude inaccuracy in the measured near-field magnitude for the AUT. The normally distributed magnitude error with empirically derived standard deviation is superimposed on the far-field pattern magnitude. The phase error is also distributed randomly with increasing standard deviation in steps of $0.5°$ according to

$$\sigma_{\mathrm{ph}} = 0.5°, ..., 2.5°. \tag{4.7}$$

Fig. 4.18 shows the erroneous probe far-field pattern cut considering 25 dB SNR at normalized 0 dB pattern level. Similarly, variable SNR values can be used according to the given uncertainty in the probe far field along with phase errors. The SNR value at maximum pattern level is varied from 20 dB to 60 dB along with $0.5°$ to $2.5°$ variation in the standard deviation for the phase error. The maximum error in the transformed E-plane pattern cut is plotted for the classical and the FIAFTA approach in Fig. 4.19.

As expected, results show better performance at higher SNR and small phase errors as compared to lower SNR and large phase errors. The main difference between the performance of both techniques comes from the fact that in the traditional 2D FFT based approach, the relation between the error in the transformed pattern and the error in the probe pattern is one-to-one [42]. It means that an error in any given direction of the transformed pattern directly depends on the probe pattern error in exactly the same direction. Since the FIAFTA approach takes the whole probe pattern

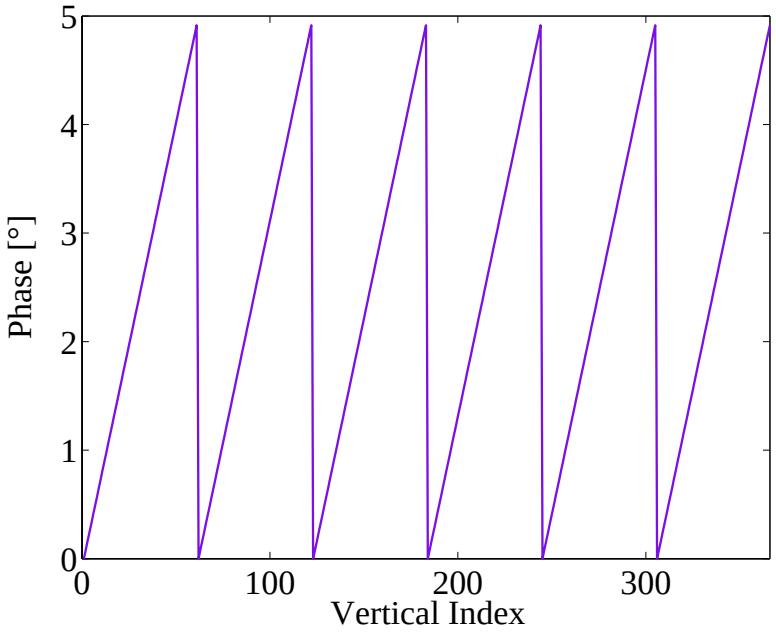

(a)

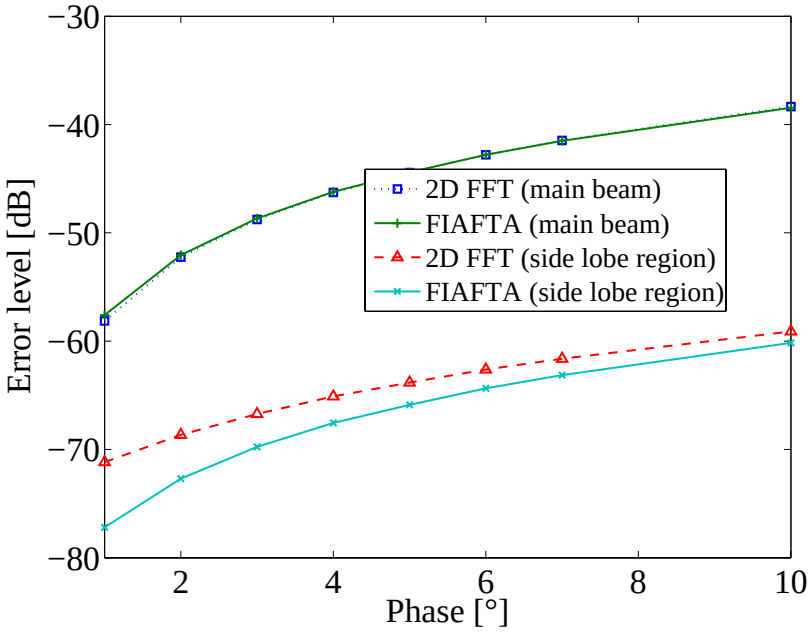

(b)

Figure 4.16: Representation of systematic increase in phase error along vertical direction (index length of 62 represents one column of measurement plane) (a) Maximum error level in the main beam and (b) side lobe region of transformed E-plane pattern cut using 2D FFT and FIAFTA.

into account, normally distributed error is compensated to some extent and results in an increased accuracy.

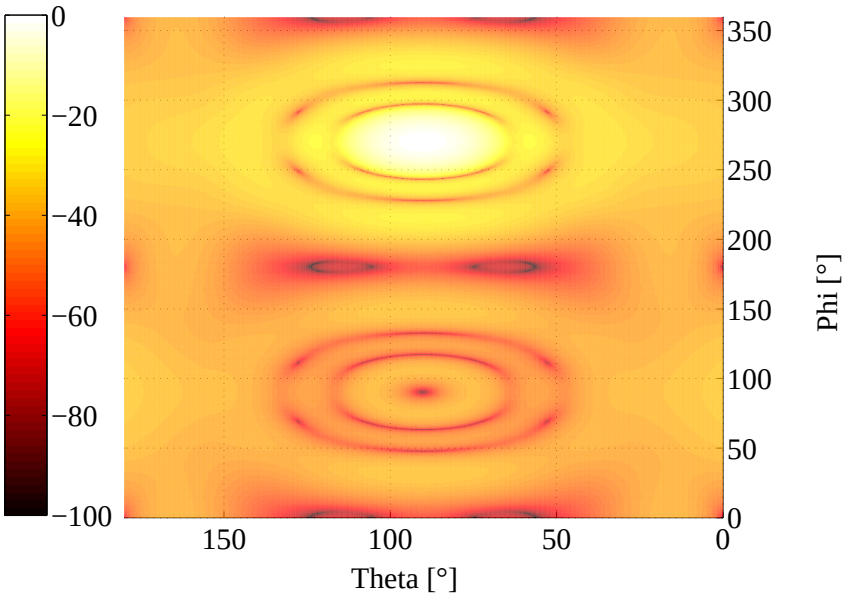

(a)

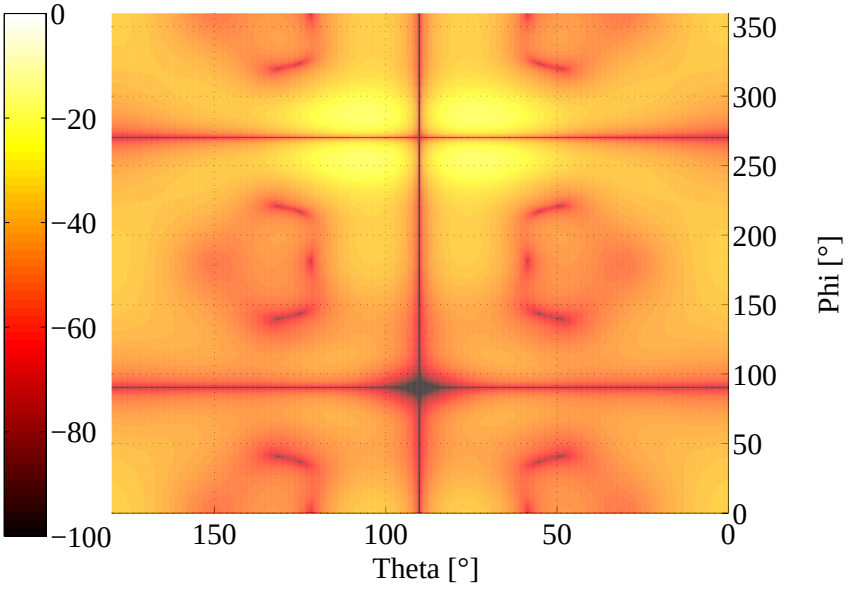

(b)

Figure 4.17: $\boldsymbol{E}_\theta$ and $\boldsymbol{E}_\phi$ component patterns of the probe far field [dB] operating at 40 GHz.

Probe Polarisation Ratio

The polarisation ratios $\rho_s^1(\boldsymbol{K})$ and $\rho_s^2(\boldsymbol{K})$ used in the probe correction formulation (1.7) and (1.8) represent the ratio of the $\boldsymbol{E}_\theta$ and the $\boldsymbol{E}_\phi$ for the two orthogonal probes according to

$$\rho_s^1(\boldsymbol{K}) = \frac{s_{02\mathrm{cr}}^1(\boldsymbol{K})}{s_{02\mathrm{co}}^1(\boldsymbol{K})}, \qquad \rho_s^2(\boldsymbol{K}) = \frac{s_{02\mathrm{cr}}^2(\boldsymbol{K})}{s_{02\mathrm{co}}^2(\boldsymbol{K})}, \tag{4.8}$$

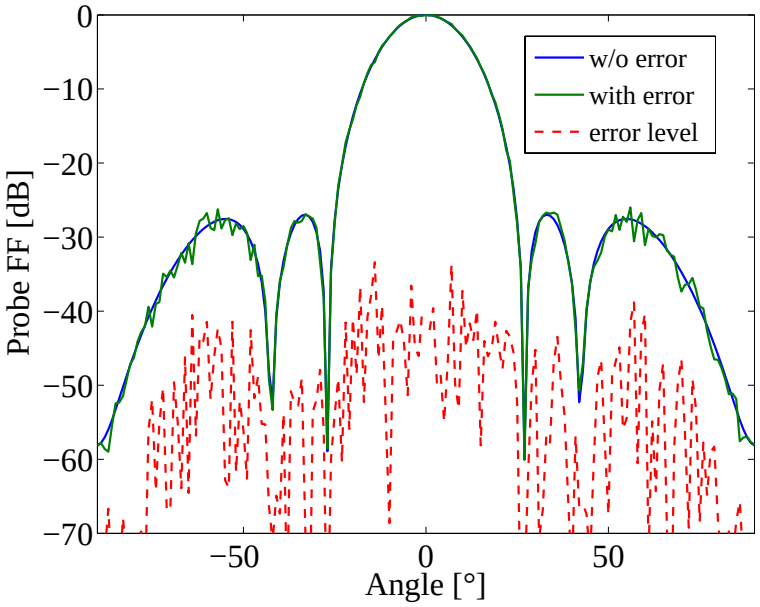

Figure 4.18: Probe far-field pattern cut considering 25 dB SNR at 0 dB normalized pattern level.

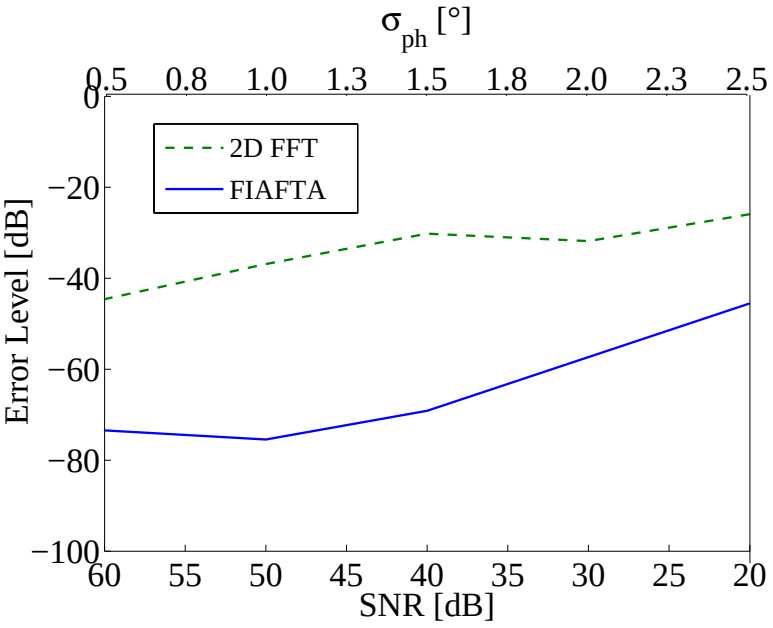

Figure 4.19: Maximum error level in the valid region of transformed E-plane pattern cut in reference to the assumed SNR at maximum pattern level and σ_{ph}.

where s_{02} represent the receiving pattern of the probe. Therefore, any error in the polarization ratio due to non-ideal probes directly effects the probe correction. However, the effect of probe polarization error can be considered as a part of probe pattern inaccuracy, as explained in the previous section. The magnitude and phase error was added in both probe components and is hence inherently contained the effect of probe polarization error as well.

Probe Alignment Error

The probe receiving pattern is related to the probe coordinate system used during the measurement. If the probe is not precisely aligned with the reference coordinate system during the near-field measurement, a shifted pattern is utilized in the transformation and hence degenerates the AUT radiation pattern. To realize the misalignment, the alignment error in the three rotations i.e. azimuth, elevation, and polarization is introduced according to the nomenclature shown in Fig. 4.20.

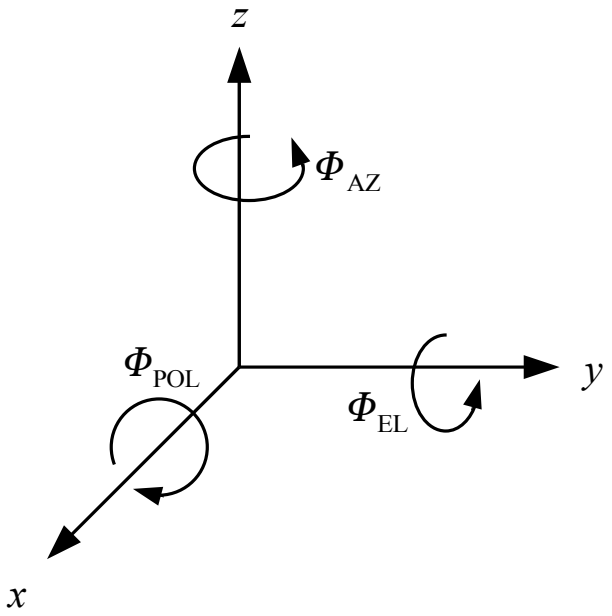

Figure 4.20: Reference alignment configuration.

A normally distributed error is introduced in the probe rotation with standard deviation varying from 0.5° to 2.5°. The erroneous alignment information is applied and the maximum error in the resultant E-plane cut is shown for all the three cases in Fig. 4.21.

Similar error behavior is observed for both transformation techniques and minor deterioration in the transformed pattern is observed for the given error in the alignment. Since the probe pattern is slowly varying and a small scan size is utilized, the rotation misalignment did not affect the AUT pattern significantly. However, for accurate results one can estimate the fluctuations provided that the uncertainty in the probe alignment is known.

Probe-AUT Interaction

It is a common practice to place the measurement plane near to the AUT so that the valid angle can be increased. The decreased separation results in a strong interaction between the AUT and the probe field. A part of the field is reflected back and forth causing multiple reflections error. The

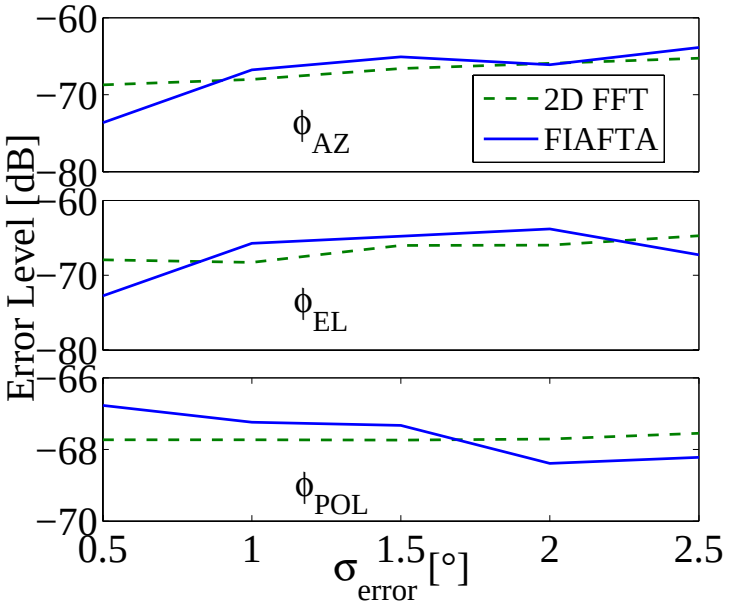

Figure 4.21: Maximum error level in the valid region of transformed E-plane pattern cut with reference to σ_{err} used for generating alignment error.

reflected signal is superimposed on the original field and tends to deteriorate the result. In the current scenario, 15% of the total field is considered as a reflection due to probe-AUT interaction and is superimposed on the ideal data set. The resultant E-plane transformed pattern cut is shown in Fig. 4.22. As can be seen, the error level of both techniques shows similar sensitivity to the reflection error.

4.2.4 Two Planes Method for Reduced Probe-AUT Interaction

As already stated, reduced separation between the probe and the AUT increases the valid angle at the cost of multiple reflections error. The reduction in the error is commonly accomplished by collecting near-field data at a series of closely spaced planes separated by $\lambda/2$. The mean of the transformed field then averages out the error and gives more accurate results. However, increase in the measurement time gets immense. A unique way to reduce multiple reflections while keeping less measurement time consumption is proposed. It is recognized that the effect of the multiple reflection error is maximum in the region where the probe and the AUT directly face each other and decreases as the probe sweeps away from the center, as shown in Fig. 4.23. Also, it is well known that the error decreases as the separation between the AUT and probe is increased. Therefore, for reduced multiple reflections, the near field is collected on two separate planes. The central near-field data is collected on a surface $S1$ at a suitable distance d_1 away from the AUT while the surface S at shorter distance d gathers the near field from the boundary region (see Fig. 4.24). The combined valid angle using the entire surface S is given as

$$\theta_{\mathrm{v}} = \tan^{-1}\left(\frac{L-a}{2d}\right) \tag{4.9}$$

where L is the length of the square shaped measurement plane and "a" is the antenna aperture. The omitted central portion of surface S can be projected backward at a larger separation and the near field is collected on surface S_1. The length L_1 and the separation d_1 of the surface S_1 can be

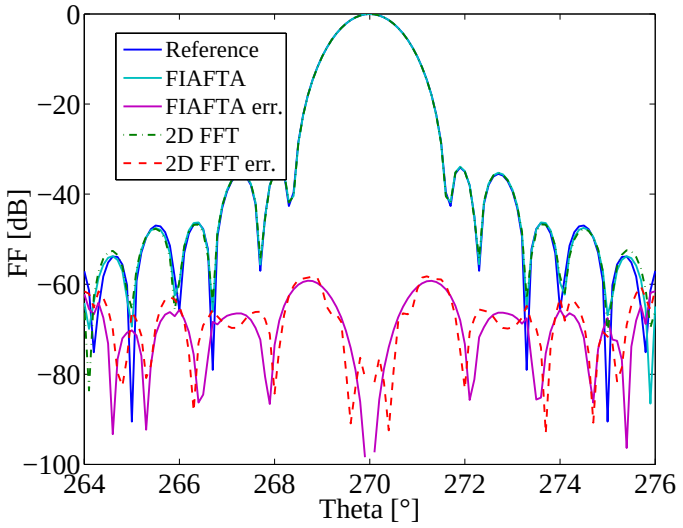

(a)

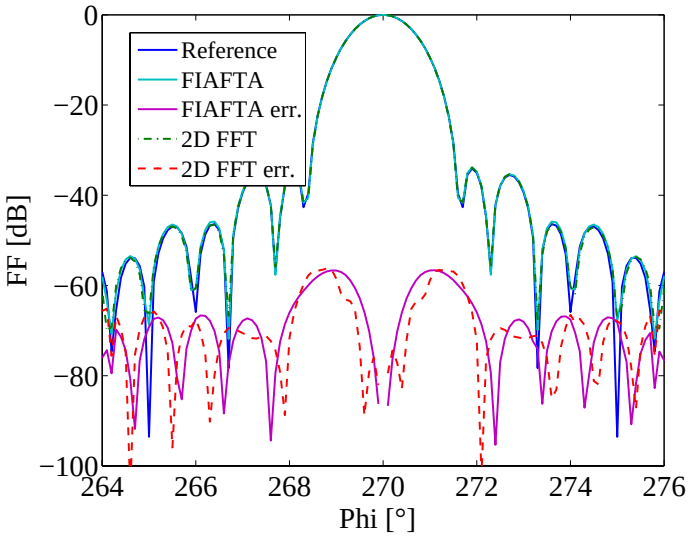

(b)

Figure 4.22: Transformed E- and H-plane cut considering 15% reflection due to probe-AUT interaction.

computed using the valid angle of the omitted central portion of surface S according to

$$\theta_{\text{v1}} = \tan^{-1}\left(\frac{xa-a}{2d}\right) = \tan^{-1}\left(\frac{L_1-a}{2d_1}\right) \tag{4.10}$$

$$\Rightarrow L_1 = \frac{1}{d}(ad_1(x-1)+ad), \tag{4.11}$$

where "xa" is the length of the omitted central portion of surface S in relation with the antenna aperture. Using appropriate parameters according to the given setup one can effectively reduce the multiple reflection error. Fig. 4.25 shows the transformed pattern using three techniques i.e. single plane with multiple reflections (15%), mean of the far field using measurements on four planes and using measurements on two partial planes. For comparison purposes, 5% reflection is assumed

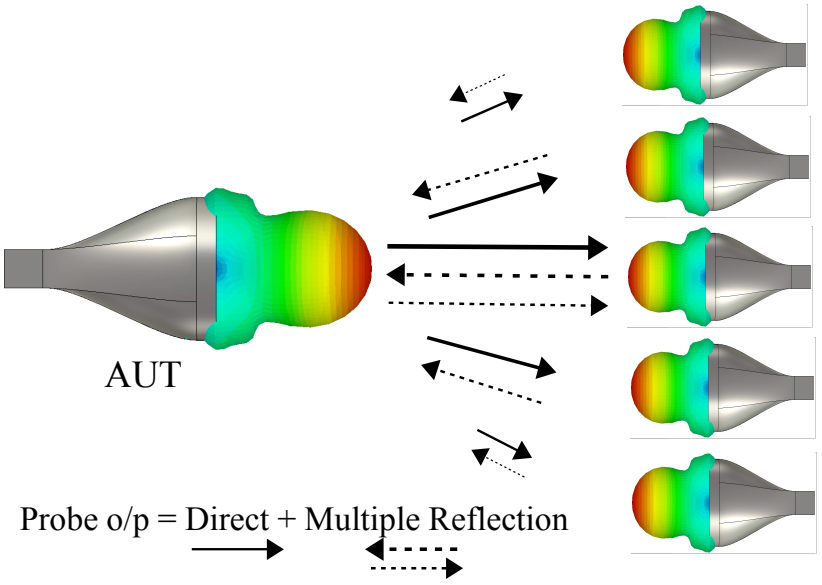

Figure 4.23: Multiple Reflections due to interaction between probe and AUT.

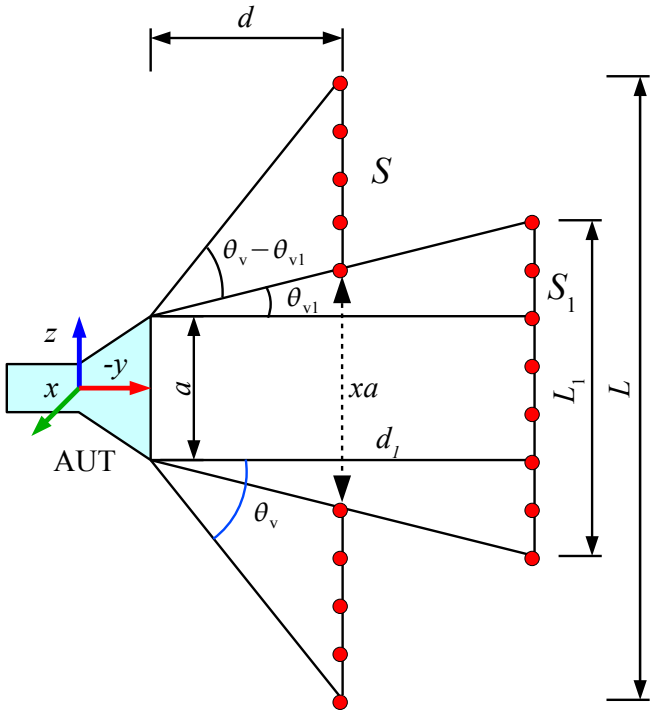

Figure 4.24: Proposed setup for reduced probe-AUT interaction consisting of two partial planes.

for the near field measurements on two partial planes. However, this value varies according to the choice of the probe, the area of the central omitted portion from the near scan plane, and the separation between the AUT and the probe. One can choose the parameters according to the required accuracy in the far field and the given limitations in the measurement setup. As observed, the error due to the two partial planes method is comparable with the method utilizing measurements on four planes and is even better at the nulls.

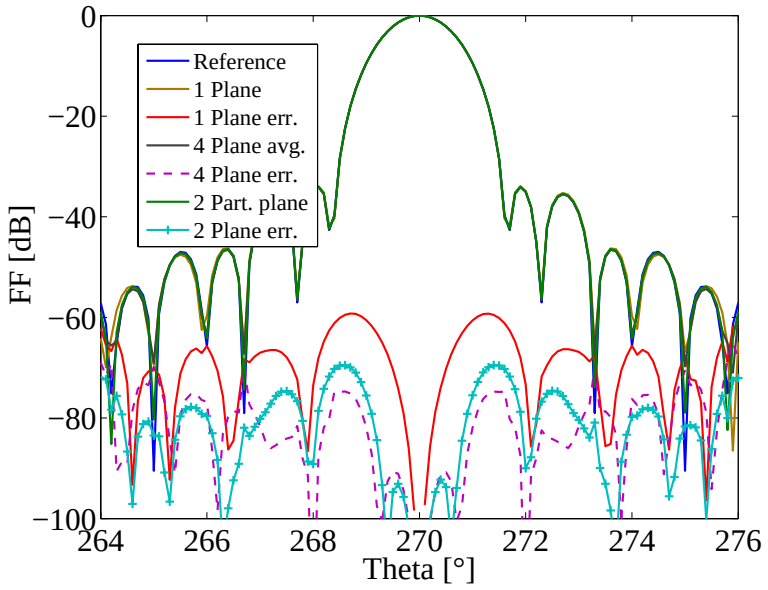

Figure 4.25: Transformed E-plane pattern cut using single plane, averaged field of four planes, and the near field collected on two partial planes.

4.3 Combination of Errors

The degradation in the accuracy of the transformed far field due to corrupted near field because of the combined measurement errors is of most interest. Therefore, most of the above mentioned errors were combined and incorporated in the obtained near field. The values of the near-field measurement error chosen are realistic and are as follows:

- Sample Spacing Error: $\sigma_{\mathrm{ss}} = 5\lambda/3$
- Measurement Position Inaccuracy (xyz): $\sigma_{\mathrm{xyz}} = 200\mu$m/2
- Random RF Phase Inaccuracy: $\sigma_{\mathrm{ph}} = 5°/3$
- RF Amplitude Error:

$$\sigma_{\mathrm{amp}} = 20\log_{10}\left(\frac{1}{3}\left(1+\sqrt{\frac{0.5}{10^{(\mathrm{SNR}/10)}}}\right)\right) \tag{4.12}$$

  considering 60 dB and 30 dB SNR at 0 dB and -30 dB at normalized pattern level.

- Measurement Surface Irregularity (z): $\sigma_{\mathrm{z}} = 0.05$ m/3

- Probe Pointing Inaccuracy ϕ_{EL}: $\sigma_{\mathrm{EL}} = 1.5°/3$
- Probe Pointing Inaccuracy ϕ_{AZ}: $\sigma_{\mathrm{AZ}} = 1.5°/3$
- Probe Pointing Inaccuracy ϕ_{PO}: $\sigma_{\mathrm{POL}} = 1.5°/3$
- Probe Pattern Inaccuracy: in the same manner as RF amplitude error but considering 30 dB and 0 dB SNR at 0 dB and -30 dB normalized pattern level.

Transformed E- and H-plane pattern cuts using the disturbed near field processed using FIAFTA are shown in Figs. 4.26 and 4.27. The reference far field is computed directly at a far field distance of 10 km while the reference transformation includes NFFF transformation using FIAFTA without introducing any error. It has been observed that the maximum error level increased from -75 dB to -60 dB because of the introduction of above mentioned errors. However, still a good accuracy is observed even with the introduction of subjected errors thus employing the fact that FIAFTA offers a robust performance provided the magnitude of the measurement errors is under a certain limit.

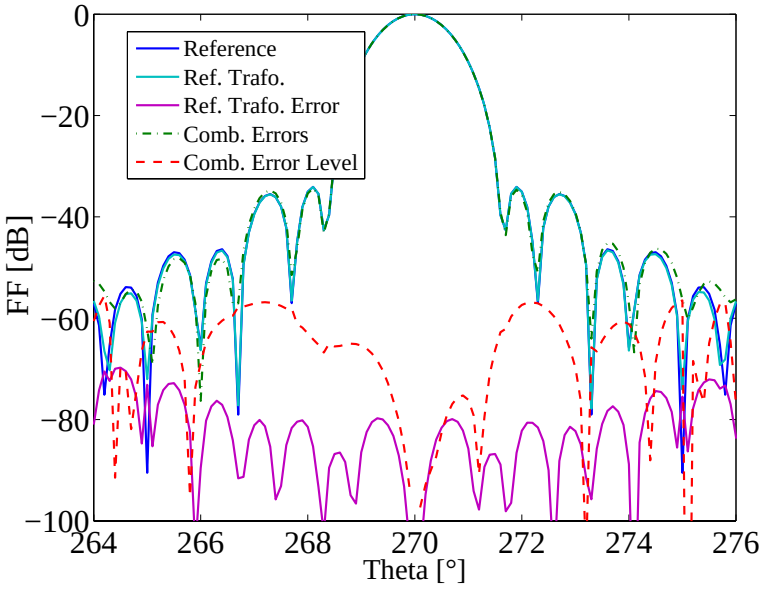

Figure 4.26: Transformed E-plane pattern cut using a corrupted near-field data with combined measurement errors.

4.4 Short Summary

The complete comparative analysis of planar near-field measurement errors between FIAFTA and the traditional transformation technique employing 2D FFT revealed the following important facts:

1. The use of the complete Ewald sphere of propagating plane waves helps FIAFTA to perform better against scan area truncation errors as compared to the 2D FFT based approach. The same reason facilitates FIAFTA to perform better against RF amplitude inaccuracy as well in the side lobe region.

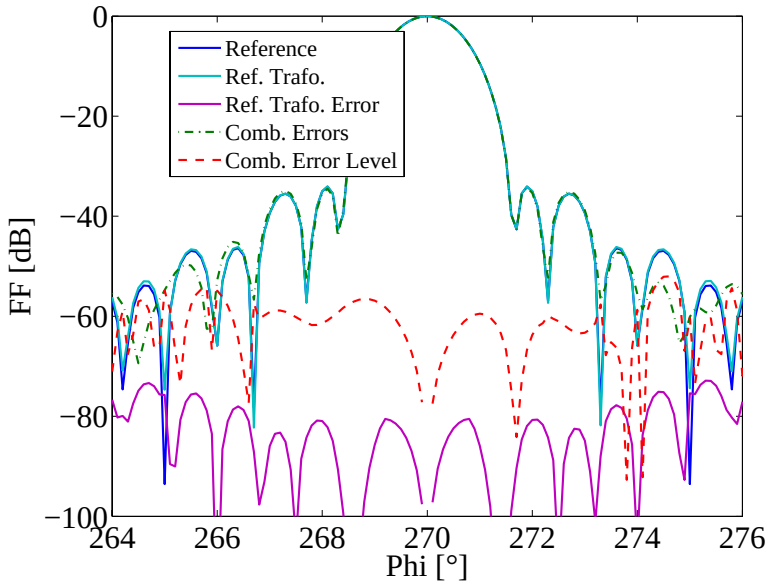

Figure 4.27: Transformed H-plane pattern cut using a corrupted near-field data with combined measurement errors.

2. FIAFTA can work with irregular grids and provides good results even if the near-field sample spacing is increased from the standard $\lambda/2$ sample spacing. This conclusion assisted us to determine the sampling criterion for FIAFTA on the arbitrary surfaces and is explained in Chap. 5.

3. The effect of probe pattern inaccuracy has a negligible effect on the performance of FIAFTA as far as random error is considered in the probe pattern. The dominant performance comes from the fact that FIAFTA considers the whole probe pattern for the probe correction which is in contrast with the traditional technique.

4. The multiple reflection error can be significantly reduced by using FIAFTA if the measurement is performed on two partial planes separated by a suitable distance from the AUT. The classical technique has the inability to simultaneously handle the data collected on two different planes.

For all other errors FIAFTA shows similar sensitivity when compared with the 2D FFT based technique. It must be emphasized that the given results are valid only for the planar scanning geometry and for the given antenna. The error behavior varies according to the type of the antenna and the scanning surface. Therefore, a general technique which can estimate the error for any scanning geometry and is valid for all kind of antennas is highly desirable. Also, in the above analysis, the synthetic approach is used which gave the opportunity to use the ideal far field which is not available in real life. Estimating uncertainty in the far field without the knowledge of the ideal far field is rather demanding. These issues are tackled in the next chapter where a general technique is formulated using FIAFTA to determine the far-field uncertainty with the knowledge of the extent of error in the near field.

Chapter 5

Estimation of Far-Field Uncertainties for Arbitrary Near-Field Errors

In the last chapter, the error behavior of FIAFTA was compared with that of the standard technique employing 2D FFT for planar near-field measurements. Assuming a similar comparative response for the cylindrical and spherical measurement errors, a rather demanding analysis for the estimation of far-field uncertainties due to arbitrary near-field measurement errors is now performed [10]. Fortunately, the formulation of FIAFTA allows to alienate the effect of any arbitrary near-field error using the erroneous near-field data along with the knowledge of the extent of the error. Before going into the detail of the error estimation techniques using FIAFTA, we first review the available methods of error estimation using standard techniques.

5.1 Review of Error Estimation Techniques

A major computer simulation based study for planar near-field measurement errors has been performed by Rodrigue et al. in [66]. The hypothetical near-field is perturbed with position and instrumentation errors to determine the far-field behavior. Newell and Crawford estimated the scan area truncation error by utilizing the measured near-field data in [62]. The first concrete error analysis for planar near-field antenna measurements has been performed by Yaghjian [61] to determine the upper bound errors in the far-field parameters. With a rigorous theoretical analysis, he derived expressions for estimating uncertainties in the far field due to scan area truncation, probe positioning inaccuracies, instrumentation errors effecting amplitude and phase of the probe output, as well as the multiple reflection error. However, the analysis is only valid for electrically large antennas ($>10\lambda$) and it is assumed that the size of the scan plane is appreciably larger than the antenna size. Also, for the probe position inaccuracy, the worst case error is assumed in the direction of observation involving the side lobe region. A similar concept is valid for other errors as well. Therefore, the resulting error estimates predict a worst case error which becomes unrealistically high. Newell performed a more realistic error analysis in [42] making use of a known spatial dependency of errors. The comprehensive analysis identifies the significant errors and also estimates the magnitude of all near-field error sources. Error equations are derived afterwards to determine the relationship between the measurement errors and the far-field results. However, the analysis is again valid only for planar scanning surfaces and assumes antennas with electrical size $>4\lambda$ for the derivation of the error equations. A more rigorous methodology is presented in [67] for the accuracy qualification of near-field measurement ranges. The methodology involves computer simulation, component certification, self tests, and comparison tests to determine upper bound far-field errors due to near-field measurement errors. Afterwards, a near-field error budget is proposed

for each near-field system component.

A detailed error analysis for spherical near-field measurements is presented in [25]. Mechanical inaccuracies, spherical area truncation, receiver errors, probe parameter error etc. are considered and the results of computer simulations with known inaccuracies are compared with inaccuracies in real measurements. The emphasis of the analysis is mainly on errors occurring in the main beam and in the first side lobe region. Nevertheless, it is stated that the results are applicable only for directive spot-beam antennas and may only be considered as guidelines. There are many other contributions in which authors address the individual error sources and propose their compensation techniques e.g. regarding probe positioning errors [68], [69], [70] effect of random errors [71], measurement area reduction compensation [72][73], analysis of system phase errors [74], methods to reduce leakage errors [75], etc.

A common observation implicit in the available literature is that the analysis is valid only for a given set of antennas and it assumes a specific scanning geometry. Error equations are not generalized and may not be applicable to all antennas. Also, the analysis is usually performed with emphasis on estimating the error in the main beam and in the first side lobe of the transformed far field. The mean and the maximum error estimation within the valid angle of the transformed far field needs more rigorous analysis. It is highly desirable to derive an error model which is suitable for arbitrary measurement grids and is suitable for all kinds of antennas. The error model should also provide realistic error estimates and should not always consider the worst case scenario.

In this chapter, an extensive error analysis is performed for arbitrary near-field measurements which is valid for all kinds of antennas. Though we consider FIAFTA in the error analysis, the error model is equally valid for transformation techniques making use of other equivalent sources like electric currents. These techniques use a forward operator in the formulation of the transmission equation. The linearity of the forward operator makes it possible to oversee the effect of near-field errors and to estimate the mean and the maximum error in the transformed far field. The accuracy of the estimated uncertainty in the far field is dependent on the knowledge of the near-field measurement inaccuracies. The magnitude of the near-field measurement errors is usually available for near-field measurement ranges, e.g. the corrected planarity (RMS) of a planar NSI scanner 300V-6×6 is 0.025 mm [37]. Also, the uncertainty in the received near-field magnitude via Rohde & Schwarz vector network analyzers R&S®ZVL for 6-13.6 GHz frequency range is $<$0.2 dB for pattern levels from 0 dB to -50 dB [76]. Similarly, the magnitude of other near-field measurement inaccuracies can be extracted from the data sheets of the equipment. Once the uncertainties in near-field parameters are known, they can be used to find the uncertainty in the plane wave spectrum representing the AUT fields and hence the error in the far field.

5.2 Arbitrary Near-Field Error Analysis

The error behavior of FIAFTA is analyzed by setting up a linear system of equations

$$\boldsymbol{U}' = -\mathrm{j}\frac{\omega\mu}{4\pi}\,\|C\| \cdot \tilde{\boldsymbol{J}}' \tag{5.1}$$

using (3.4), where $\boldsymbol{U}'$ is the vector containing the probe output for all measurement points and $\tilde{\boldsymbol{J}}'$ contains the plane wave coefficients of the AUT. The diagonal translation operator $T_L(\hat{k}, \hat{r}_{\mathrm{M}})$, the weighting factor $W(k_\theta)$ and the probe correction coefficient $\bar{\boldsymbol{P}}(\hat{k}, \hat{r}_{\mathrm{M}})$ are combined to form the coupling matrix $\|C\|$. The given set of linear equations is solved using the Generalized Minimum

Residual Solver (GMRES)[51] in a least mean square sense (LMS) [77] as

$$\|C\|^H \cdot \boldsymbol{U}' = -\mathrm{j}\frac{\omega\mu}{4\pi}\|C\|^H \cdot \|C\| \cdot \tilde{\boldsymbol{J}}', \tag{5.2}$$

where $\|C\|^H$ is the complex conjugate transpose of the coupling matrix. The near-field errors are divided into three major categories based on their influence on the probe output, probe correction coefficient, and the translation operator. The other two categories include computational errors due to inappropriate selection of parameters during the transformation and the miscellaneous errors like aliasing error, scan area truncation, etc.

5.3 Synthetic AUT and Probe Antenna Design

The AUT used in the current analysis is an electrically small antenna (3.8λ) and is designed in a similar manner as described in section 4.1. The dipoles are arranged in concentric circles and the magnitude of the source dipoles follows a cosine profile from the inner to the outer circle. The AUT represents a medium gain horn like antenna operating at 10 GHz with a directivity of 19.34 dB. The antenna aperture is 11.6 cm and the total number of source dipoles used is 162. The probe used for the given AUT is an open ended wave guide (OEWG) also operating at 10 GHz.

It must be emphasized here that the arbitrary near-field error analysis presented here is equally valid for practical measurements. The only reason for using the synthetic approach is to compare the estimated errors with that of the observed errors in reference to the ideal far field and thus determine the performance of the provided error model. In addition the effect of each near field error on the transformed far field can be isolated using the synthetic approach.

5.4 Computational Errors

It is conventionally assumed that the errors due to theoretical approximations are negligible, however, there are various parameters involved in the formulation of FIAFTA which determine the accuracy of the transformed far-field. The choice of optimum parameters is necessary to assume negligible errors in the transformed far field. The major factors are discussed here along with their effect on the transformed results.

5.4.1 Number of Levels and Buffer Boxes

There are few factors like the number of levels in the multilevel approach[1] and the number of buffer boxes [78] which effect the transformed pattern. The number of levels is chosen keeping in view the size of the AUT and the probe. The optimum choice of the number of levels varies from case to case e.g. for planar scanning surfaces a cubical box structure with minimum box size chosen according to the size of the probe and maximum box size chosen according to the minimum separation between the AUT and the probe gives the optimum result. If the hierarchical structure is not chosen properly, the multilevel approach might even consume more time instead of improving the computational time. The effect on the accuracy, however, remains negligible. The buffer boxes are used to maintain a certain distance between the minimum spheres enclosing the AUT and the probe. The minimum spheres must not overlap in order for the representation to converge. For a good accuracy a larger separation between the AUT and the probe is recommended and is achieved by increasing the number of buffer boxes.

[1] In the multilevel approach the computational complexity is reduced and the translations are performed on the coarsest level and are processed through various levels to arrive at the observation point (see [4] for more details.)

5.4.2 Multipole Order of AUT and T_L

The multipole order used to compute the translation operator also effects the accuracy of FIAFTA. A semi-empirical formula to compute the multipole order L_{T_L} is [50]

$$L_{T_L} = kd/2 + 1.8 d_o^{2/3} (kd)^{1/3}, \tag{5.3}$$

where $d = d_\mathrm{a} + d_\mathrm{p}$ is the sum of diameters of the smallest spheres enclosing the AUT and the probe antenna, respectively, while $d_o = \log(1/\gamma)$ is the factor controlling the desired accuracy of the expansion. In a similar fashion, the AUT multipole order is approximated as [25]

$$L_\mathrm{AUT} \simeq kd_\mathrm{a}/2 + 10. \tag{5.4}$$

The translation operator incorporates the effect of both the probe and the AUT and requires larger spectral content. Therefore, the multipole order of the translation operator is larger than the multipole order of the AUT. The accuracy of the multipole expansion is controlled by γ. Choosing a very low value of γ results in insufficient spectral content for accurate representation of the radiation pattern. On the other hand, a very high value makes the second order Hankel function $\mathrm{h}_l^{(2)}(kr_\mathrm{M})$ to approach infinity quickly and thus deteriorates the resultant pattern. The maximum error level observed in the transformed field of the horn antenna operating at 10 GHz against variable multiple order is shown in Fig. 5.1. A similar analysis has been carried out for a variety of

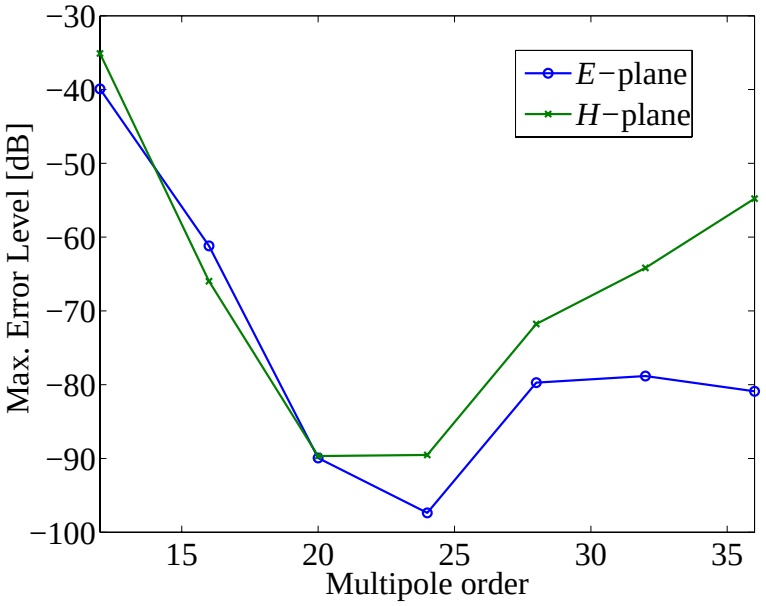

Figure 5.1: Multipole order vs. max. error level in E- and H-plane of horn antenna.

antennas (electrical size varying from 4λ to 64λ) and an empirically deduced value of ϵ is found to be $\simeq 10^{-4}$. The observed maximum error level for the same value of ϵ for the horn antenna is $\leq$-90 dB in both E and H plane pattern cuts (see Fig. 5.1 for multipole order = 24).

5.4.3 Residuum of GMRES Solver

As already stated FIAFTA is implemented in an iterative fashion using the GMRES solver. The optimum selection of the relative residuum

$$\tau = \frac{\mathrm{norm}(\|C\|^H \|C\| \tilde{\boldsymbol{J}}'_\mathrm{final} - \|C\|^H \boldsymbol{U}')}{\mathrm{norm}(\|C\|^H \boldsymbol{U}')} \tag{5.5}$$

of the GMRES solver is extremely important both in terms of time and accuracy. Therefore, once the unknown plane wave coefficients are determined, the near-field error

$$\epsilon = \text{norm}(\tilde{\boldsymbol{J}}'_{\text{final}} - \|C\|^H \boldsymbol{U}') \tag{5.6}$$

is determined to compare the near field reproduced by plane wave sources with the given near field. It has been found empirically that when the residual error is $<10^{-3}$ and when the difference between the residuum of GMRES solver in two consecutive iterations tends to remain the same, the error level

$$\text{Error level} = 20\log_{10}(\text{abs}\,(|\boldsymbol{E}_{\text{ref}}\,(\theta,\phi)\,| - |\boldsymbol{E}_{\text{trans}}\,(\theta,\phi)\,|)) \tag{5.7}$$

is usually <-70 dB. A similar criterion is applied for the synthetic horn antenna using a spherical measurement and at 38^{th} iteration it satisfies the above described condition. Fig. 5.2 shows the logarithmic decrease in the residuum of the GMRES solver versus number of iterations. As observed, the residuum decreases rapidly in the beginning but after a certain number of iterations the convergence rate is very slow and stays almost constant.

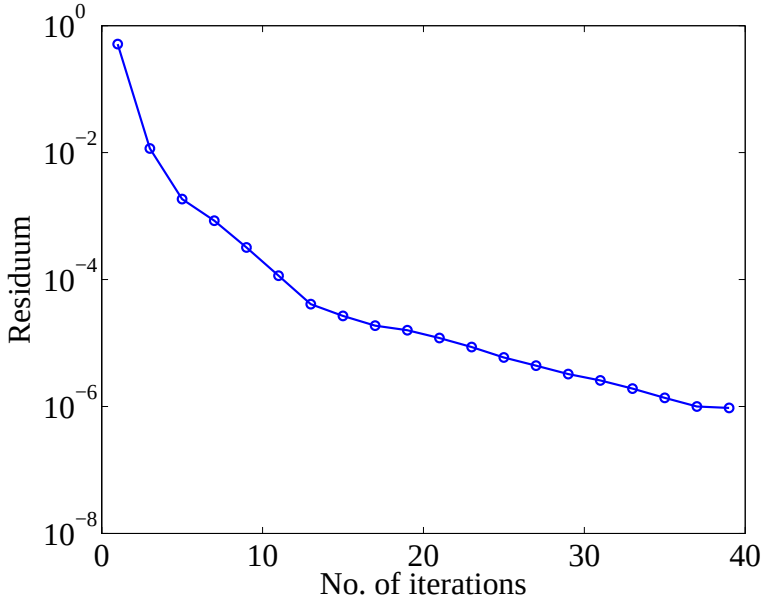

Figure 5.2: Residuum vs. no. of iterations of GMRES solver for horn antenna.

The transformed pattern cuts of the horn antenna using 6 hierarchical levels, 3 buffer boxes, and 10^{-4} accuracy of the multipole expansion of the translation operator are shown in Fig. 5.3. In the spherical setup, the AUT is looking in -y direction and the whole spherical surface is considered. A near-field error ϵ of less than 10^{-4} is observed and as can be seen, the difference between the ideal and the transformed far field using FIAFTA is approaching -90 dB which can be considered negligible. The average iteration time observed is 2.1 s per iteration.

5.5 Errors Affecting the Probe Output

The errors described in this section mainly involve inaccuracies due to the RF measurement system and directly affect the magnitude and phase of the probe output. The errors include receiver

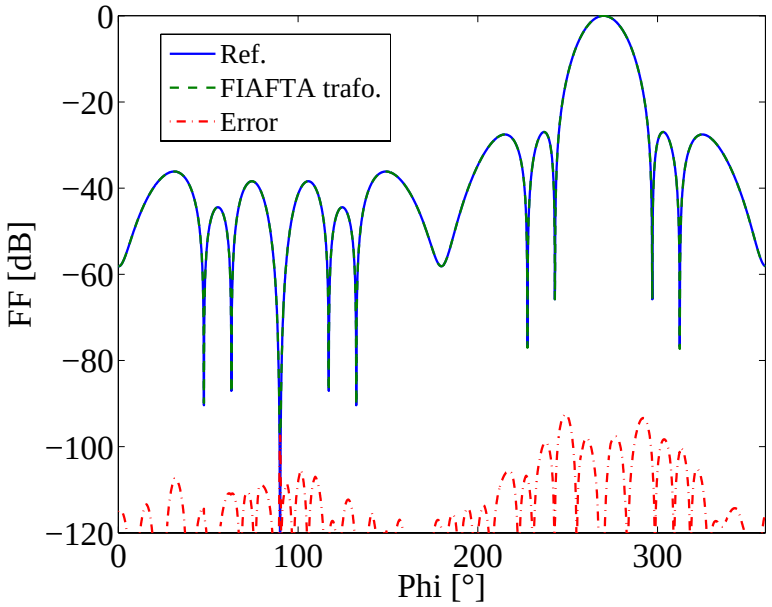

(a) E-plane pattern cut

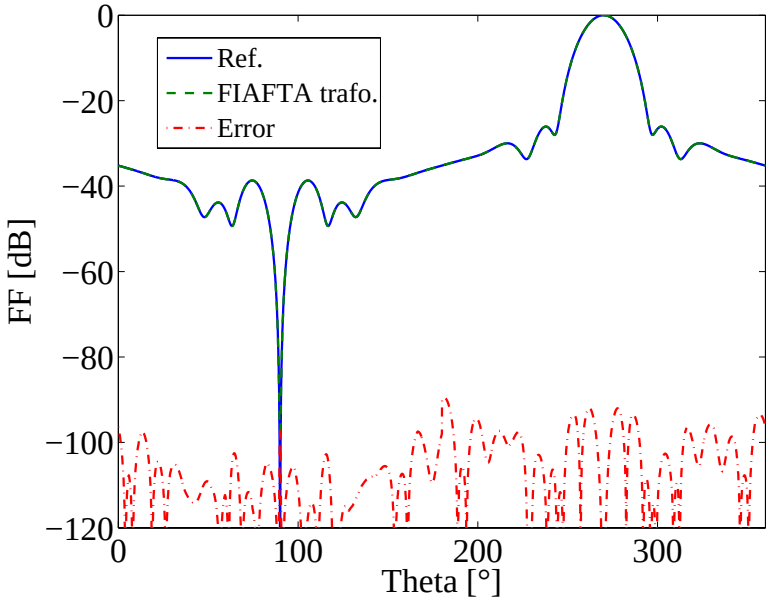

(b) H-plane pattern cut

Figure 5.3: Transformed E- and H- plane pattern cuts of horn antenna operating at 10 GHz.

amplitude and phase non-linearity, RF leakage and cross talk, random amplitude and phase error, temperature effects etc. The degree of inaccuracy in the magnitude $\triangle a$ and the phase $\triangle \psi$ is normally provided by the receiver manufacturers. Therefore, the probe output can be written as

$$U_{\mathrm{o}}(r_{\mathrm{M}}) = (a(r_{\mathrm{M}}) + \triangle a(r_{\mathrm{M}}))\, \mathrm{e}^{\mathrm{j}(\psi(r_{\mathrm{M}}) + \triangle\psi(r_{\mathrm{M}}))}, \tag{5.8}$$

where r_{M} is the measurement point. Since the exact error magnitude is unknown, one can replace $\triangle a$ and $\triangle \psi$ by their respective standard deviations $\sigma_{\mathrm{mag}}(r_{\mathrm{M}})$ and $\sigma_{\mathrm{ph}}(r_{\mathrm{M}})$

$$U_{\mathrm{o}}(r_{\mathrm{M}}) = \left(a(r_{\mathrm{M}}) + \sigma_{\mathrm{mag}}(r_{\mathrm{M}})\right) \mathrm{e}^{\mathrm{j}(\psi(r_{\mathrm{M}}) + \sigma_{\mathrm{ph}}(r_{\mathrm{M}}))} \tag{5.9}$$

and assuming the Gaussian distribution. The standard deviations σ_{mag} and σ_{ph} can now be defined according to the corresponding instrumentation error and its order of magnitude. For instance, we select the random error in the magnitude arising due to the noise addition by the receiver. A unique and effective way of representing the standard deviation is by considering the SNR of the measured signal, as defined in [2]. The available absolute noise of the receiver is taken into account and the empirically derived SNR based standard deviation is given as

$$3\sigma_{\mathrm{mag}} = 20\log_{10}\left(1 + \sqrt{\frac{0.5}{10^{\frac{\mathrm{SNR}}{10}}}}\right). \tag{5.10}$$

An SNR of 60 dB at normalized maximum pattern level (i.e. 0 dB) produces ± 0.006 dB inaccuracy using (5.10). Similarly, at -30 dB normalized pattern level the inaccuracy is ± 0.2 dB. The SNR value at the maximum pattern level can be varied according the specification of the given RF measurement setup.

The effect of any other instrumentation error can be introduced in a similar way. Once the standard deviation of the amplitude and the phase error is available, the error in the probe output U_{err} can be approximated from the available erroneous near-field data. The probe output can then be represented as $U_{\mathrm{o}} = U_{\mathrm{ef}} + U_{\mathrm{err}}$, where U_{ef} is the assumed error free near-field data. Using the linearity of the problem, the probe output

$$\boldsymbol{U}'_{\mathrm{o}} = -\mathrm{j}\frac{\omega\mu}{4\pi}\,\|C\| \cdot \tilde{\boldsymbol{J}}'_{\mathrm{o}} \tag{5.11}$$

can be modified as

$$\boldsymbol{U}'_{\mathrm{ef}} + \boldsymbol{U}'_{\mathrm{err}} = -\mathrm{j}\frac{\omega\mu}{4\pi}\,\|C\| \cdot \left(\tilde{\boldsymbol{J}}'_{\mathrm{ef}} + \tilde{\boldsymbol{J}}'_{\mathrm{err}}\right). \tag{5.12}$$

The error in the plane wave spectrum $\tilde{\boldsymbol{J}}'_{\mathrm{err}}$ is computed by solving

$$\boldsymbol{U}'_{\mathrm{err}} = -\mathrm{j}\frac{\omega\mu}{4\pi}\,\|C\| \cdot \tilde{\boldsymbol{J}}'_{\mathrm{err}} \tag{5.13}$$

and utilizing the amplitude and the phase error distributions of the near field. The normalized error spectrum $\tilde{\boldsymbol{J}}'^{\mathrm{n}}_{\mathrm{err}}$ is obtained by utilizing $\tilde{\boldsymbol{J}}'_{\mathrm{o}}$ as

$$\tilde{\boldsymbol{J}}'^{\mathrm{n}}_{\mathrm{err}} = \frac{\tilde{\boldsymbol{J}}'_{\mathrm{err}}}{\max(|\tilde{\boldsymbol{J}}'_{\mathrm{o}}|)}. \tag{5.14}$$

Since the plane wave coefficients directly represent the far field of the AUT, the estimated maximum and mean error can be calculated as

$$E^{\mathrm{est}}_{\mathrm{max}} = \max\left(20\log\left(|\tilde{\boldsymbol{J}}'^{\mathrm{n}}_{\mathrm{err}}|\right)\right), \tag{5.15}$$

$$E_{\text{mean}}^{\text{est}} = \frac{\sum \left(20\log \left(|\tilde{\boldsymbol{J}}_{\text{err}}^{\prime \text{n}}| \right) \right)}{\text{no. of plane wave coefficients}}. \tag{5.16}$$

It is emphasized that the given procedure is equally valid for arbitrary near-field measurements and only requires the commonly available uncertainty in the measured probe output. The coupling matrix $\|C\|$ takes care of the plane wave translations to the measurement points of the arbitrary grid. Therefore, the estimated error in the plane wave spectrum for the same inaccuracy in the probe output can differ for different measurement surfaces.

The use of the synthetic approach allows us to compare the estimated error with that of the actually observed error in the plane wave spectrum. The reference plane wave spectrum $\tilde{\boldsymbol{J}}_{\text{ref}}^{\prime}$ using ideal near-field data is compared with the erroneous plane wave spectrum $\tilde{\boldsymbol{J}}_{\text{o}}^{\prime}$ and the "reference" maximum and mean errors are computed as

$$E_{\text{max}}^{\text{ref}} = \max \left(20\log \left(|\tilde{\boldsymbol{J}}_{\text{o}}^{\prime}| - |\tilde{\boldsymbol{J}}_{\text{ref}}^{\prime}| \right) \right) \tag{5.17}$$

$$E_{\text{mean}}^{\text{ref}} = \frac{\sum \left(20\log \left(|\tilde{\boldsymbol{J}}_{\text{o}}^{\prime}| - |\tilde{\boldsymbol{J}}_{\text{ref}}^{\prime}| \right) \right)}{\text{no. of plane wave coefficients}}. \tag{5.18}$$

The directivity

$$D_{\text{AUT}} = 10\log \left(\frac{4\pi}{\sum\limits_{k_\phi} \sum\limits_{k_\theta} \tilde{\boldsymbol{J}}^{2}(k_\phi, k_\theta)\, W(k_\theta)} \right) \tag{5.19}$$

of the AUT is also computed following the same methodology and the estimated error in the directivity is computed using $\tilde{\boldsymbol{J}}_{\text{err}}^{\prime \text{n}}$. The reference error $D_{\text{err}}^{\text{ref}}$ in the directivity is obtained by subtracting D_{ref} from D_{o}. The normalized plane wave spectra were used to compute the erroneous and the reference directivities. The $W(k_\theta)$ factor in (5.19) represents the weighting factor of the Gauss-Legendre quadrature used for the discrete representation of the spectral integral [46].

To validate the given error model, we superimpose randomly distributed magnitude errors (given by (5.10)) assuming 50 dB SNR at the normalized maximum pattern level and phase errors with a standard deviation $\sigma_{\text{ph}} = 1^\circ$ on the unperturbed near-field data of the horn antenna. A different realization but with the same standard deviation is used to compute the error in the plane wave spectrum. The observed error in the plane wave spectrum using perturbed near-field data and the estimated error using only the error distribution in the probe output for spherical measurements are then compared. The behavior is shown in Fig. 5.4. The analysis is extended to cylindrical and planar near-field measurements as well and the resulting error values are composed in Table 1. A square shaped planar measurement surface (xz) at y=-0.4 m is used to collect the near-field data. The length and the width of the planar surface are 1.5 m each which makes a valid angle of 60°. Similarly, the radius and the height of the cylindrical surface used is 0.4 m and 1 m, respectively, with AUT looking in -y direction and makes a valid angle of 48° in the E-plane pattern. The good agreement noticed in the estimated and the observed uncertainty in the transformed pattern clearly shows that if the magnitude of the near-field error is known, one can estimate the uncertainty in the far field very accurately.

5.6 Errors Affecting the Probe Correction Coefficients

Probe parameter errors include errors affecting the probe correction coefficients $\boldsymbol{P}(.,.,.,.)$ in (4). The errors include probe pattern inaccuracy, probe polarization ratio, probe gain, and probe alignment

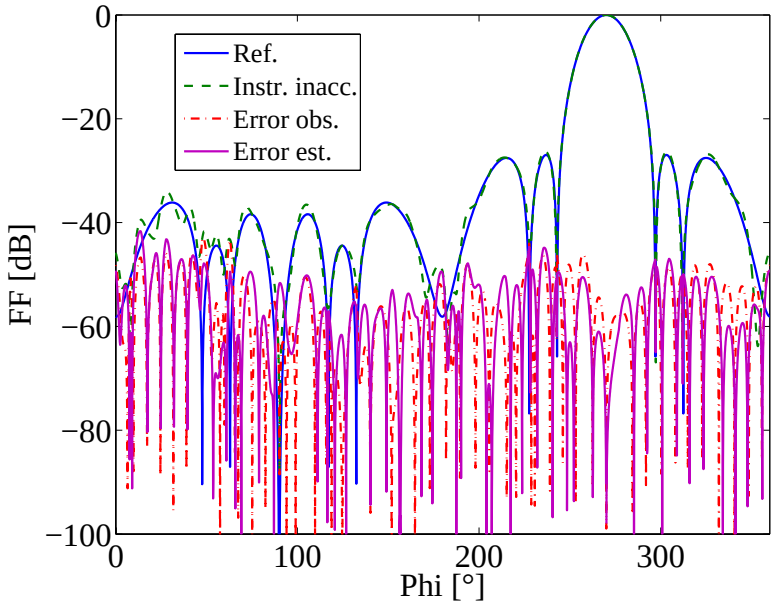

(a) E-plane pattern cut

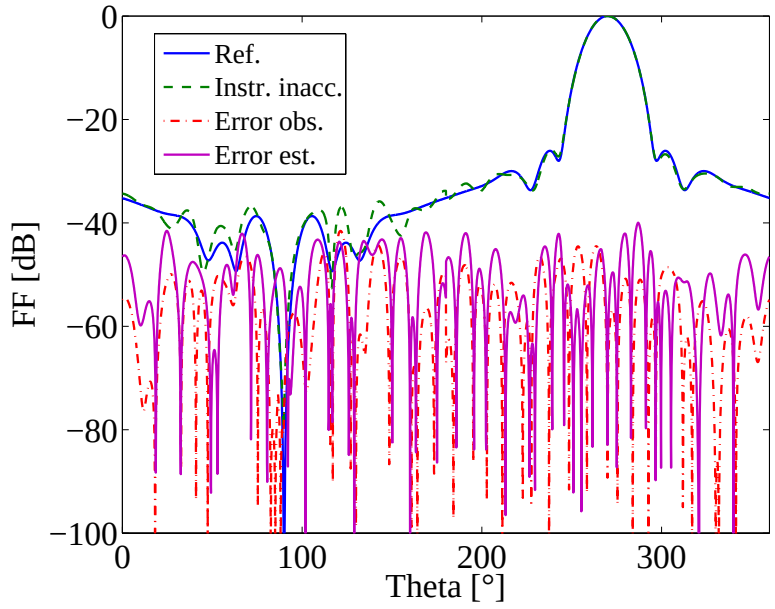

(b) H-plane pattern cut

Figure 5.4: Transformed E- and H-plane pattern cuts of horn antenna using spherical near-field data contaminated with random magnitude and phase error.

errors. Any such error directly affects the accuracy of the coupling matrix elements

$$C_{\phi/\theta}(k_{\phi p}, k_{\theta q}, \phi_m, \theta_n) = T_L(\hat{k}, \boldsymbol{r}_{\mathrm{M}}) W(k_{\theta q}) P\left(k_{\phi p}, k_{\theta q}, \phi_m, \theta_n\right) \tag{5.20}$$

and in turn deteriorates the transformed radiation pattern. The number of integration points $p = 1, ..., P$ and $q = 1, ..., Q$ in ϕ- and θ-direction, respectively, are used in the above equation. Using an analogous procedure as described in the previous section, we split the erroneous probe

Table 5.1: Far-field uncertainty [dB] in the transformed E- and H-plane pattern cuts due to random errors for horn antenna operating at 10 GHz.

Grid	Random Errors									
	E-plane				H-plane				D_{AUT}	
	mean err		max err		mean err		max err		error	
	est.	ref.	est.	ref.	est.	ref.	est.	ref.	est.	ref.
Spherical	-57	-56	-43	-43	-56	-57	-41	-42	0.01	0.01
Cylindrical	-59	-59	-48	-49	-59	-60	-45	-45	0.01	0.01
Planar	-69	-66	-48	-44	-70	-71	-49	-52	0.00	0.00

correction coefficient into an error free $\boldsymbol{P}_{\text{ef}}(.,.,.,.)$ and a probe error part $\boldsymbol{P}_{\text{err}}(.,.,.,.)$ according to

$$C_{\phi/\theta}(k_{\phi p}, k_{\theta q}, \phi_m, \theta_n) = T_L(\hat{k}, \boldsymbol{r}_{\text{M}}) W(k_{\theta q}) \\ \left[P_{\text{ef}}\left(k_\phi, k_\theta, \phi_m, \theta_n\right) + P_{\text{err}}\left(k_{\phi p}, k_{\theta q}, \phi_m, \theta_n\right)\right]. \tag{5.21}$$

Accordingly, the coupling matrix elements can also be divided into two parts

$$C_{\text{ef}}(k_{\phi p}, k_{\theta q}, \phi_m, \theta_n) + C_{\text{err}}(k_{\phi p}, k_{\theta q}, \phi_m, \theta_n) = T_L(\hat{k}, \boldsymbol{r}_{\text{M}}) W(k_{\theta q}) \\ \left[P_{\text{ef}}\left(k_\phi, k_\theta, \phi_m, \theta_n\right) + P_{\text{err}}\left(k_{\phi p}, k_{\theta q}, \phi_m, \theta_n\right)\right] \tag{5.22}$$

and the probe output is modified as

$$\boldsymbol{U}'_{\text{o}} = -\text{j}\frac{\omega\mu}{4\pi}\left(\|C\|_{\text{ef}} + \|C\|_{\text{err}}\right) \cdot \tilde{\boldsymbol{J}}'_{\text{o}}. \tag{5.23}$$

A known uncertainty in the probe alignment, probe pattern inaccuracies and other probe errors allow us to compute $\|C\|_{\text{err}}$ which in combination with the plane wave spectrum $\tilde{\boldsymbol{J}}'_{\text{o}}$ gives the uncertainty in the probe output

$$\boldsymbol{U}'_{\text{err}} = -\text{j}\frac{\omega\mu}{4\pi}\|C\|_{\text{err}} \cdot \tilde{\boldsymbol{J}}'_{\text{o}}. \tag{5.24}$$

Once the uncertainty in the probe output is obtained, the error in the plane wave spectrum $\tilde{\boldsymbol{J}}'_{\text{err}}$ can be computed using

$$\boldsymbol{U}'_{\text{err}} = -\text{j}\frac{\omega\mu}{4\pi}\|C\| \cdot \tilde{\boldsymbol{J}}'_{\text{err}}. \tag{5.25}$$

The directivity, estimated mean and the maximum error can then be computed using (5.17), (5.18), and (5.19).

To examine the effectiveness of the given procedure, we introduce randomly generated magnitude error in the probe patterns used for the probe correction of the horn antenna. The erroneous plane wave spectrum $\tilde{\boldsymbol{J}}'_{\text{o}}$ is determined using the perturbed probe patterns. The uncertainty in the $\tilde{\boldsymbol{J}}'_{\text{o/p}}$ is then approximated by using another randomly generated error distribution[2] and following the above mentioned procedure. The observed and the estimated error in the transformed E and H-plane cuts for spherical measurements is shown in Fig. 5.5. The transformed pattern shows stability against magnitude errors in the probe pattern and good agreement in the observed and the estimated errors is seen. Table 2 summarizes the estimated and the reference error values for spherical, cylindrical, and the planar scanning surfaces.

[2]The standard deviation used to generate the error distribution, however, is the same and uses 50 dB SNR at the normalized maximum pattern level.

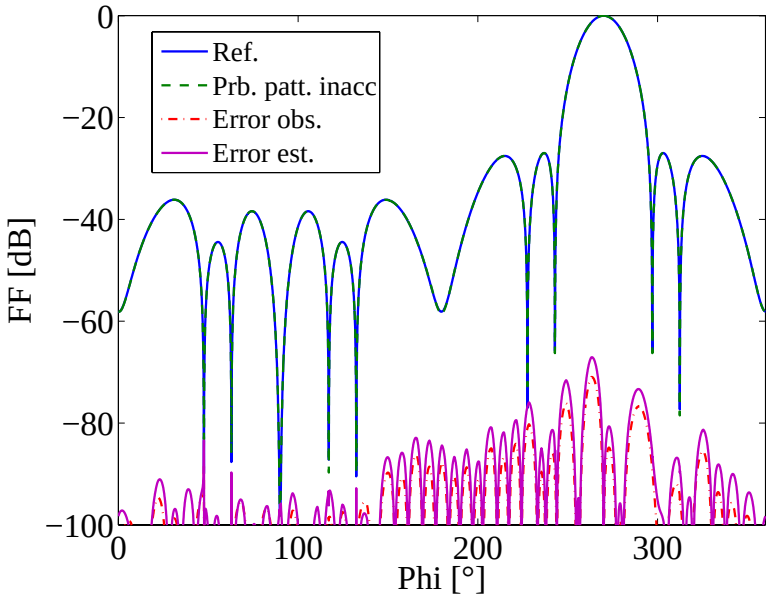

(a) E-plane pattern cut

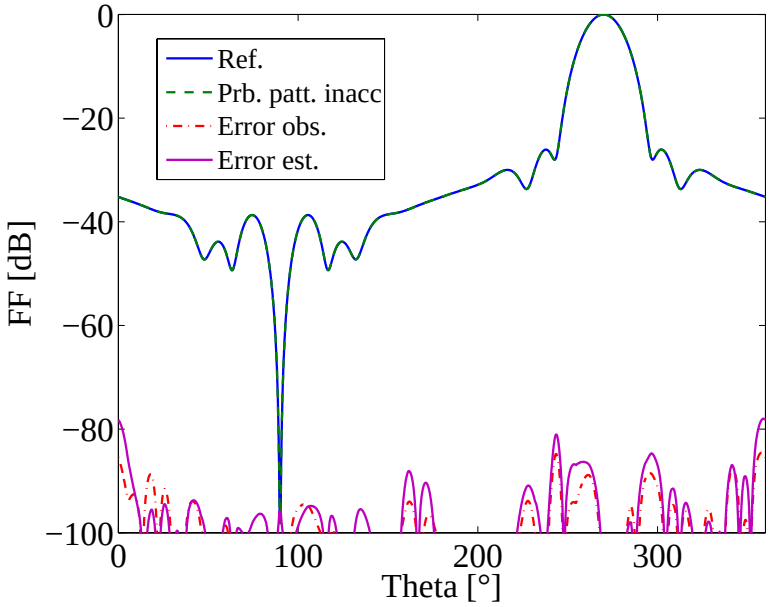

(b) H-plane pattern cut

Figure 5.5: Transformed E- and H-plane pattern cuts of horn antenna using near-field data contaminated with probe pattern errors.

5.7 Errors Affecting the Translation Operator

The positioning system used in near-field measurements can mark the position of the measurement point with an accuracy of several tens of micrometers. No matter how small the position error is, it results in the inaccurate translation of the plane wave spectrum and introduces uncertainties in the transformed pattern. The relative error in the x, y, and z coordinates i.e. δx, δy, and δz of the probe position can be determined using optical measurements. We make use of the position

Table 5.2: Far-field uncertainty [dB] in the transformed E- and H-plane pattern cuts due to probe pattern error for horn antenna operating at 10 GHz.

Grid	Probe Pattern Error									
	E-plane				H-plane				D_{AUT}	
	mean err		max err		mean err		max err		error	
	est.	ref.	est.	ref.	est.	ref.	est.	ref.	est.	ref.
Spherical	-100	-100	-71	-71	-105	-99	-98	-86	0.00	0.00
Cylindrical	-85	-87	-66	-67	-90	-90	-66	-66	0.00	0.00
Planar	-105	-104	-64	-66	-101	-99	-62	-63	0.00	0.00

inaccuracy to determine the uncertainty in the transformed pattern. The erroneous measurement point

$$\boldsymbol{r}_{\text{M}} + \delta\boldsymbol{r}_{\text{M}} = (x + \delta x)\boldsymbol{a}_x + (y + \delta y)\boldsymbol{a}_y + (z + \delta z)\boldsymbol{a}_z \tag{5.26}$$

is now a combination of the actual measurement point $\boldsymbol{r}_{\text{M}}$ and the inaccuracy $\delta\boldsymbol{r}_{\text{M}}$. Consequently, the modified translation operator is rewritten as

$$\begin{aligned} T_L(\hat{k}, \boldsymbol{r}_{\text{M}} + \delta\boldsymbol{r}_{\text{M}}) = -\,\mathrm{j}\frac{k}{4\pi}\sum_{l=0}^{L}(-\mathrm{j})^l\,(2l+1) \\ \mathrm{h}_l^{(2)}\left(k\left(r_{\text{M}} + \delta r_{\text{M}}\right)\right)\mathrm{P}_l(\hat{k}\cdot(\hat{r_{\text{M}}} + \delta\hat{r_{\text{M}}})). \end{aligned} \tag{5.27}$$

It is worth mentioning here that one cannot use the error in the probe position $\delta\boldsymbol{r}_{\text{M}}$ directly to compute the error in the translation operator. This would simply mean as if the translations are performed considering the position error as the actual position. The inaccuracy in the translation operator

$$T_{L\text{err}} = T_L(\hat{k}, \boldsymbol{r}_{\text{M}} + \triangle\boldsymbol{r}_{\text{M}}) - T_L(\hat{k}, \boldsymbol{r}_{\text{M}}) \tag{5.28}$$

is used to compute the erroneous coupling matrix

$$C_{\text{err}}(k_{\phi p}, k_{\theta q}, \phi_m, \theta_n) = T_{L\text{err}} W(k_\theta) P\left(k_\phi, k_\theta, \phi_m, \theta_n\right). \tag{5.29}$$

Afterwards, the error in the probe output

$$\boldsymbol{U}'_{\text{err}} = -\mathrm{j}\frac{\omega\mu}{4\pi}\left\|C\right\|_{\text{err}} \cdot \tilde{\boldsymbol{J}}'_{\text{o}} \tag{5.30}$$

$$\boldsymbol{U}'_{\text{err}} = -\mathrm{j}\frac{\omega\mu}{4\pi}\left\|C\right\| \cdot \tilde{\boldsymbol{J}}'_{\text{err}} \tag{5.31}$$

and the error in the plane wave spectrum is used along with (5.17), (5.18), and (5.19) to compute the estimated mean and the maximum error.

The behavior of FIAFTA against probe positioning errors is analyzed by adding a randomly distributed error in the probe coordinates. A realistic standard deviation in the probe coordinates σ_x=σ_y=σ_z= 50 μm is chosen and the resulting error in the transformed pattern is compared with the estimated mean and maximum error. The transformed E- and H-plane pattern cuts of the horn antenna with observed and estimated error for spherical measurements are shown in Fig. 5.6. A slightly high error level is noticed for the spherical transformation in the equator region. It is due to the fact that equidistant spacing in θ and ϕ is used to generate the spherical grid for the near-field acquisition. Such equidistant distribution tends to accumulate more sampling points along

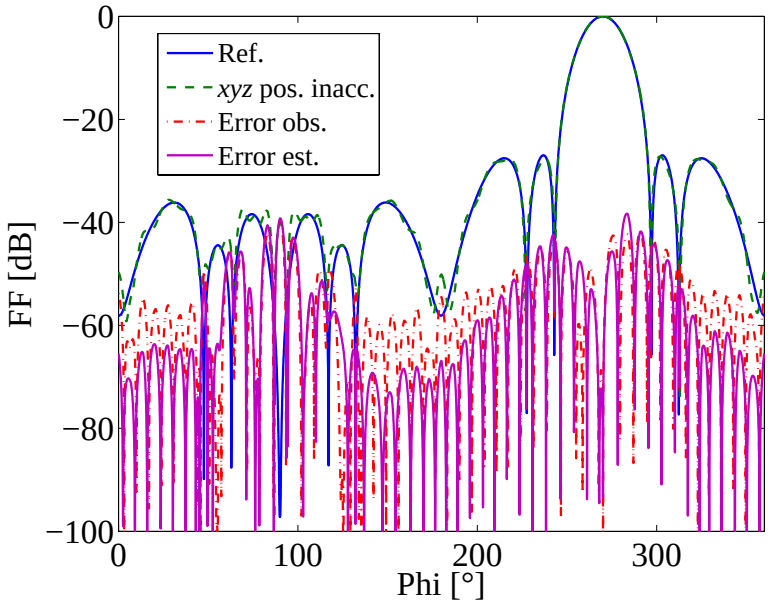

(a) E-plane pattern cut

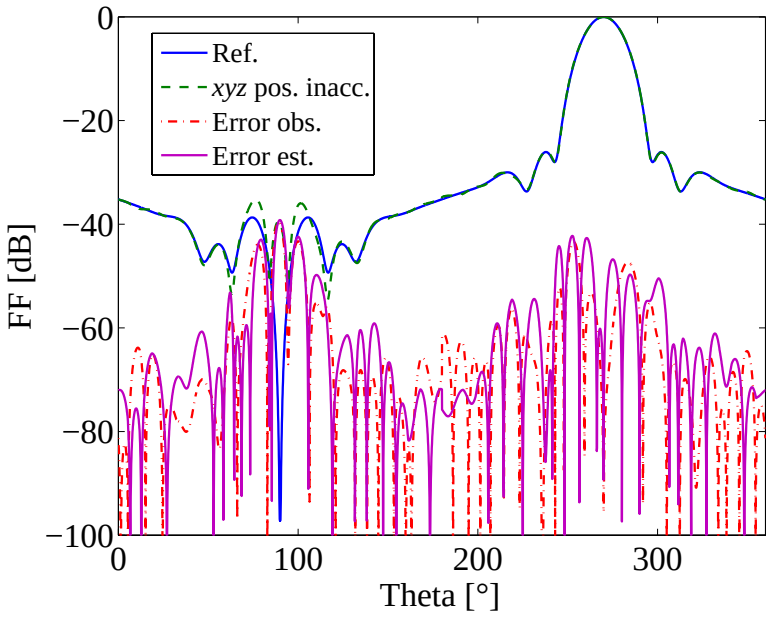

(b) H-plane pattern cut

Figure 5.6: Transformed E- and H- plane pattern cuts using spherical near-field data of horn antenna incorporating probe position inaccuracy.

the polar region. Any error in the probe position is compensated to some extent due to redundant information at polar regions with more samples while the equator i.e. the main beam and the back lobe region directly reflects the error behavior. The analysis is also extended for the cylindrical and planar scanning surfaces and the error values are summarized in Table 3. Again, a good agreement in the estimated and the references error values is seen.

The schematic summarizing the analysis for instrumentation, probe parameter, and probe po-

Table 5.3: Far-field uncertainty [dB] in the transformed E- and H-plane pattern cuts due to probe position error for horn antenna operating at 10 GHz.

Grid	Probe Position Error									
	E-plane				H-plane				D_{AUT}	
	mean err		max err		mean err		max err		err	
	est.	ref.	est.	ref.	est.	ref.	est.	ref.	est.	ref.
Spherical	-61	-54	-43	-42	-64	-64	-43	-43	0.01	0.02
Cylindrical	-70	-68	-49	-53	-58	-59	-36	-43	0.00	0.00
Planar	-70	-70	-52	-48	-70	-74	-53	-52	0.01	0.00

sitioning errors is shown in Fig. 5.7. By following the mentioned steps one can estimate the maximum and the mean uncertainty in the transformed far-field pattern.

5.8 Other Errors

The errors falling in this category do not directly effect probe output, probe radiation pattern, or the translation operator but have an inherent effect in near-field measurements. In the following, we discuss these errors with their effect on the transformed pattern along with any correction technique available.

5.8.1 Measurement Area Truncation

Scan area truncation is one of the unavoidable sources of error in planar and cylindrical near-field measurements. As explained before, the inability to measure the near field on a surface with infinite extent results in limiting the radiation behavior of the AUT to a certain reliable region. The assumption of zero near field outside the scan area or its periodic repetition introduces errors within the valid region as well. However, the behavior of FIAFTA against scan area truncation is found to be more robust [1] as compared to the traditional transformation techniques. The better performance comes from the fact that, unlike other plane wave based approaches, FIAFTA uses the entire Ewald sphere for the representation of the plane wave sources. Also, FIAFTA first transforms the measured data to the source plane to determine the coefficients for equivalent sources from which the far field is ascertained. The use of the complete Ewald sphere and the fact that FIAFTA involves an intermediate step to determine equivalent plane wave sources, unlike 2D FFT based approaches, helps in reducing the truncation error [63] and avoids ripples in the far-field pattern. The ripples can also be eliminated by using a direct non-redundant NFFF transformation in a cylindrical scanning geometry as proposed by D'Agostino et al. in [100]. The overall effect of scan area truncation can be assumed negligible if the truncation level at the edges of the scan plane is $\leq$-40 dB. Since FIAFTA can handle measurements on arbitrary grids, the valid angle of the radiation pattern can be significantly increased by utilizing adaptive sampling in planar and cylindrical measurements [2][6]. In the adaptive sampling, a certain measurement area is scanned in the beginning with the regular sampling and afterwards an SNR based decision criterion helps us to determine the key locations from where the near field should be acquired using adaptive sampling. The measurement burden can be reduced by decreasing the number of sampling points as much as 47%. More details about the adaptive technique will be explained in Chap. 6.

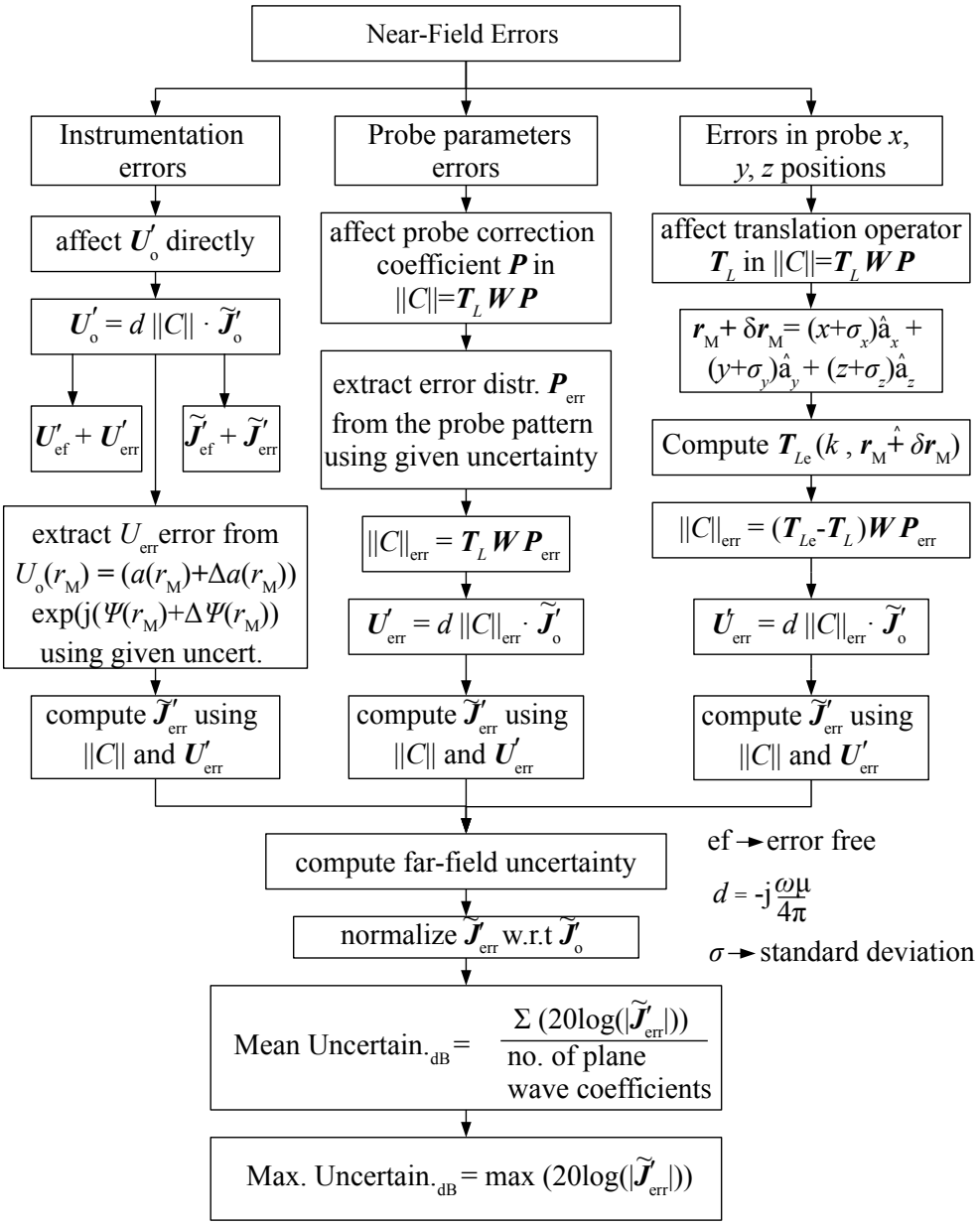

Figure 5.7: Schematic of the near-field measurement error analysis.

5.8.2 Sample spacing

The spacing between the sample points on the near-field scanning surface greatly affects the accuracy of the transformed far field. $\lambda/2$ sample spacing is commonly adopted along the length of the cylinder in the standard cylindrical and in the planar measurements due to FFT usage. Sample spacings coarser than $\lambda/2$ result in aliasing errors [42]. However, no such limitation applies to FIAFTA and the sample spacing is computed in relation with the number of unknowns required to

solve the linear system of equations. The required spacing in θ and ϕ is

$$\triangle\phi = \pi/(\alpha_1 L_{\text{AUT}}) \tag{5.32}$$

$$\triangle\theta = \pi/(\alpha_2 L_{\text{AUT}}) \tag{5.33}$$

where α_1 and α_2 are the proportionality constants with empirical values[3] slightly greater than 1 and $L_{\text{AUT}} = kd_a/2 + 10$ is the antenna multipole number with d_a as the diameter of the minimum sphere enclosing the antenna. Once the spacing in θ and ϕ is determined, the samples are efficiently distributed on the spherical surface and can then be mapped to planar [8], cylindrical, or any arbitrary surface. As long as the given sampling criteria are satisfied, negligible errors in the transformed pattern are observed. The extensive analysis for the determination of sampling criteria is carried out in Chap. 6.

5.8.3 Multiple reflections

As described in Chap. 4, it is common practice to place the scan plane near the AUT so that the valid angle can be efficiently increased. Nonetheless, it results in strong interaction between the AUT and the probe and the resulting multiple reflections deteriorate the measured data especially for planar measurements. Yaghjian in [61] tried to establish the upper bound due to multiple reflection errors which predicts very large errors. Estimating multiple reflection errors is extremely difficult as it varies according to the choice of the probe and the separation between the AUT and the probe. However, it can be reduced by acquiring the central near-field data on a plane at a large distance and at another plane at smaller distance but collecting the near field from the boundary region and processing the acquired data using FIAFTA. In this way, one can reduce the effect of multiple reflection errors while keeping a larger valid angle and less time consumption. The concept is validated in [4] for planar measurements and is equally applicable for cylindrical measurements (see Fig. 5.8). The length L_1 of the outer cylinder can be determined in a similar fashion as described in [4] and is given as

$$L_1 = \frac{1}{r}(ar_1(x-1) + ar) \tag{5.34}$$

where r_1 and r are the radius of the outer and the inner cylinder, respectively.

5.8.4 Room scattering

The near-field probe receives direct as well as multipath signal scattered from different objects. The effect on the measured near field is more pronounced if the measurement is performed in a semi-anechoic chamber. However, FIAFTA has the ability to alienate the contribution of multipath signals by attributing the echo contributions to scattering centres with or without the knowledge of the location of echo sources [79]. The modified linear system of equations is

$$\boldsymbol{U'} = -j\frac{\omega\mu}{4\pi}\|C\|_{\text{AUT}} \cdot \tilde{\boldsymbol{J}} - j\frac{\omega\mu}{4\pi}\sum_{i=1}^{N_{\text{SC}}}\|C\|_{\text{SC}i} \cdot \tilde{\boldsymbol{J}}_{\text{SC}i}, \tag{5.35}$$

where $\|C\|_{\text{SC}i}$ represent the coupling matrices for the i_{th} scattering center and N_{SC} is the number of scattering centres employed. Significant improvement has been reported in comparison to the case when no echo suppression is applied [79]. The NFFF transformations based on the nonredundant representation of electromagnetic field also allow to cut away the echo contributions outside the antenna spatial bandwidth, due to the low pass filtering properties of the employed interpolation functions, as stated in [80].

[3] The optimum value of α_1 and α_2 depends on the noise conditions and other systematic errors.

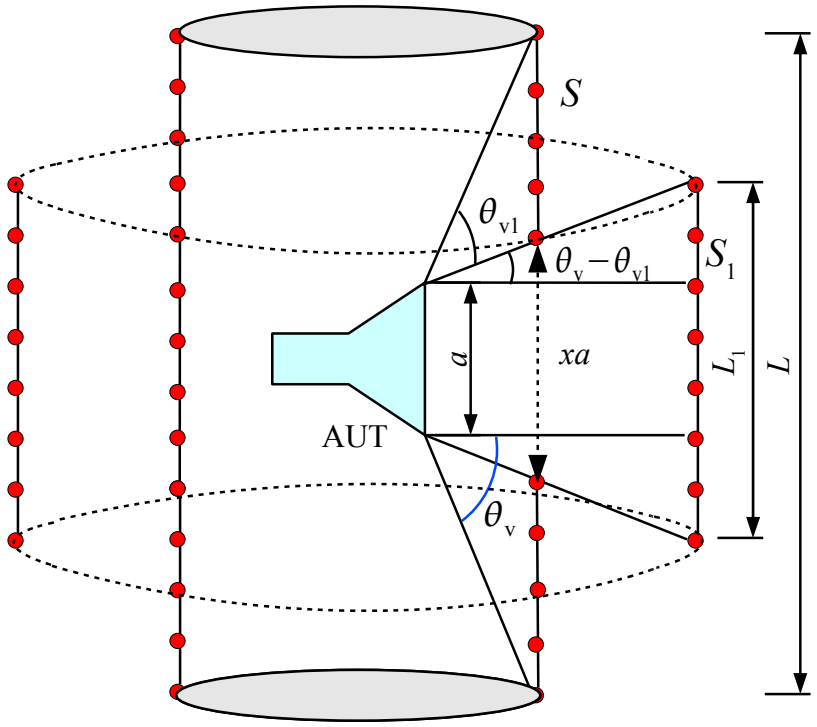

Figure 5.8: Proposed measurement setup for reduced AUT-probe interaction in cylindrical near-field measurements.

5.9 Short Summary

It has been shown that the effect of any arbitrary near-field error can be determined by making use of the erroneous near-field data and the magnitude of the error. The formulation of FIAFTA allows us to differentiate between the contribution of errors in the transformed far field. The errors have been broadly divided according to their direct effect on the probe output, probe correction coefficients, and the translation operator. Apart from that, other errors inherent in the near-field data have also been discussed.

Chapter 6

Adaptive Near-Field Data Acquisition

It has been observed during the error analysis of FIAFTA that it can handle a larger sample spacing than $\lambda/2$ which is usually applied in planar measurements and in the vertical direction of the cylindrical measurements. However, there are various concerns in the practical setup which should be considered. The practical limit on the number of required samples is set by the noise and error conditions during the measurements. For instance, consider the testing of phased array antennas with some faulty arrays. In a normal setup, the abrupt changes in the near-field magnitude will go unnoticed if a coarser sampling is applied in the region containing variations due to faulty arrays. Therefore, an intelligent scanning is required which tend to decrease measurement burden while capturing the essential information. Many techniques have been proposed in the past but with some concerns. In the following, these techniques are reviewed.

As earlier stated, planar near-field antenna measurements are appropriate for medium and high gain antennas and ideally require measurements on an infinite plane. Reducing the scan plane size, due to practical limitations, reduces the reliable region of the far-field pattern and also introduces truncation errors within the reliable region [42]. On the other hand, increasing the scan plane size would directly result in an increased testing time. Several methods have been proposed in the recent past to cope with the truncation effects. This would allow a larger reliable region while keeping the smaller scan size, hence reducing the measurement time. One method [85] uses a set of equivalent magnetic currents over a fictitious planar surface to characterize the antenna. The near-field is related to the equivalent magnetic currents using integral equation. This method provides a larger reliable region as compared to modal expansion methods in which radiated antenna fields are expanded in terms of planar wave functions [63]. As stated by the author, the method is not suitable for highly directive antennas [85] dissolving the major benefit of planar near-field (PNF) measurements. Another method in [72] utilizes *a priori* information i.e. the size of the antenna and ”recovers” the lost information content due to the area truncation by employing the sampling theory. However, the effectiveness of this method depends on the fact that the probe can also move in a direction perpendicular to the measurement plane which eventually increases measurement time. The Gerchberg-Papoulis iterative algorithm is applied in [86] to extrapolate the plane wave spectrum of the field radiated by the antenna to overcome the truncation problem. Back-projections and re-adjustments are recursively applied to the originally determined plane wave spectrum until the given convergence criterion is met. This method of projections is prone to so-called traps and tunnels and may not converge [87]. In another approach in [73], the near-field data is extrapolated outside the measurement region by employing the optimal sampling interpolation (OSI) expansions instead of cardinal series (CS) ones. The comparison between OSI and CS based approach is performed afterwards using numerical simulations and significant enlargement of the valid far-field region is reported. A similar non-redundant sampling representation in an electromagnetic

field based approach is applied in bipolar scanning for extrapolating near-field values outside the measurement plane in [88]. The external data is estimated by employing a singular value decomposition method and using OSI expansions. A significant decrease in the truncation errors occurring in near-field far-field transformations is reported for bipolar scanning.

An effective planar spiral scanning technique described in [89] utilizes ellipsoidal modelling of the source [90] instead of the spherical one. The said technique gives the freedom of considering measurement planes at distances smaller than one half of the antenna size and therefore increases the valid angle associated with the size of the scan plane for quasi-planar antennas. The technique works well as long as the decreased separation does not increase the multiple reflections between the AUT and the probe. The planar wide-mesh scanning is applied in [92] with sample spacing greater than half-wavelength when moving away from the center of the scanning region. The amount of required near-field data is significantly reduced without decreasing the accuracy and no drastic change is required in an existing plane-rectangular facility. Although the number of sampling points are reduced, the effect on the acquisition time is not reported.

Recently, an adaptive acquisition technique has been proposed in [93] to reduce the measurement time by rectangular spiral scanning of the probe. It considerably reduces the measurement time by terminating the measurement process when a specific accuracy is reached dependent on a decision factor. The decision factor, as explained in [93], is based on either the first side lobe level pattern difference or the directivity of the given AUT. It is shown that a considerable decrease in the acquisition time can be achieved if the measurement process is terminated optimally [94]. Nevertheless, if the measurement is terminated at a smaller scan plane size the reliable region is also reduced accordingly. Also, NFFF transformations after each rectangular ring acquisition make it difficult to use transformation algorithms employing integral equations which usually require long computation times.

In this chapter, we present a simple approach to reduce the measurement time in PNF measurements. In contrast to the adaptive acquisition in [93], the valid angle is not reduced and as such no extra measurement step is required. The measurement system adapts itself during the measurement process and based on a given decision threshold, it concentrates mainly on the strongly changing near-field regions while skipping data points from smoothly varying locations. However, the extent at which the measurement time is reduced depends on the near-field distribution. Best results have been achieved for antennas with smoothly varying near-fields. The irregular grid obtained as a result of adaptive scanning is processed using the FIAFTA.

6.1 Near-Field Acquisition

6.1.1 Rectangular Spiral Planar Acquisition

It is recognized that the distribution of the near field on the measurement plane is of prime importance containing more degrees of freedom in suddenly changing regions compared to smoothly varying locations within the scan plane. Therefore, avoiding data points from smooth areas and thereby saving measurement time will have a negligible effect on the radiation pattern of the AUT. To determine sudden variations during the measurement process, a ring shaped data acquisition approach is proposed for planar measurements. The data acquisition starts from the center of the scan plane and steps in the outward direction away from the center. In the beginning,

the main beam data is obtained until the m^{th} ring.[1] Using the acquired data, the magnitude of the near-field $U_{\text{ext}}^{(m+2)}$ is extrapolated at the measurement points of the $(m+2)$ ring while skipping the $(m+1)$ ring. Afterwards, sampling points of $(m+2)$ ring are measured providing $U_{\text{meas}}^{(m+2)}$. The logarithmic differences between the extrapolated and the measured values

$$D^{(m+2)} = 20\log_{10}(\text{abs}(U_{\text{ext}}^{(m+2)} - U_{\text{meas}}^{(m+2)})) \tag{6.1}$$

determine whether the corresponding points from the $(m+1)$ ring can be skipped or not. The list containing sampling points is constantly updated and once the probe finishes traversing the $(m+2)$ ring, it steps back to the $(m+1)$ ring and measures only the non-skipped points. It is worth mentioning here that extrapolated near-field values are only used to locate the unexpected change in the near field magnitude and are not used in the NFFF transformation itself so any standard extrapolation technique can serve the purpose. We utilize Piecewise Cubic Hermite Interpolation (pchip) to extrapolate out of range values. Fig. 6.1 shows a measurement plane divided into a rectangular ring structure.

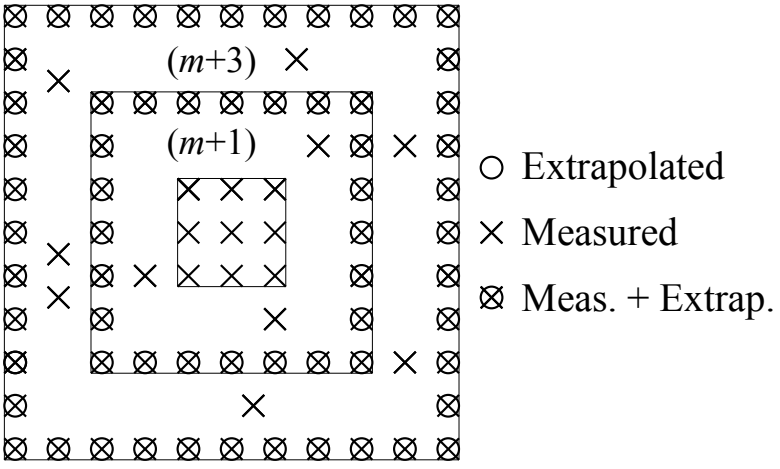

Figure 6.1: Measurement plane dividing sampling points into rectangular rings. Depending on the difference in the extrapolated and the measured values of (m+2) ring points, selected points have been measured in (m+1) ring.

6.1.2 Adaptive Cylindrical Scanning Methodology

The standard sampling criterion used for cylindrical measurements includes the radius of the minimum cylinder containing the AUT as

$$\triangle\phi \leq \frac{2\pi}{2N+1} \quad \text{with} \quad N = k\frac{d}{2} + 10, \tag{6.2}$$

where d is the diameter of the minimum cylinder enclosing the antenna. For cylindrical measurements, $\lambda/2$ spacing is used in the vertical direction. A standard cylindrical scanning technique

[1] It is assumed here for simplicity that the main beam lies in the center of the scan plane. However, if the main beam does not lie in the center or the exact location of the main beam is not known, data acquisition can be started from any other part of the scan plane provided that the main beam would lie in that specific portion acquired in the beginning.

involving movement the probe in the vertical direction while sweeping in ϕ is chosen with a little amendment. After acquiring a specific number of vertical lines ($(m\pm1)$ in our case) from the main beam direction (m^{th} line), the $(m+3)^{\text{th}}$ line is extrapolated to obtain $U_{\text{ext}}^{(m+3)}$. Near-field measurement at $(m+3)$ then provides $U_{\text{meas}}^{(m+3)}$. The logarithmic difference between the extrapolated and the measured values

$$D^{(m+3)} = 20\log_{10}(\text{abs}(U_{\text{ext}}^{(m+3)} - U_{\text{meas}}^{(m+3)})) \tag{6.3}$$

now determines whether the corresponding values from the $(m+2)^{\text{th}}$ line can be skipped or not. Once the probe finishes traversing the $(m+3)^{\text{th}}$ line it steps back to the $(m+2)^{\text{th}}$ and measures only the required points. Both traditional and proposed scanning techniques are shown in Fig. 6.2. Blue dots represent extrapolated as well as measured points while the red dots mention only the measured points. A similar technique can also be applied for cylindrical scanning which involves sweeping the AUT in ϕ while stepping in z-direction.

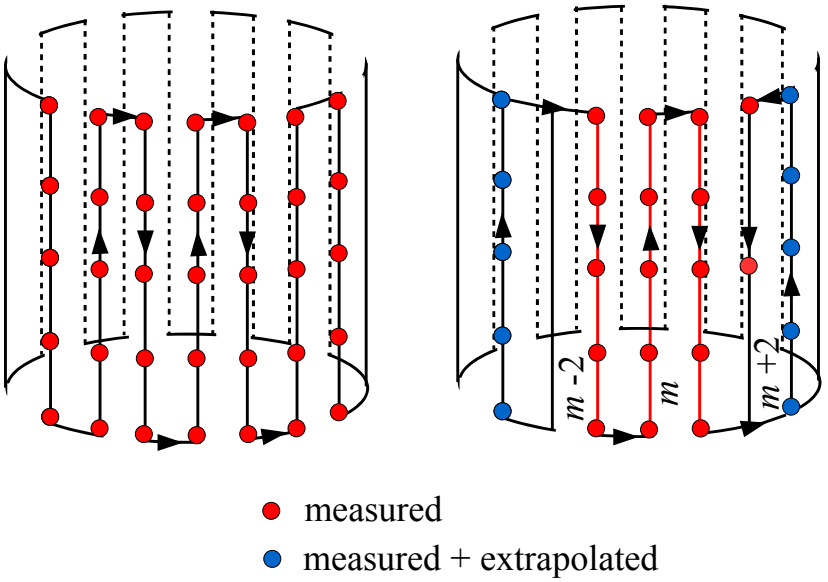

Figure 6.2: Traditional vs. proposed cylindrical scanning.

6.1.3 Adaptive Spherical Near-Field Acquisition

Spherical scanning involves movement of the probe in one angular direction (ϕ or θ) while stepping in the other one. The spacing in ϕ and θ are the same and given as

$$\triangle\phi, \triangle\theta \leq \frac{2\pi}{2N+1} \quad \text{with} \quad N = k\frac{d}{2} + 10. \tag{6.4}$$

Only one case of spherical scanning is described here (i.e. scan in ϕ and step in θ) and a similar approach can be extended for the second case. Like cylindrical scanning, a specific number of

circular rings ($(m \pm 1)$ in our case) are acquired in the beginning from the centre. After skipping an intermediate ring the near field is extrapolated and measured at the $(m+3)^{\text{th}}$ ring. Eq. (6.3) is then used to find the logarithmic difference between the two and the $(m+2)$ ring points are skipped accordingly. Fig. 6.3 shows the geometrical arrangement of the proposed spherical scanning.

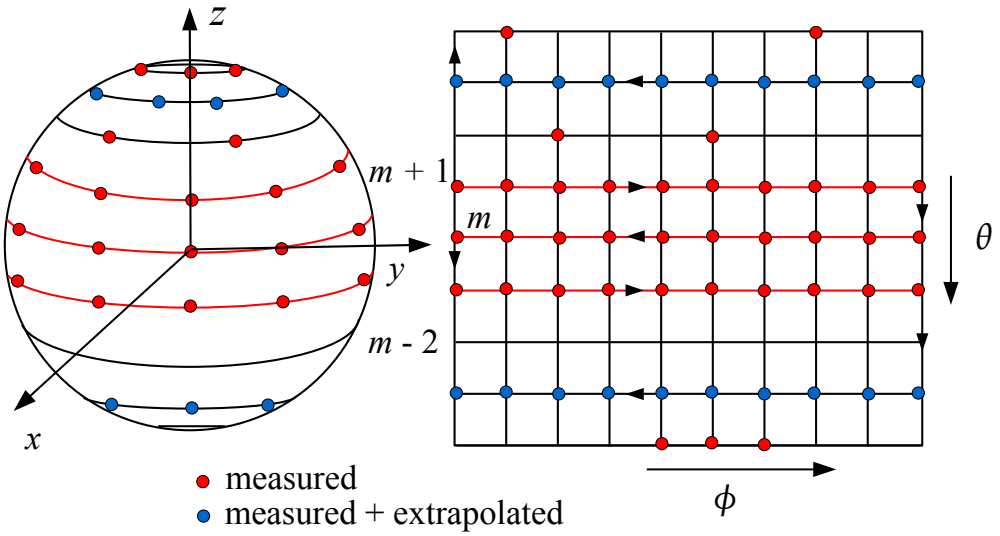

Figure 6.3: Proposed spherical scanning.

6.1.4 Decision Criterion

A suitable choice of decision criterion will determine the threshold difference ($D_{\text{th}}^{(m+2)}$ for planar and $D_{\text{th}}^{(m+3)}$ for spherical and cylindrical near-field acquisition) for skipping data points. Obviously, one cannot use a fixed value for all the data points as it should vary with the near field magnitude for reliable results. A unique way is introduced to define the decision criterion based on signal-to-noise ratio (SNR) of the received signal. An SNR of 60 dB[2] (can be varied) is assumed at the maximum pattern level and is decreased down to 30 dB at 30 dB below the maximum pattern level. The intermediate points can be linearly interpolated and the threshold difference is empirically computed as

$$D_{\text{th}}^{(m+2)} = 20\log_{10}\left(\frac{1}{3}\left(1+\sqrt{\frac{0.5}{10^{\frac{\text{SNR}}{10}}}}\right)\right). \tag{6.5}$$

Afterwards, the threshold difference is compared with the computed difference as

$$D^{(m+2)} - D_{\text{th}}^{(m+2)} = \begin{cases} < 0 & \text{skip point} \\ \geq 0 & \text{include point} \end{cases} \tag{6.6}$$

[2]The SNR value is deduced empirically from practical measurements.

and the corresponding points from ring $(m + 1)$ are skipped according to the given condition. Fig. 6.4 shows the schematic of the designed algorithm[3]. The process is recursively repeated until the boundary of the scan plane is reached when it terminates. The given procedure is equally valid for square as well as rectangular grids. The only difference occurs in acquiring the initial data from the center which is in accordance with the shape of the grid.

6.2 Performance Evaluation

6.2.1 Case I: Planar

In order to assess the performance of the proposed procedure, synthetic as well as measured data is utilized. Electric dipoles are used to model the AUT with proper magnitude profile and geometrical arrangement as explained in [60]. A high gain parabolic reflector (64 λ) and a medium gain horn (4 λ) are designed with source dipoles arranged in concentric circles. The near-field distribution of both antennas collected in the *xz*-plane and placed at $y = -1.5\,\mathrm{m}$ with half-wavelength sample spacing is shown in Fig. 6.5. As observed, the near field of the high gain antenna varies smoothly but the medium gain horn contains fluctuations.

Afterwards, the proposed planar adaptive approach is applied considering 20 dB SNR at maximum amplitude in the decision threshold and is decreased down accordingly, as explained in section 6.1.4. The resulting near-field distribution is shown in Fig. 6.6. Apart from part of the main beam acquired in the beginning, it can be seen that every alternate near-field ring for the parabolic reflector is skipped making a full-wavelength sample spacing. Sudden changes in the horn near field distribution are successfully detected at run time, hence data is acquired accordingly.

For realistic comparisons, we also use measured data of a broad beam and a shaped beam antenna operating at 4 GHz and 12 GHz, respectively. The proposed procedure is applied to the measurement data and the adaptive near-field distribution is shown in Fig. 6.7. A significant reduction of data points can be seen in the field distribution of the broad beam antenna while less reduction of data points is observed for the shaped beam antenna.

To get more insight into the effect of changing the SNR in the decision criterion, the SNR is varied from 80 dB to 20 dB at the highest near-field amplitude. On decreasing the SNR the number of measurement points also decreased. However, less reduction of measurement points is observed for the shaped beam antenna due to abrupt changes in the near-field distribution.

Adaptive and regular near-field data of both synthetic and real antennas are processed using FI-AFTA. The transformed far field of all the AUTs is obtained by considering various SNR values in the decision threshold. The transformed pattern obtained using regular near-field data is compared with the transformed pattern using adaptive acquisition and the error level is computed as

$$\text{Error level} = 20\log_{10}(\text{abs}((|\boldsymbol{E}_{\text{reg}}(\theta,\phi)| - |\boldsymbol{E}_{\text{adap}}(\theta,\phi)|)). \tag{6.7}$$

Fig. 6.9 shows the transformed E-plane pattern cuts of the broad-beam antenna with lowest 20 dB SNR at maximum pattern level. As observed, good results have been obtained even with approx. 45 % decrease in the number of measurement points. To clearly show the effect of varying SNR in the decision threshold, the maximum error in the transformed E- and H-plane pattern cuts versus

[3]The schematic is shown for planar measurements. For cylindrical and spherical near-field acquisition a similar concept is applied.

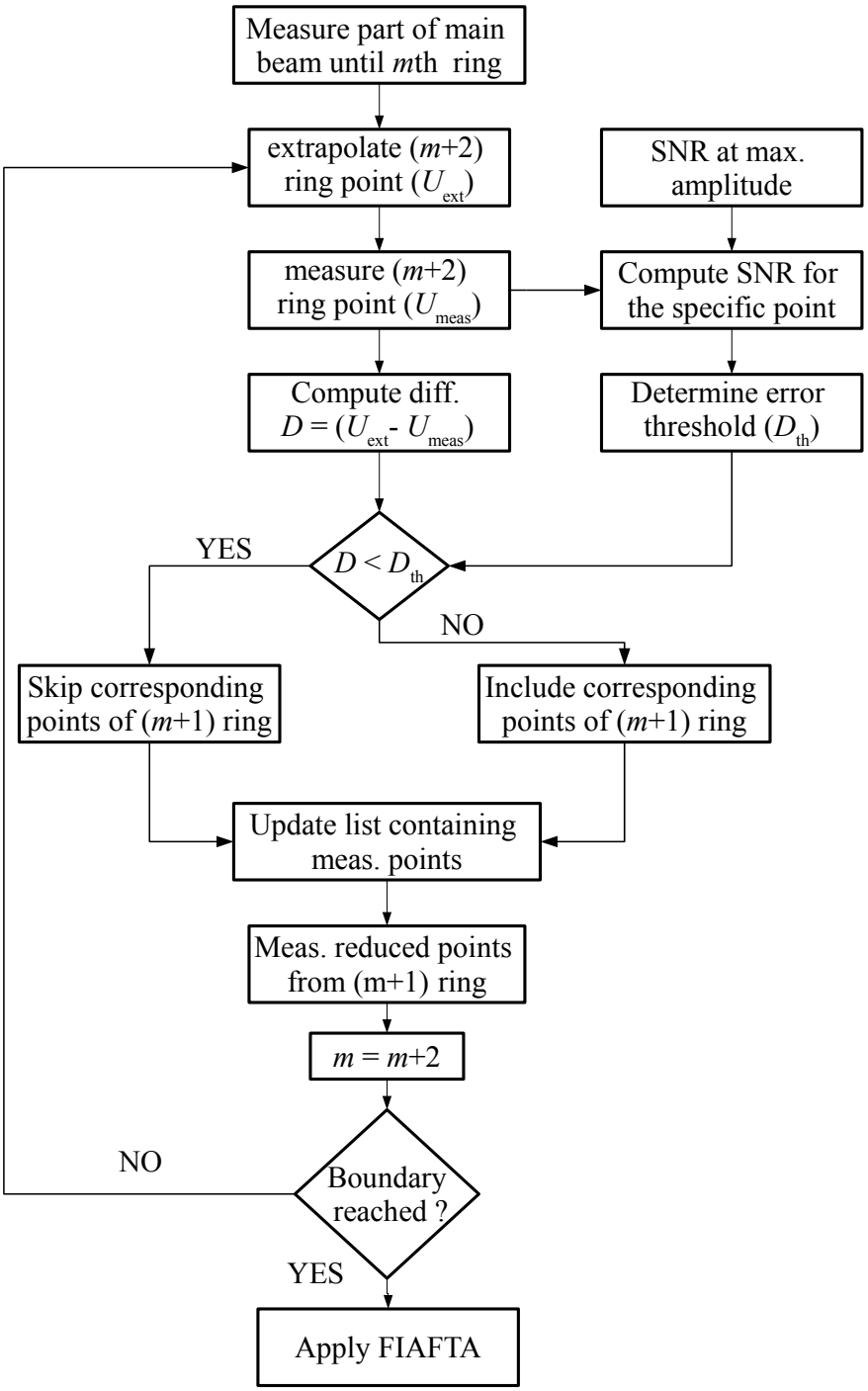

Figure 6.4: Schematic of the proposed adaptive acquisition techniques' procedure.

SNR at maximum pattern level is shown in Fig. 6.10. The percentage reduction in the number of measurement points is also shown on the right side of Fig. 6.10. As expected, the accuracy of the transformed pattern increases by increasing the SNR value which in turn also increases the num-

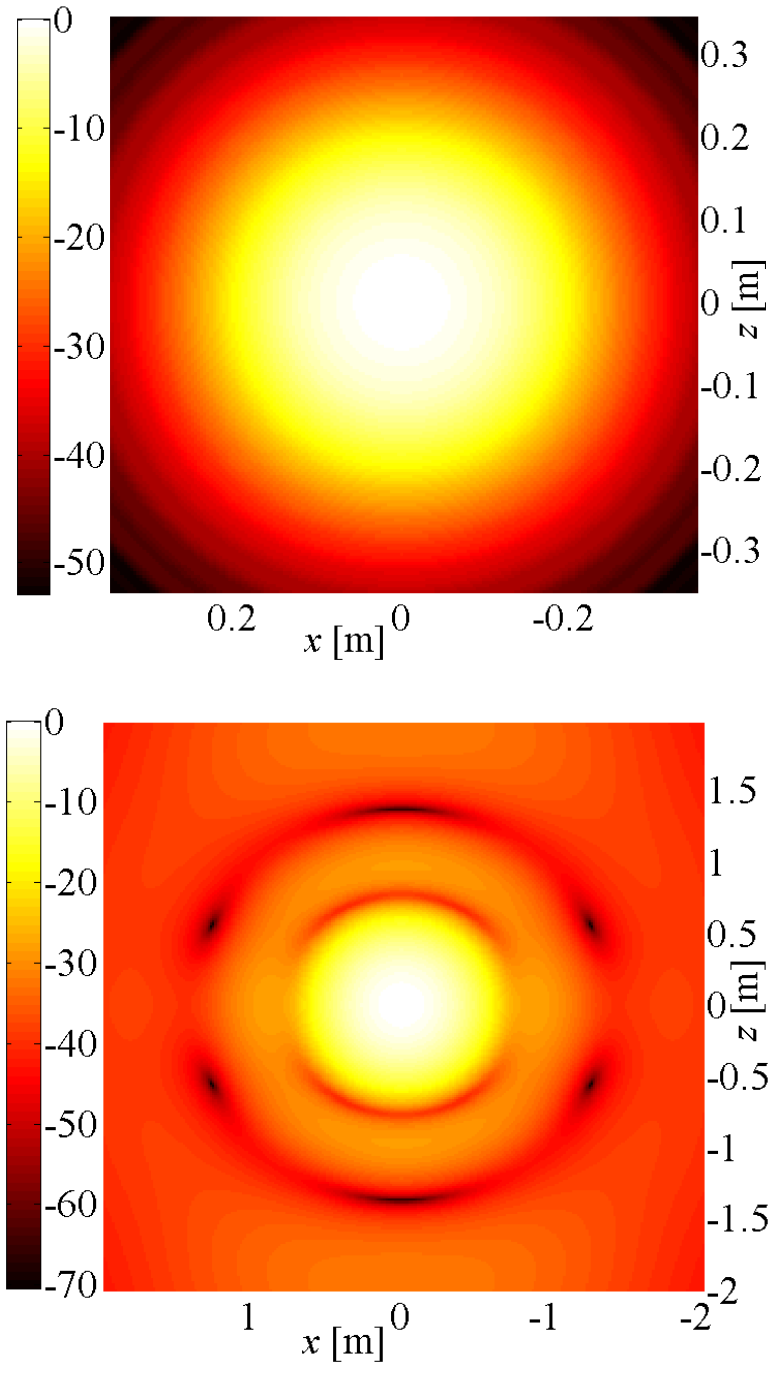

Figure 6.5: Near-field distribution of high gain parabolic reflector (a) and medium gain horn (b) operating at 40 GHz and 10 GHz, respectively.

ber of measurement points. A similar behavior is seen for all the antennas under test. The lowest accuracy at lowest SNR i.e. 20 dB is tabulated in Table 1 for both E- and H-plane pattern cuts. The SNR can be increased for higher accuracy at the expense of more measurement points.

In a traditional measurement setup, the near field is acquired by linear motion of the probe in

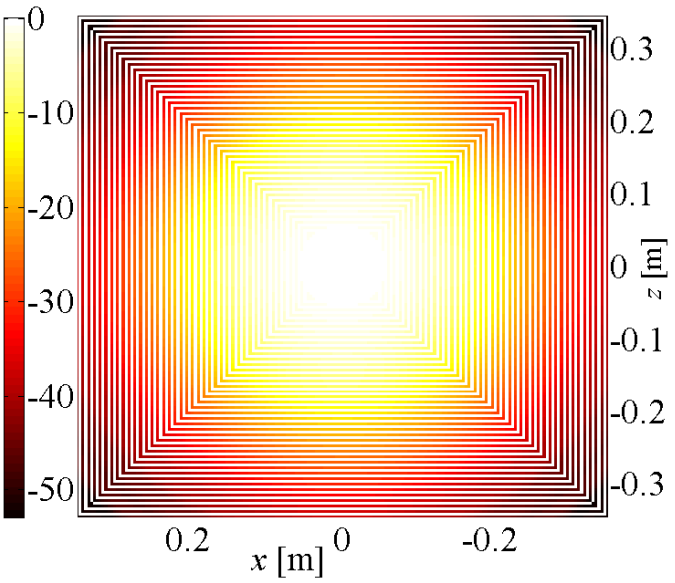

(a) Adaptive near-field acquisition of high gain parabolic reflector

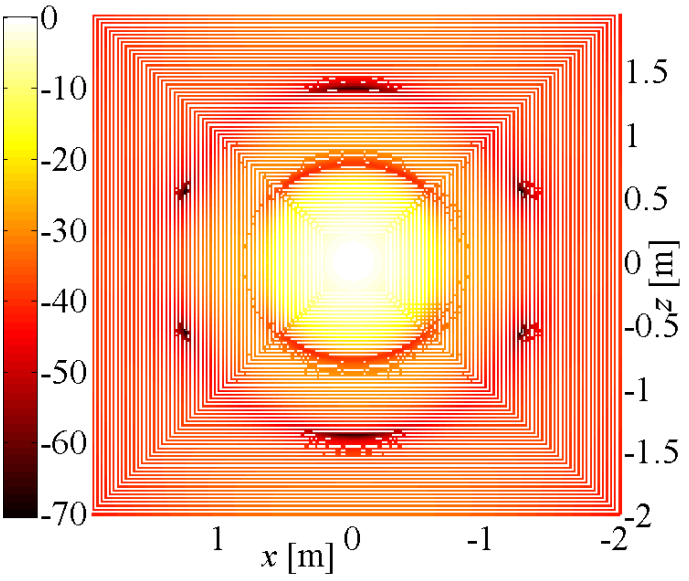

(b) Adaptive near-field acquisition of medium gain antenna

Figure 6.6: Adaptive near-field acquisition of high gain parabolic reflector (a) and medium gain horn (b). White rings denote the location of skipped data.

vertical direction while stepping in the horizontal, or vice versa. Assuming the same scan speed v of the probe in the vertical and the horizontal direction, the total acquisition time t_{tot} can be expressed as

$$t_{\mathrm{tot}} = \frac{L_t}{v} + N t_{\mathrm{mp}} + n t_{\mathrm{delay}} \tag{6.8}$$

where L_t is the total length traversed by the probe in the vertical and the horizontal direction, N is the total number of measurement points, t_{mp} is the acquisition time at one measurement point, n

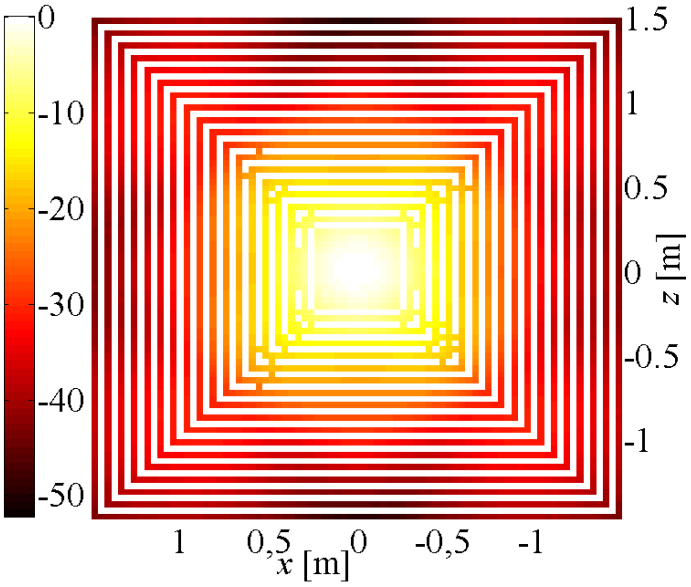

(a) Adaptive near field acquisition of the broad beam antenna

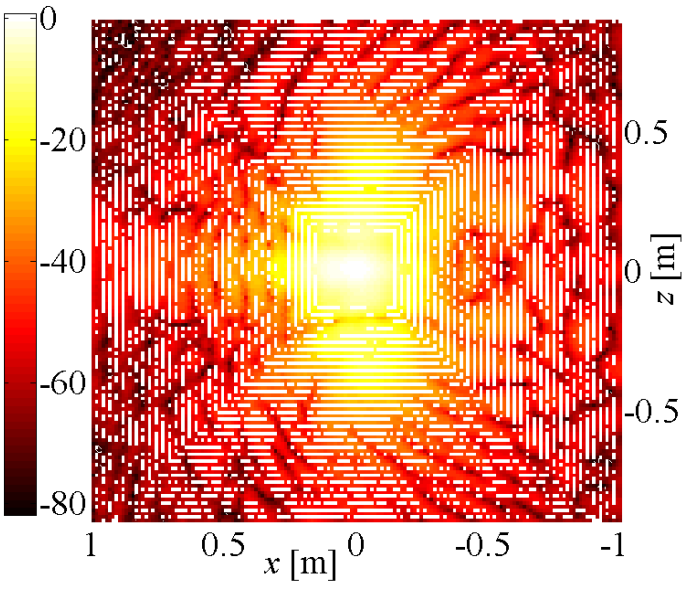

(b) Adaptive near field acquisition of the shaped beam antenna

Figure 6.7: Adaptive near field acquisition of the broad beam (a) and the shaped beam antenna (b). White rings denote the location of skipped data.

is the number of times when the probe changes its direction while stepping, and t_{delay} represents the delay due to a single change. The black spots in Fig. 6.11 mark the position of the probe when it changes its direction.

The ring shaped adaptive data acquisition can be achieved by traversing the probe in a rectangular spiral locus while starting from the center of the scan plane and stepping in the outward direction away from the center. The total acquisition time for the adaptive approach can also be ex-

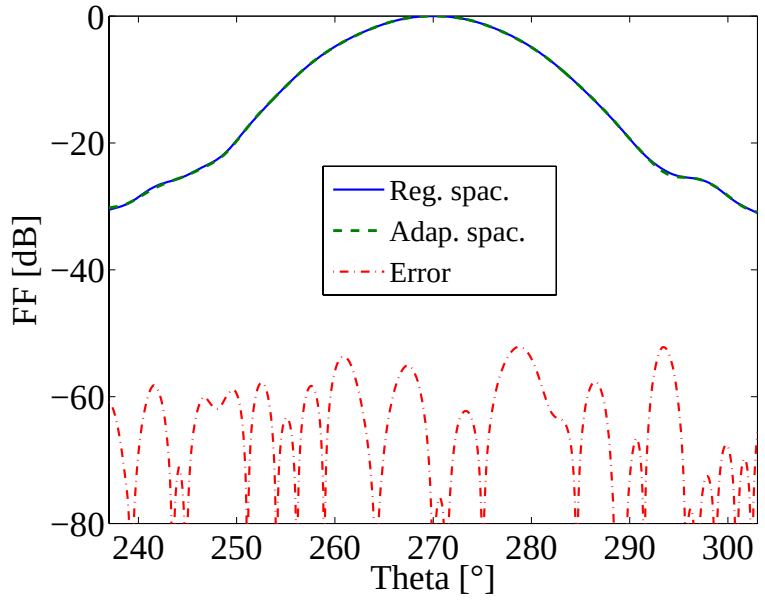

(a) E-plane pattern cut (main polarisation)

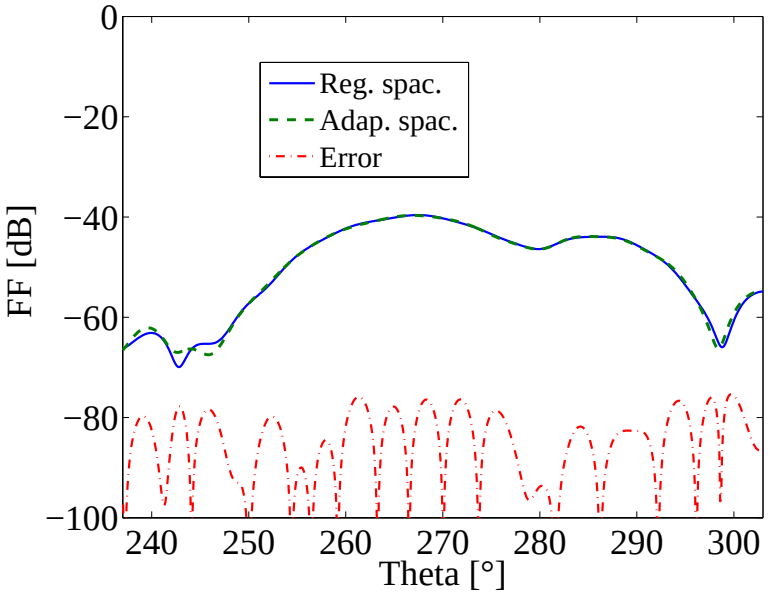

(b) E-plane pattern cut (orthogonal polarisation)

Figure 6.8: E-plane transformed far-field pattern cut for the main polarisation (a) and the orthogonal polarisation (b) using regular and adaptive processing of measured near-field data of the broad-beam antenna.

pressed using Eq. (6.8) but with varying L_t and N according to the given decision threshold. The state-of-the-art RF equipment allows data acquisition by moving the probe in an on-the-fly manner due to negligible processing time at one single point. Therefore, one can neglect the term $(N\mathrm{t}_{\mathrm{mp}})$ from Eq. (6.8) as it is considerably smaller than the other two factors. The length L traversed by the probe in the traditional measurement can be calculated as L_{trad} = (length of one vertical column)(no. of vertical columns), whereas for the adaptive measurements it can be calculated by measuring the length of the rings traversed during the measurement. Since all the rings have dif-

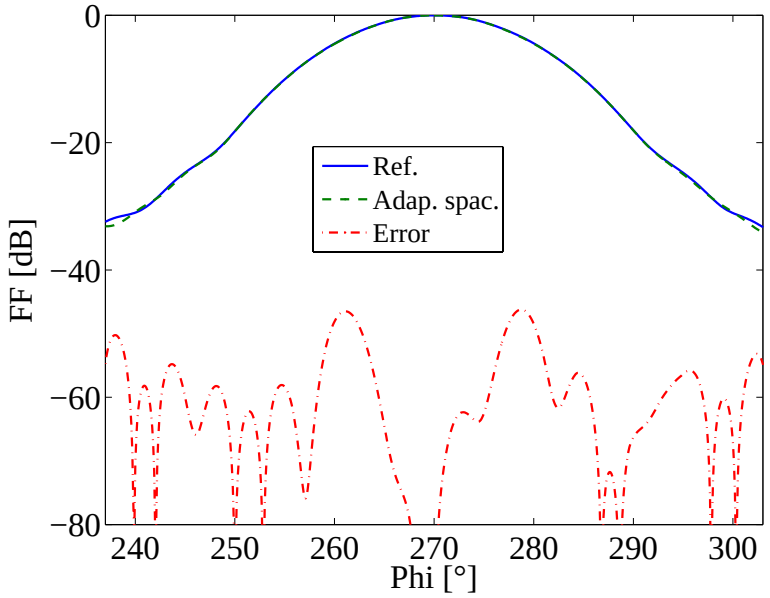

(a) H-plane pattern cut (main polarisation)

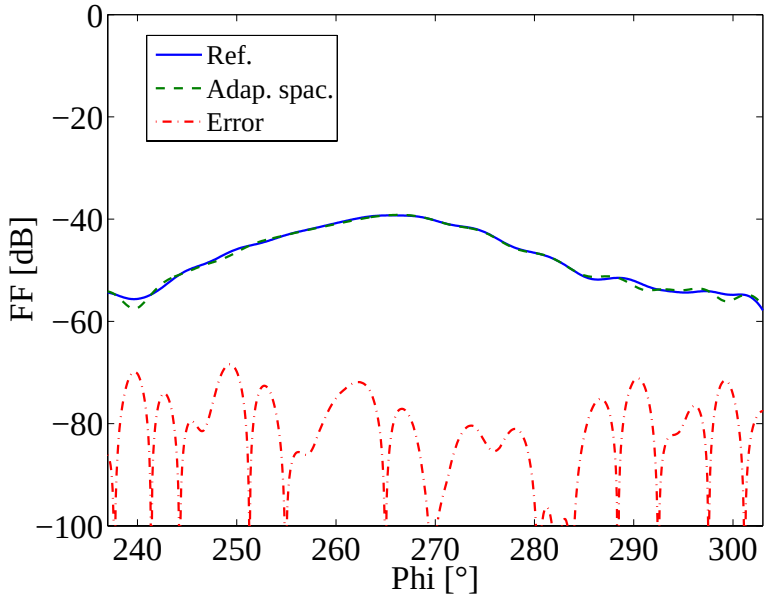

(b) H-plane pattern cut (orthogonal polarisation)

Figure 6.9: H-plane transformed far-field pattern cut for the main polarisation (a) and the orthogonal polarisation (b) using regular and adaptive processing of measured near-field data of the broad-beam antenna.

ferent lengths, the right knowledge of the skipped ring must be known for the correct length L_{adap}. It is worth mentioning here that even if a measurement is required at few points in one ring only, it is assumed that the whole ring is measured for computing the measurement time.

Table 6.2 summarizes the length traversed by the probe during traditional and adaptive measurements considering 20 dB SNR at maximum pattern level. Due to simplicity, we assume that the delay arising from changing the probe direction is the same for both cases, as can be seen from

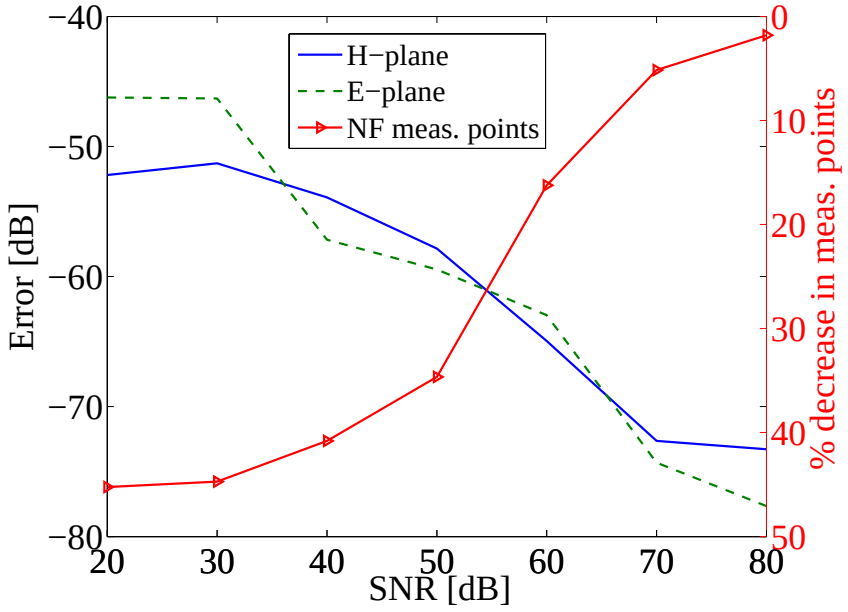

Figure 6.10: SNR at maximum pattern level versus maximum error level in the transformed E- and H-plane pattern cuts of the broad beam antenna (left y-axis) along with the reduction in the number of measurement points (right y-axis).

Table 6.1: Maximum error levels in the valid region of transformed E- and H-plane pattern cuts with adaptive acquisition of near-field data assuming 20 dB SNR at maximum pattern level.

AUT	Maximum Error Level [dB]			
	E-plane		H-plane	
	Main-pol.	Orth.-pol.	Main-pol.	Orth.-pol.
Medium gain	-67.30	-98.99	-64.77	-105.40
High gain	-68.18	-131.70	-67.17	-93.76
Broad-beam	-52.15	-75.36	-46.23	-68.42
Shaped-beam	-48.54	-65.80	-44.50	-58.80

Fig. 6.11. However, less delay is expected in adaptive measurements if many measurement rings are skipped.

The efficiency in the measurement time is also shown in Table 6.2. As observed, best results have been achieved for the high gain antenna with smoothly varying near field distribution while the worst case with zero efficiency is seen for the shaped beam antenna. The probe has to traverse the whole scan plane for the shaped beam antenna as not a single ring can be skipped according to the given decision function. Nevertheless, no extra time is needed as compared to the traditional technique and since the whole scan plane is traversed one can utilize the whole near field information for the maximum accuracy.

The sample spacing in the planar near-field acquisition can be further increased by using the adaptive approach [11]. If the number of skipped points in the $(m+1)$ ring are greater than a defined threshold, then in the next iteration two consecutive rings i.e. $(m+3)$ and $(m+4)$ can

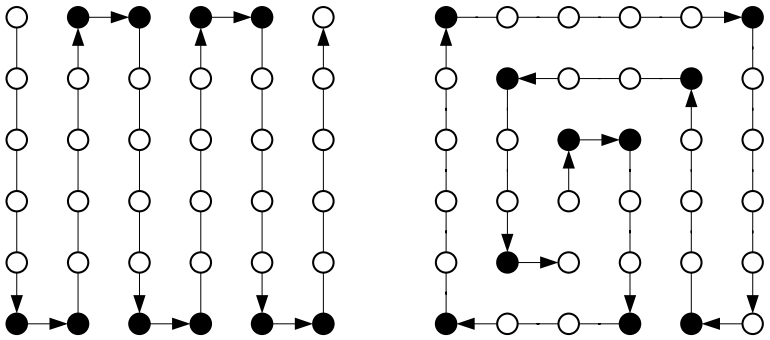

Figure 6.11: Traditional versus adaptive scanning technique (worst case). Black spots mark the position where the probe has to stop and change direction, thus causing an additional delay.

Table 6.2: Comparison between traditional and adaptive measurement in terms of number of measurement points and length L traversed by the probe assuming 20 dB SNR at maximum pattern level.

AUT	Meas. Points		Length L_t [m]		Meas. Time Efficiency
	Tradi.	Adap.	Tradi.	Adap.	
Medium gain	70756	36847	1068	655.45	38.63 %
High gain	34969	18329	131.6	69.94	46.85 %
Broad-beam	6889	3772	251	154.88	38.29 %
Shaped-beam	23345	16596	290	290	0.00 %

be skipped and so on, which is in contrast to the previous case where alternate measurement rings were skipped. Therefore, a huge decrease in the number of data points is possible. This process continues until the boundary of the scan plane is reached. Fig. 6.12 shows a measurement plane divided into a rectangular ring structure with adaptive acquisition.

The adaptive near-field distribution of a medium gain antenna is shown in Fig. 6.13. It can be seen that the abrupt changes in the near field are determined successfully and the adaptive sample spacing increased from $\lambda/2$ to 2λ where it stays constant. A regular (4 m $\times$ 4 m) grid with $\lambda/2$ sample spacing at 10 GHz requires 70 756 data points. The number of measurement points have been reduced to only 20 722 marking 70.7% reduction in the number of measurement points. The previously reported reduction in the sampling points by skipping alternate rings was 47.9%. The transformed pattern cuts are shown in Fig. 6.14 clearly showing negligible change in the pattern.

6.2.2 Case II: Cylindrical

The assessment of adaptive cylindrical sampling is performed by designing an elongated antenna (15λ) operating at 3 GHz using electric dipoles. The near field is collected with the antenna looking in $-y$ direction. The height and the radius of the measurement cylinder are 4 m and 1.5 m,

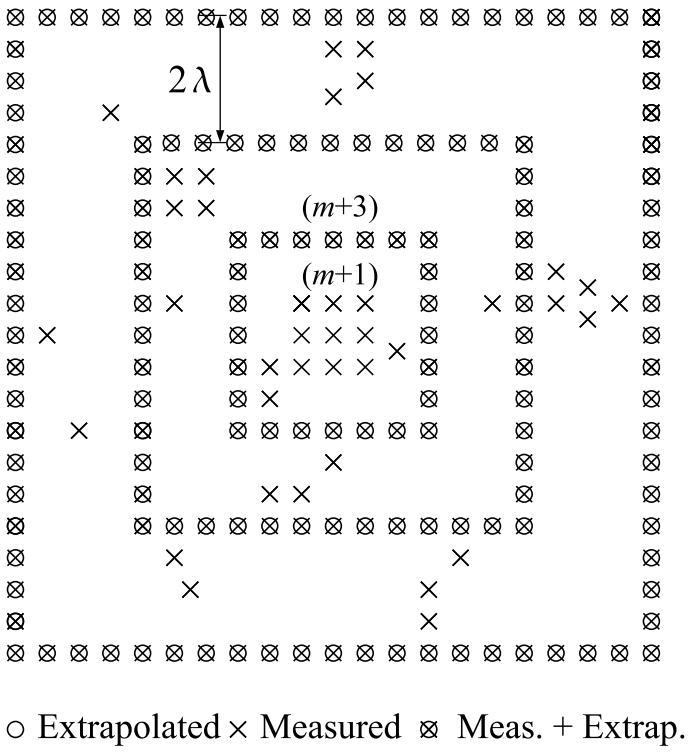

Figure 6.12: Measurement plane dividing sampling points into rectangular rings skipped adaptively.

respectively. Fig. 6.15 and Fig. 6.16 show the traditional and the adaptive acquisition of the near field of the elongated antenna, respectively. The SNR at the maximum pattern level is 30 dB and is decreased down to lower values at lower pattern level, as explained earlier. It is evident from Fig. 6.16 that almost every alternate column of the cylinder can be skipped for the elongated antenna. The number of measurement points is reduced from 9 801 to 5 117 marking 48% decrease in the number of measurement points. Since almost every alternate column is skipped, the measurement time is also reduced to nearly 48%.

Transformed E- and H-plane cuts of the elongated antenna considering 30 dB SNR at maximum pattern level are shown in Fig. 6.17 for cylindrical measurements. Further increase in the accuracy can be obtained by increasing the SNR at maximum pattern level as evident from the valid angle region (non-shaded) in Fig. 6.18.

6.2.3 Case III: Spherical

For the spherical case, the near field of a fan beam antenna i.e. a Kathrein base station antenna of type 742445 $(8.3\lambda \times 1.3\lambda)$ operating at 1.92 GHz using an NSI near-field scanner is used. The adaptively acquired near-field distribution with strong variations on the spherical grid for the fan beam antenna is shown in Fig. 6.19. The strong variations in the near field have been detected successfully at the cost of less data reduction. Fig. 6.20 and 6.21 show the transformed E- and H-plane pattern cut of the fan beam antenna. As can be seen, good accuracy is achieved with much reduction in the number of measurement points.

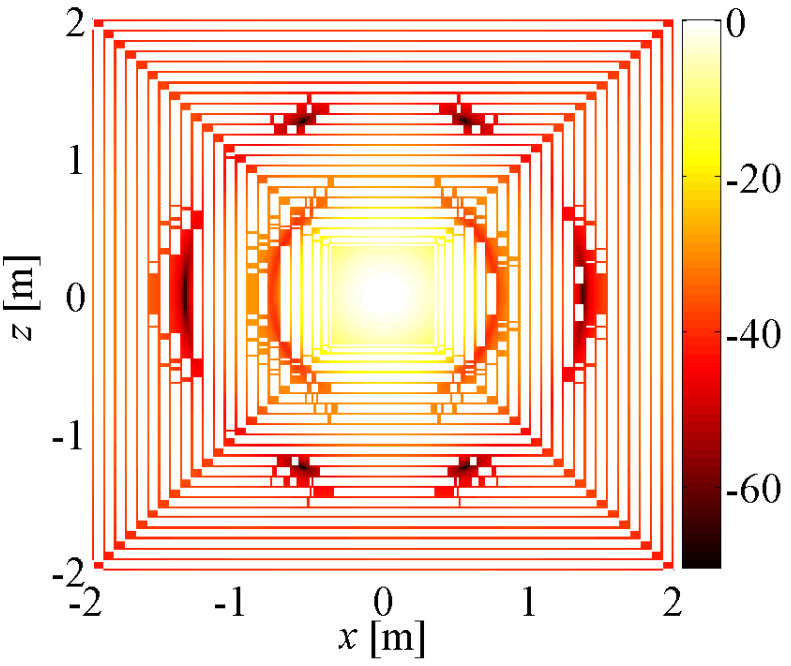

Figure 6.13: Near-field distribution of horn like antenna [dB] using adaptive sampling grid. White rings show the position of skipped measurements points.

It must be mentioned here that the explained near-field acquisition techniques are empirically derived and as such cannot assure a certain accuracy. The SNR value used to define the decision threshold is directly related with the number of sampling points to be acquired during the near field scanning and therefore also controls the transformed far-field accuracy. Nevertheless, the proposed technique can be applied to the cases when a rough estimation of radiation pattern is required using minimum acquired near-field samples.

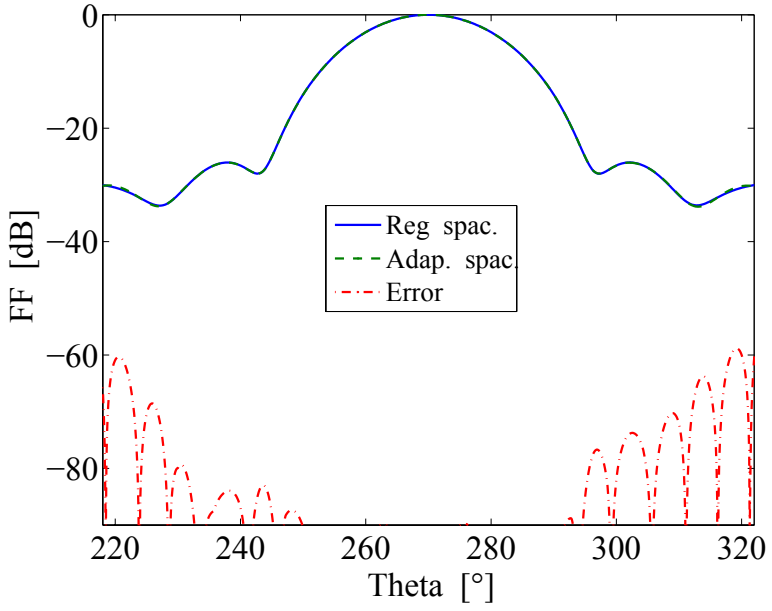

(a) E-plane pattern cut

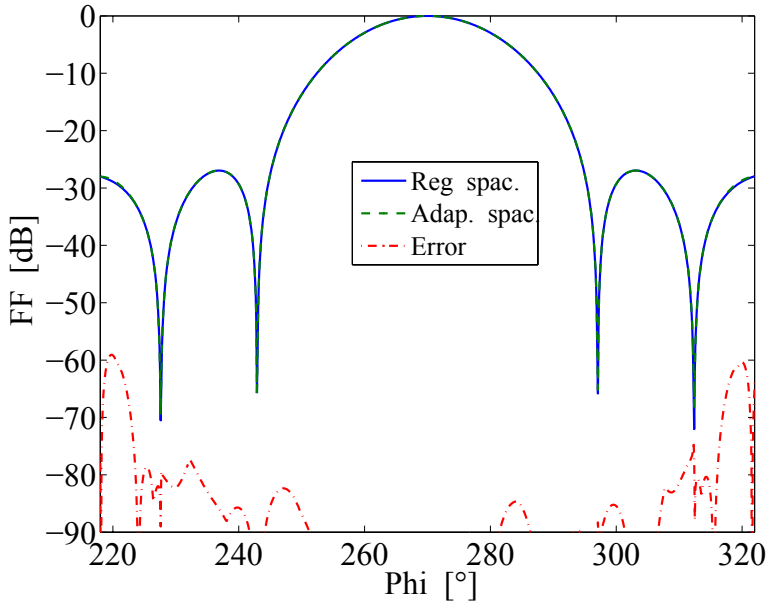

(b) H-plane pattern cut

Figure 6.14: Transformed E- and H-plane pattern cuts for the medium gain antenna considering 30 dB SNR at maximum pattern level.

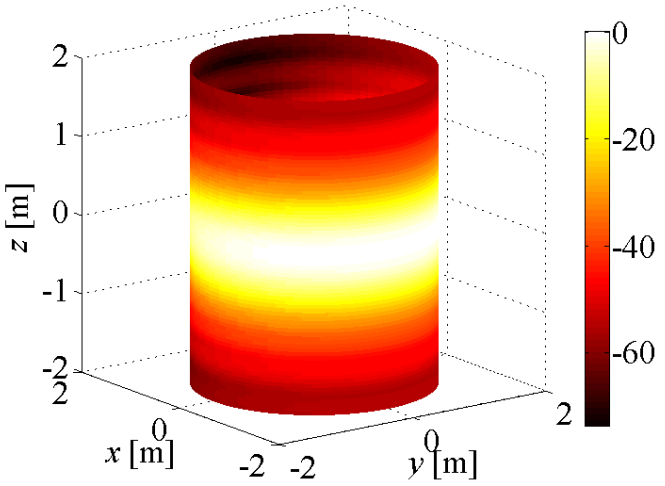

Figure 6.15: Cylindrical near-field distribution [dB] of elongated antenna at 3 GHz.

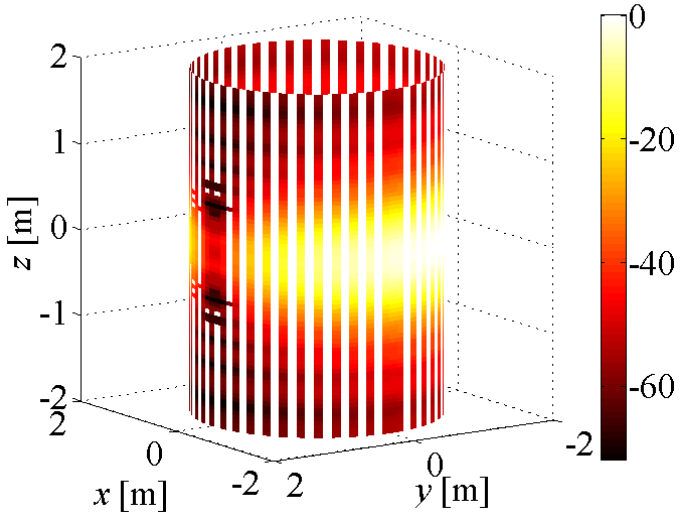

Figure 6.16: Adaptive cylindrical near-field acquisition [dB] of elongated antenna (3 GHz) considering 30 dB SNR at maximum pattern level (white spaces show the location of skipped near-field data).

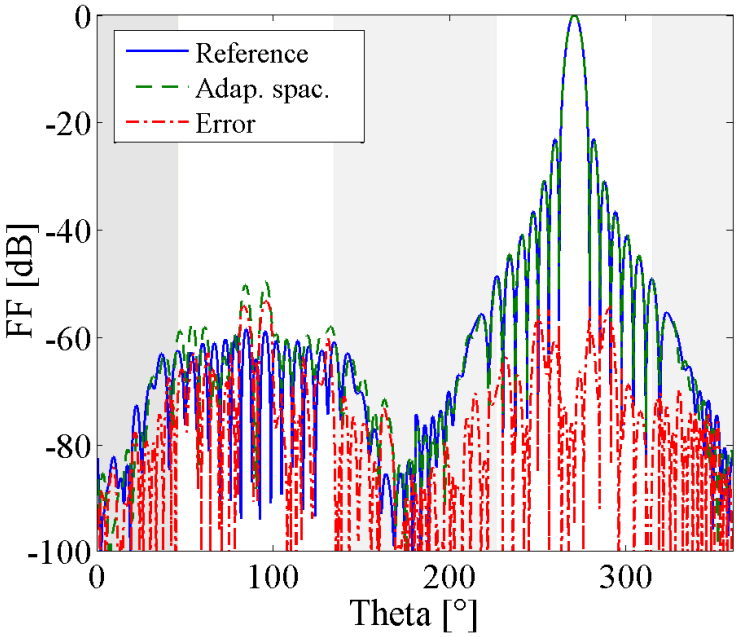

(a) E-plane pattern cut

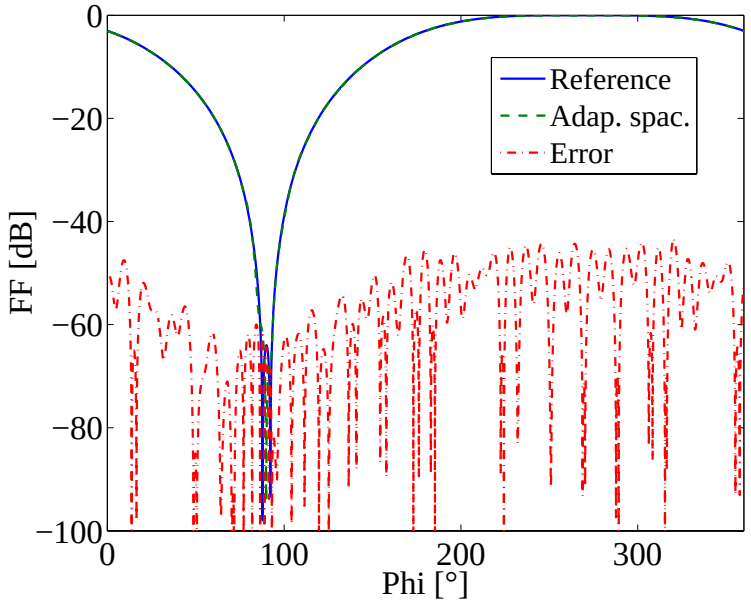

(b) H-plane pattern cut

Figure 6.17: Transformed E- and H-plane pattern cuts for the elongated antenna considering 30 dB SNR at maximum pattern level.

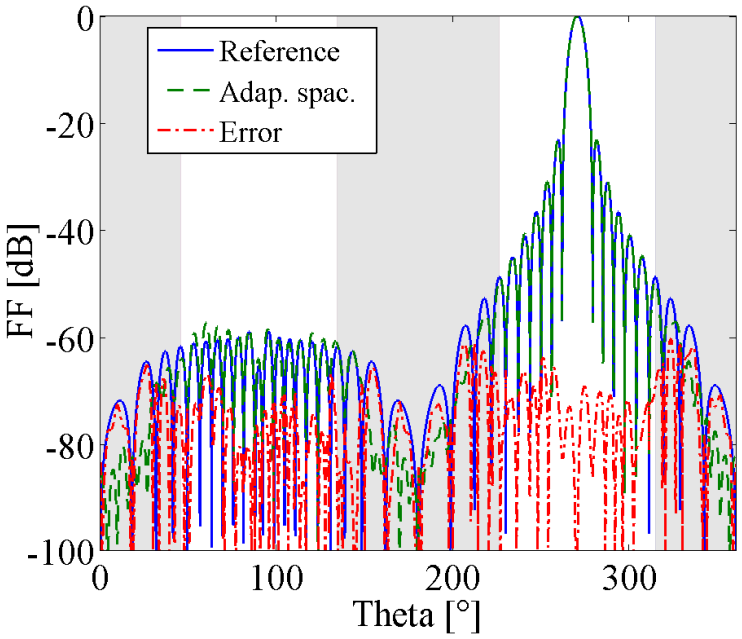

(a) E-plane pattern cut

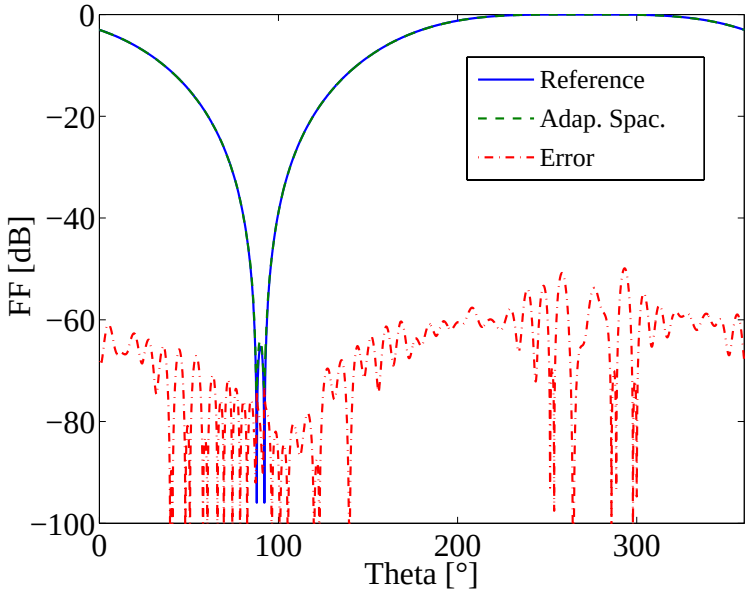

(b) H-plane pattern cut

Figure 6.18: Transformed E- and H-plane pattern cuts for the elongated antenna considering 65 dB SNR at maximum pattern level.

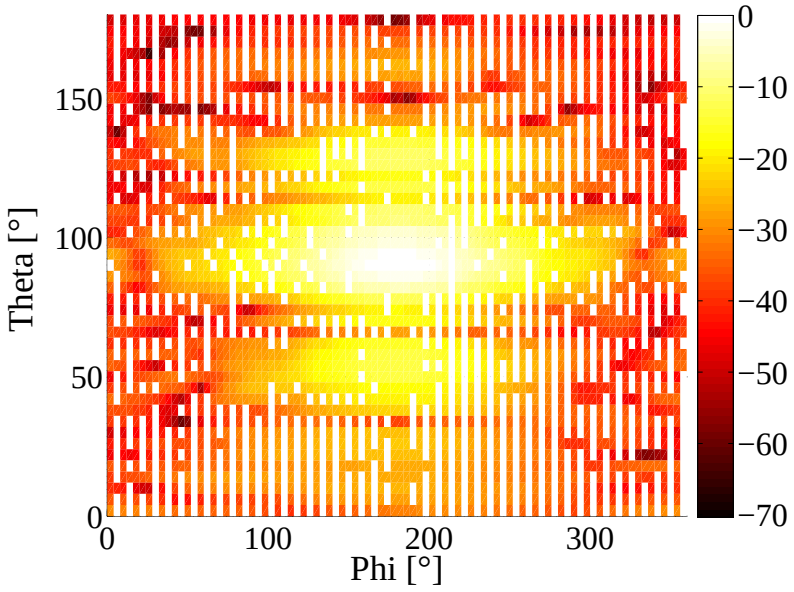

Figure 6.19: Adaptive spherical near-field acquisition [dB] considering 50 dB SNR at maximum pattern level for fan beam antenna at 1.92 GHz (white spaces show the location of skipped near-field data).

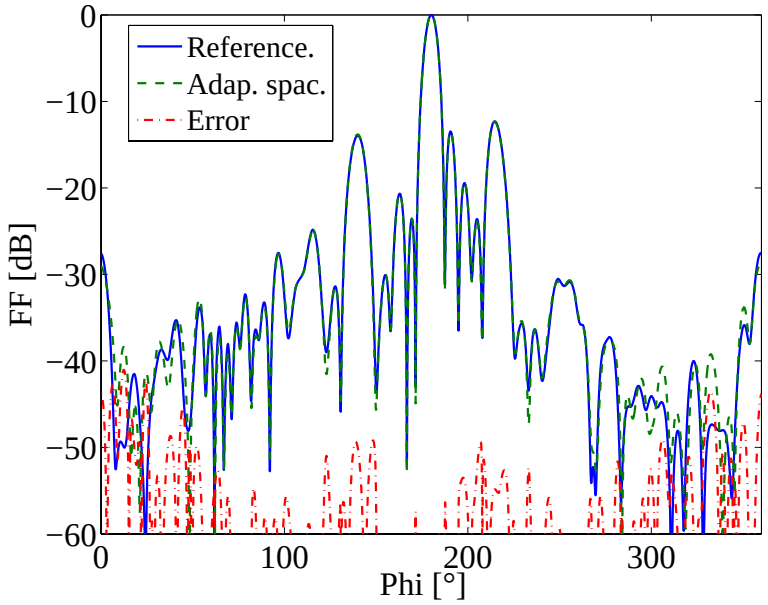

(a) E-plane pattern cut

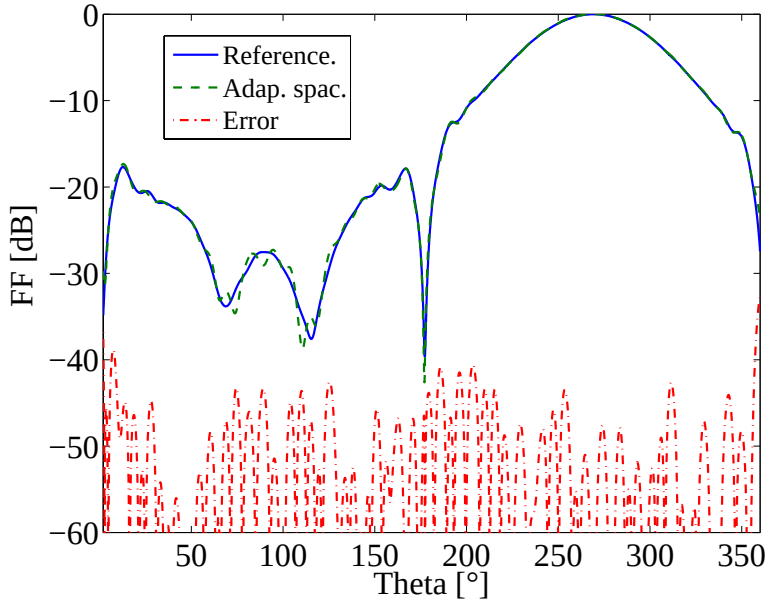

(b) H-plane pattern cut

Figure 6.20: Transformed E- and H-plane main polarisation pattern cuts of fan beam antenna considering 50 dB SNR at maximum pattern level.

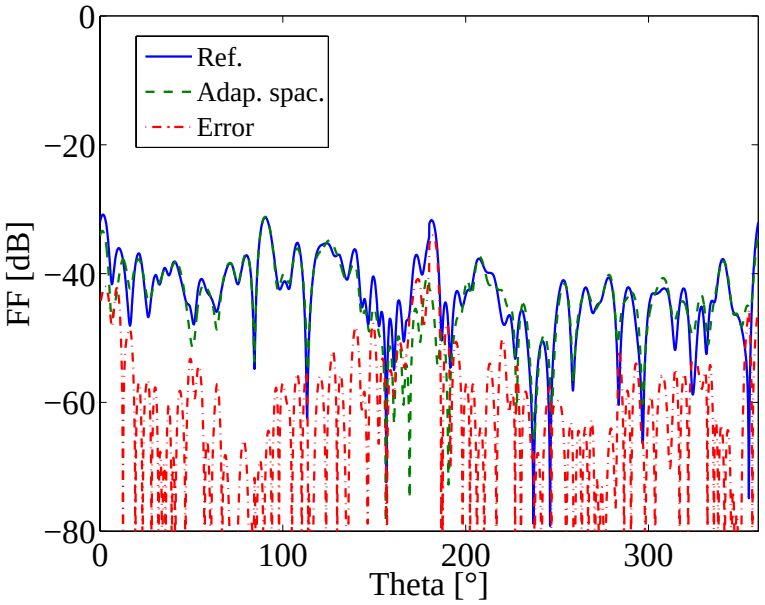

(a) E-plane pattern cut

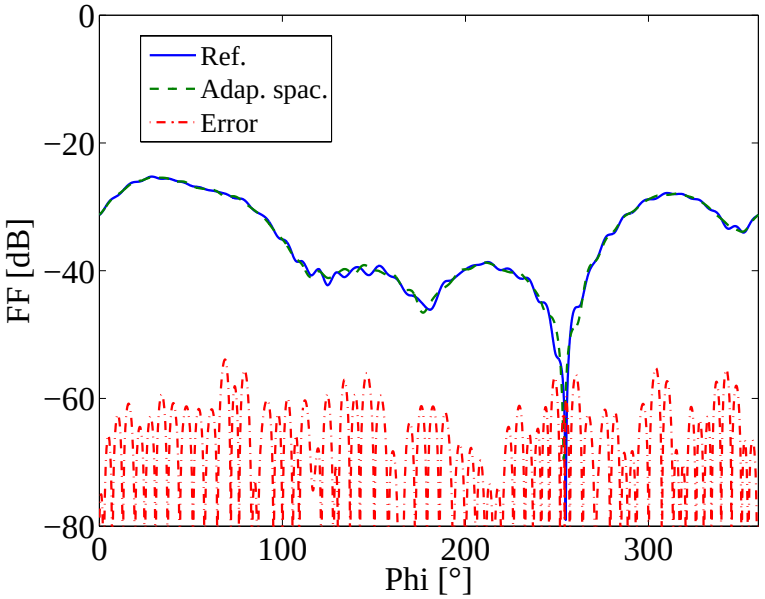

(b) H-plane pattern cut

Figure 6.21: Transformed E- and H-plane orthogonal polarisation pattern cuts of fan beam antenna considering 50 dB SNR at maximum pattern level.

Chapter 7

Nonredundant Sampling Representation for Arbitrary Measurement Grids

As stated in the Chap. 6, the adaptive near-field acquisition technique is empirically derived and cannot assure maximum accuracy. Therefore, the exact sampling criterion still needs to be determined. Since FIAFTA can handle measurements on arbitrary grids, the data point distribution on the arbitrary scanning surfaces should be determined. In this chapter, these basic concerns are addressed and the sample spacing criterion is derived in relation with the number of unknown plane wave coefficients. Before moving forward, the summary of the literature already available on the nonredundant sampling for the arbitrary measurements grids is described.

A valuable contribution regarding nonredundant sampling representation on arbitrary surfaces with theoretical analysis has been performed by Bucci et al. in [96]. It has been shown that the electromagnetic (EM) field radiated by bounded sources can be accurately represented over arbitrary surfaces with a finite number of samples even with unbounded observation domain. The approach makes use of spatially band-limited functions to approximate the EM field provided the phase propagation factor is extracted from the field expression and proper parametrization is used to analytically define the surface [97]. It is also observed in [97] that the number of samples required for a given analytical surface is of the same order as needed for the spherical wave expansion. The given results have been utilized in various contributions, e.g. [92], [98], [99], [73], and many others outline the reduction in the number of required near-field samples as compared to classical transformation techniques. The key factor involved in the utilization of nonredundant sampling for evaluation of the far field is the use of optimal sampling interpolation (OSI) to determine the intermediate samples. The near-field distribution can then be used by fast transformation algorithms. A recently proposed direct transformation [100] utilizes the acquired nonredundant near-field data directly for cylindrical geometries. A far-field OSI expansion is proposed from an efficiency point of view. The described far-field OSI expansion reconstructs the antenna pattern from a limited number of far-field samples and is only suitable for cylindrical surfaces [101].

7.1 Nonredundant Sampling Representation

To reconstruct the radiation pattern of the AUT using equivalent plane wave sources, an efficient sampling representation must be defined. Obviously one cannot use an infinite number of samples so a certain sample spacing criterion providing sufficient accuracy in the reconstructed pattern is

desirable. In this section, a nonredundant sampling representation is determined which is equally valid for arbitrary surfaces. As explained in Chap. 3, the spectral integral over the Ewald sphere is evaluated by numerical quadrature with discrete representation using (3.4). A linear system of equations can then be developed for many measurement points as

$$\boldsymbol{U}' = -\mathrm{j}\frac{\omega\mu}{4\pi}\,\|C\|\cdot\tilde{\boldsymbol{J}}', \tag{7.1}$$

where $\boldsymbol{U}'$ is the measured voltage vector containing all measurement points with both orthogonal polarizations and $\tilde{\boldsymbol{J}}'$ contains the plane wave samples of the AUT. The diagonal translation operator $T_L(\hat{k},\hat{r}_{\mathrm{M}})$, weighting factor $W(k_\theta)$, and probe correction coefficient $\tilde{\boldsymbol{P}}(\hat{k},\hat{r}_{\mathrm{M}})$ are combined to form the coupling matrix $\|C\|$. It is worth mentioning here that in the multilevel approach, the coupling matrix $\|C\|$ is no more explicitly computed. The set of plane waves $\tilde{\boldsymbol{J}}'$ (forward operator) is used to compute $\boldsymbol{U}'$ in an on-the-fly manner. The normal system of equations is solved in the solution stage of the GMRES solver. Therefore, the adjoint operator is applied to the result of the forward operator. The adjoint operator starts from the probe signal at a measurement point and superimposes the contributions of each measurement point to the overall spectrum of the AUT using aggregation and interpolation as adjoint operations to disaggregation and anterpolation in the forward operator.

The number of unknowns i.e. plane wave coefficients in ϕ and θ direction are directly influenced by the size of the antenna given by the AUT multipole order L_{AUT} according to

$$P = 2\alpha_1 L_{\mathrm{AUT}}, \quad Q = \alpha_2 L_{\mathrm{AUT}} \tag{7.2}$$

where

- P = no. of plane wave coefficients (ϕ-direction),
- Q = no. of plane wave coefficients (θ-direction),
- α_1 = proportionality constant relating P and L_{AUT},
- α_2 = proportionality constant relating Q and L_{AUT}.

The number of plane wave coefficients in ϕ are twice the number of coefficients in θ to represent the equivalent plane wave sources on the complete sphere. The AUT multipole order is commonly approximated as

$$L_{\mathrm{AUT}} = kd/2 + 10 \tag{7.3}$$

with d as the diameter of the minimum sphere enclosing the AUT [25]. The number of samples used to solve the given system of equations should ideally at least equal the number of unknowns. Accordingly, the number of samples[1] in ϕ and θ is

$$M = \chi_1 P = 2\chi_1\alpha_1 L_{\mathrm{AUT}} \tag{7.4}$$

$$N = \chi_2 Q = \chi_2\alpha_2 L_{\mathrm{AUT}} + 1 \tag{7.5}$$

where

- M = no. of near-field samples (ϕ-direction),

[1] It should be mentioned that the total number of measurement points is $2MN$ where 2 represents two orthogonal polarizations for each measurement point. The same applies for the total number of unknowns.

- N = no. of near-field samples (θ-direction),[2]
- χ_1 = scaling factor for P,
- χ_2 = scaling factor for Q.

We choose $\chi_1 = \chi_2 = 1$ to fulfill the minimum requirement for the number of unknowns. For practical measurements, N samples in θ are taken in the $0 \leq \theta \leq \pi$ interval while M samples over the complete 2π interval i.e. $0 \leq \phi < 2\pi$ are used. Consequently, the uniform sample spacing in ϕ and θ using (7.4) and (7.5), respectively, is given as

$$\triangle\phi = 2\pi/M \quad \Rightarrow \triangle\phi = \pi/(\alpha_1 L_{\mathrm{AUT}}) \tag{7.6}$$

$$\triangle\theta = \pi/(N-1) \quad \Rightarrow, \triangle\theta = \pi/(\alpha_2 L_{\mathrm{AUT}}). \tag{7.7}$$

The empirical values of the proportionality constants α_1 and α_2 vary from 1 to slightly higher values depending on the noise conditions of the given measurement environment. It is worth noticing here that the number of samples required is of the same order as determined in [96] by considering equivalent sources on a minimum sphere. Since the plane wave based near-field transformation is equally valid for any scanning geometry, we can utilize the sampling representation on the sphere based on the derived sampling criterion and project the data points to any arbitrary surface. It should be mentioned that the given sampling criterion is derived by considering the equivalent sources on the minimum sphere enclosing the AUT. Further decrease in the number of samples may be still possible if volumetric redundancy of the convex domain enclosing the sources is also considered [96]. The least number of samples can be obtained if an arbitrary convex domain with some rotational symmetry according to the shape of the AUT is used along with the measurement surface with the same symmetry [90]. It is also worth mentioning that the equidistant angular spacing in θ and ϕ produces closely spaced samples at the poles and relatively larger sample spacing on the equator. An alternative sampling strategy for thinning the number of closely spaced samples at the poles could also be used, as described in [25]. Other uniform distributions may include equal area based partitions on the spherical surface [102]. We employ the equidistant angular spacing, but the equator region is utilized to map the samples from spherical to arbitrary surfaces for rigorous analysis. In the following, the mapping of these sampling points over planar, cylindrical, and an arbitrary surface is described with reference to the valid angle requirements.

The boundaries of the scan plane in the PNF measurement are defined by selecting a valid angle for the reliable region of interest. The simple relation (Eq. 4.9) containing separation between the AUT and the measurement plane d_{p}, radius of minimum sphere enclosing AUT a, and the length of the square shaped scan surface L has been already validated using theoretical and measurement results [61]. Similarly, area truncation can be carried out on a spherical surface with the corresponding valid region given as [25]

$$\theta_{\mathrm{vs}} = \theta_{\mathrm{t}} - \sin^{-1}\left(\frac{a}{d_{\mathrm{s}}}\right), \tag{7.8}$$

where θ_{t} is the angle until which the near field shall be sampled[3] and d_{s} is the radius of the spherical surface as shown in Fig. 7.1 (a). Combining and rearranging (4.4) and (7.8) gives the length of the planar scan plane

$$L = 2d_{\mathrm{p}} \tan\left(\theta_{\mathrm{t}} - \sin^{-1}\left(\frac{a}{d_{\mathrm{s}}}\right)\right) + a \tag{7.9}$$

[2]To include samples at the poles, a constant value "1" is added in the number of points in θ-direction

[3]The extent of sampling in ϕ can be computed in the same way. We assume the same valid angle for ϕ as it is assumed for θ.

for acquiring the near field in the region of interest. The samples obtained by dividing θ_t by $\triangle\theta$ are mapped to the planar surface as shown in Fig. 7.1 (b).

Unlike the traditional technique employing 2D FFT for planar measurements, the sample spac-

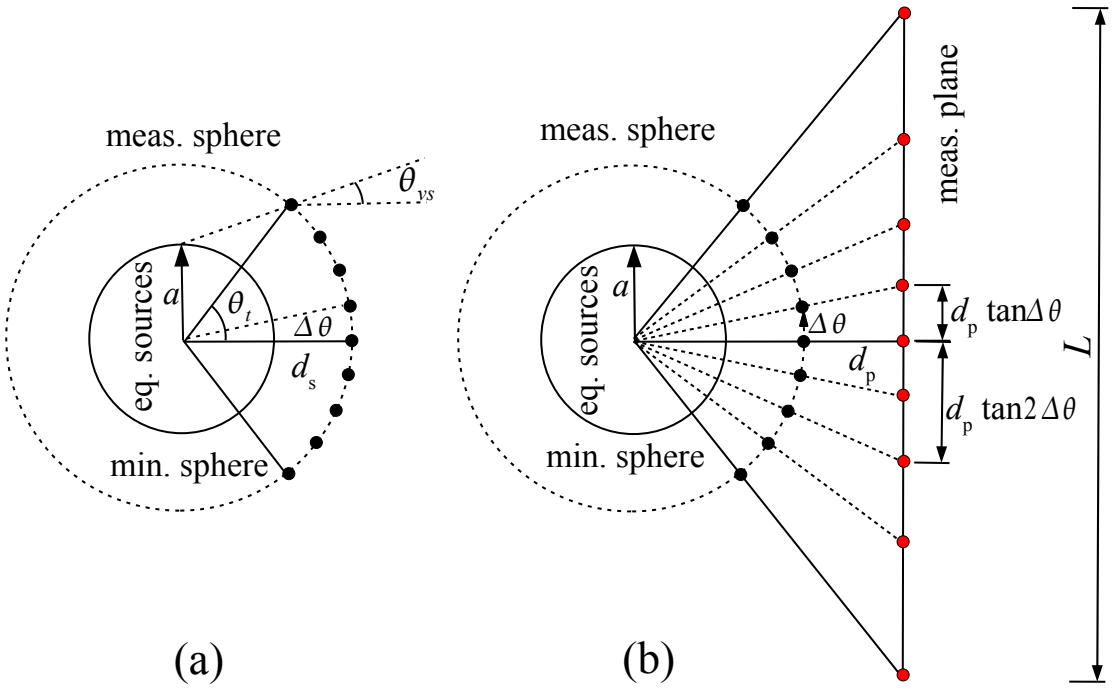

Figure 7.1: Region of validity for spherical truncation (a) and mapping of sample points from spherical to planar surface (b).

ing increases gradually as the probe moves in the outward direction from the center. Also, the $\lambda/2$ spacing as utilized in the classical approach is independent from the size and the separation between the AUT and the measurement plane which increases the measurement burden greatly for large antennas. The measurement grid obtained as a result of efficient sampling is shown in Fig. 7.2.

In a similar fashion, the number of measurement points can be dramatically reduced as compared to the traditional technique by projecting the samples over a cylindrical scanning surface [12]. The separation between each ϕ ring is increased gradually from the center as shown in Fig. 7.3. The height of the cylinder is calculated according to the valid region of interest while the angular spacing between samples in each ϕ ring remains the same.

The spacing between two consecutive samples in irregular grids is computed separately due to varying distance between the AUT and the measurement surface. The trigonometric relations

$$a_{23} = \sqrt{d_2^2 + d_3^2 - 2d_2 d_3 \cos(\triangle\theta)} \tag{7.10}$$

$$a_{12} = \sqrt{d_1^2 + d_2^2 - 2d_1 d_2 \cos(\triangle\phi)} \tag{7.11}$$

are used for this purpose where d_p with $p = 1, 2, 3, 4$ are the variable separations of the irregular surface S from the AUT (see Fig. 7.4). In this way, one can either compute the projected distribution of angular spacing over any arbitrary irregular surface or verify the minimum sampling requirement if the measurement grid is already available.

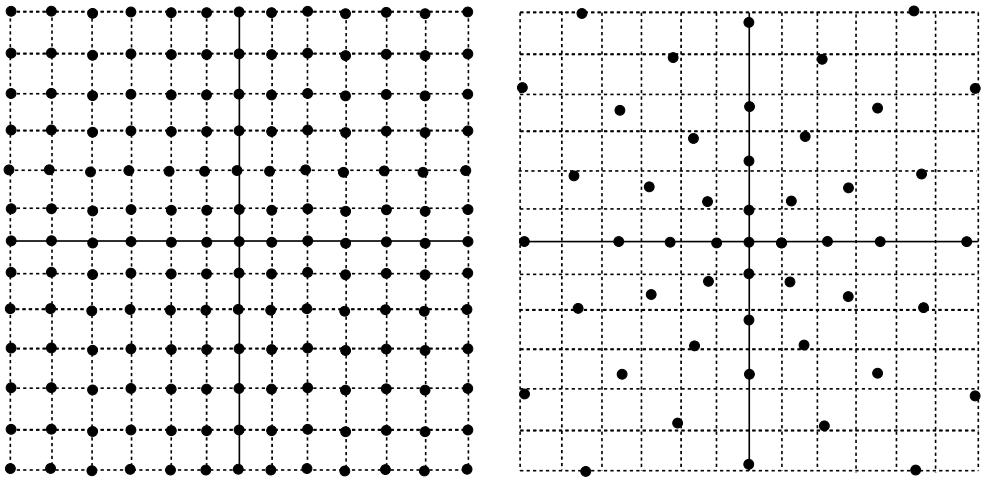

Figure 7.2: Traditional vs. projected nonredundant sampling on a planar grid. The sampling points shown on the nonredundant sampling grid are only for representation purposes and are not to the scale.

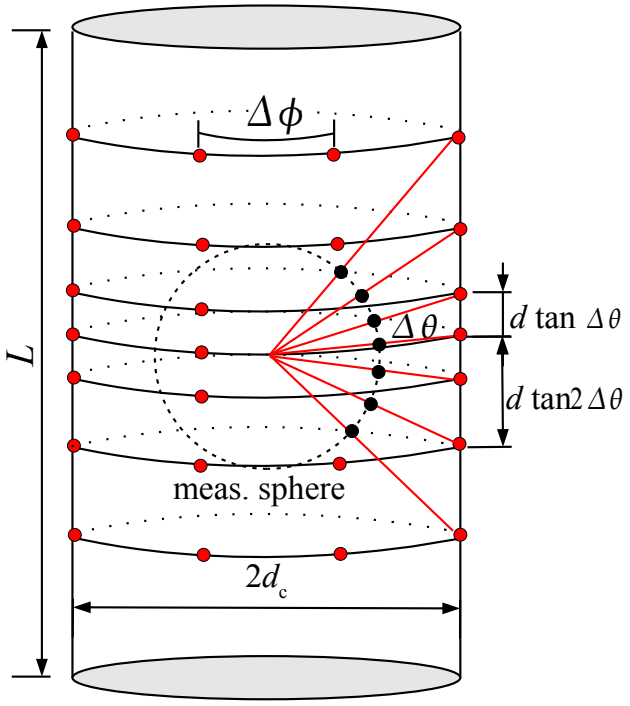

Figure 7.3: Data points projection from spherical to cylindrical measurement surface.

7.2 Planar Near-Field Measurements

7.2.1 Case I : Shaped Beam Reflector

The performance of the proposed sampling representation is assessed using both synthetic and real measurement data. The near field of a shaped beam antenna (as seen in Fig. 7.5) operating at 12 GHz is collected on a regular planar surface xz of size 1.8 m $*$ 2 m with $\lambda/2$ sample spacing in

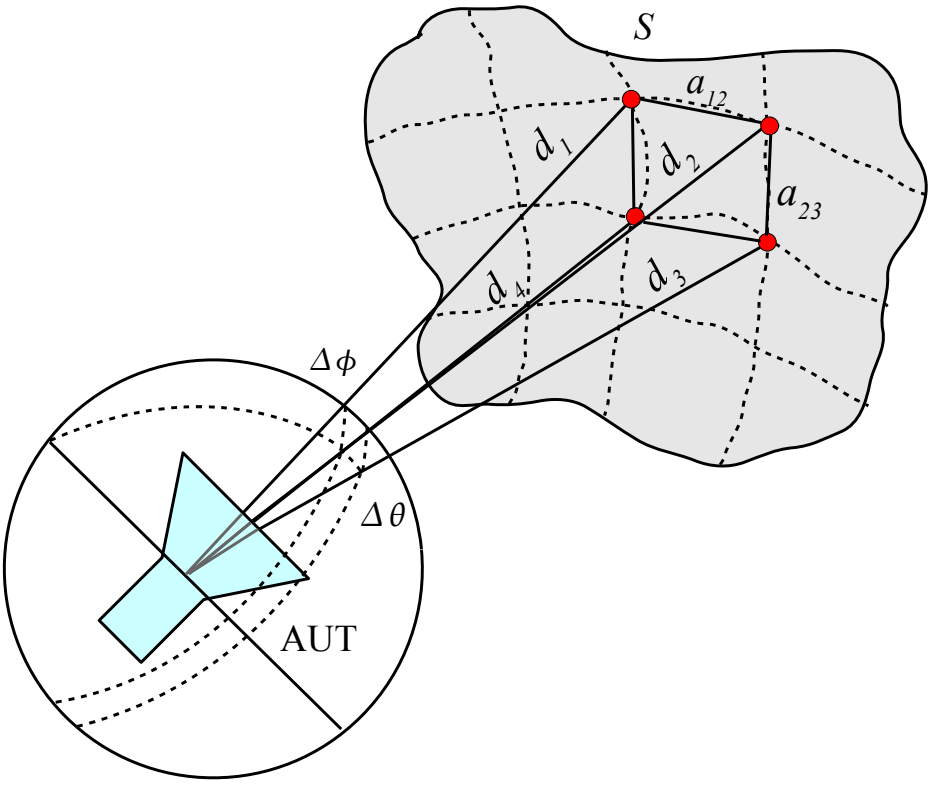

Figure 7.4: Nonredundant sampling representation over an arbitrary irregular surface.

both x- and z-directions, as shown in Fig. 7.6. The total number of measurement points considering $\lambda/2$ sample spacing equals $145 * 161$. The antenna is looking in -y-direction and is placed at $d_{\mathrm{p}} = 1.1$ m. The length and width of the shaped reflector is 0.5 m and 0.8 m, respectively. The translation of the plane wave spectra was processed using 4 hierarchical levels using the multilevel approach. Afterwards, the nonredundant sampling distribution is generated on the same scan surface in a way that it collects the near field in three increasing steps in the spacing from $\lambda/2$ to $3\lambda/2$ in both x and z, thereby greatly reducing the number of measurement points from 23 345 to only 7 921. The average iteration time with the code implemented in C and using an Intel(R) Core(TM) i7 CPU 920 @2.69 GHz processor was 58 s and 37 s using regular and nonredundant sampling, respectively. A total number of 110 iterations was employed.

Near-field data collected using regular and nonredundant sampling are processed using FI-AFTA. The transformed pattern obtained using regular near-field data is compared with the pattern using the reduced data set. Fig. 7.7 and Fig. 7.8 show the transformed E-plane and H-plane pattern cuts for the shaped-beam antenna along with the error level.

As observed, good results have been obtained even with 66% decrease in the number of measurement points. In a standard planar measurement setup, the near field is acquired by linear motion of the probe in vertical direction while stepping in the horizontal, or vice versa. Assuming the same measurement setup for the given example, the number of columns the probe has to traverse reduces from 161 to 97 and thus saving 40% of the measurement time. It should be mentioned here that only the number of columns is used to compute the reduction in measurement time since the probe traverses the columns in an on-the-fly manner. Therefore, any reduction in

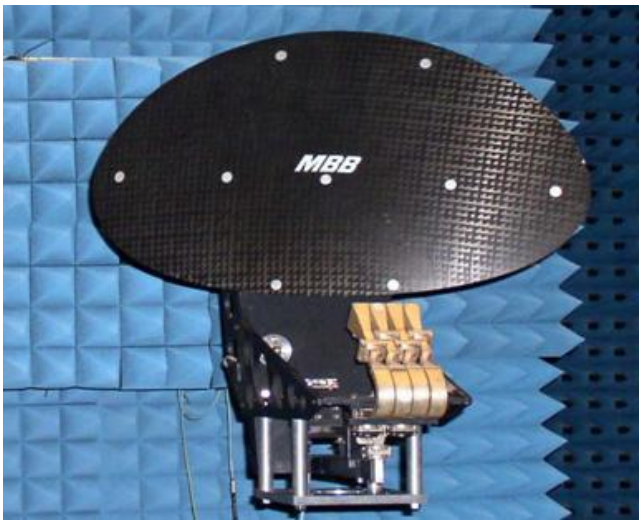

Figure 7.5: Shaped-beam antenna mounted in an anechoic chamber.

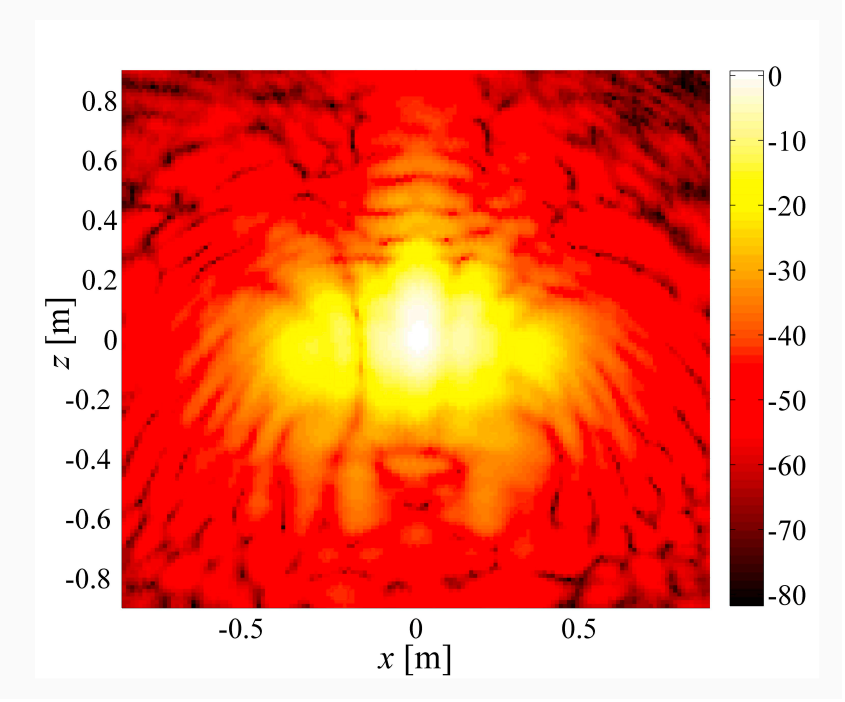

Figure 7.6: Near-field distribution [dB] of shaped-beam antenna on a planar surface.

the number of measurement points within the columns does not help in reducing the measurement time unless some intelligent scanning technique is adopted.

7.2.2 Case II : Medium Gain Antenna

In the second test case, we chose a medium gain antenna to confirm the proposed sampling criterion. The near field of the antenna operating at $11.95\,\mathrm{GHz}$ is collected on a planar surface xz

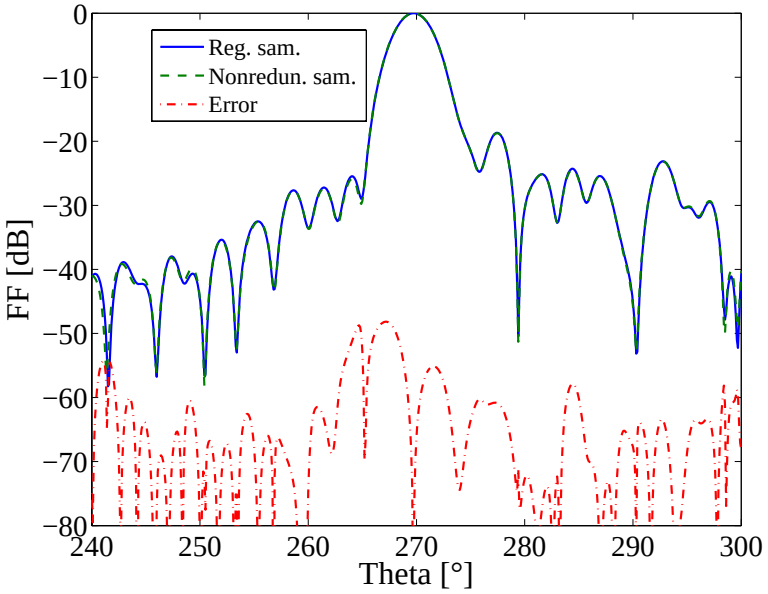

(a) E-plane pattern cut

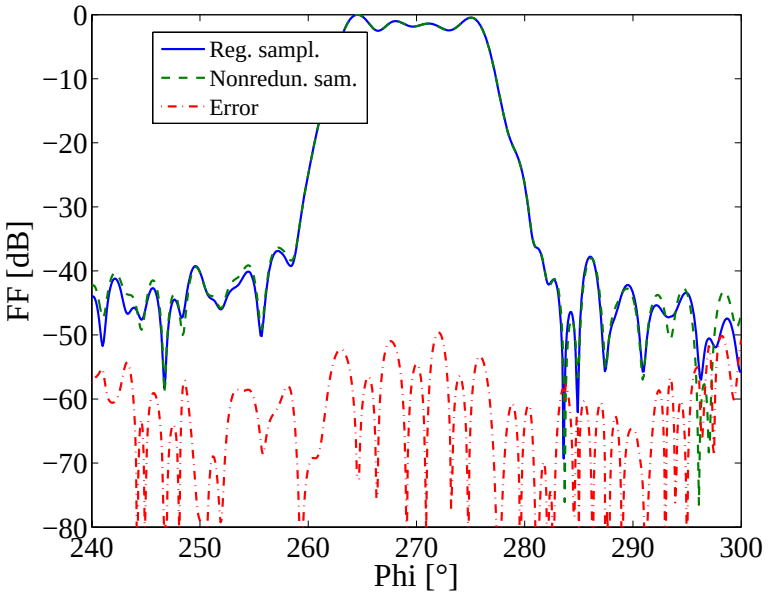

(b) H-plane pattern cut

Figure 7.7: Transformed E- and H-plane pattern cuts for the main polarisation of the shaped-beam antenna using a planar surface.

placed at $d_\mathrm{p} = 1.8288\,\mathrm{m}$. The length of the square shaped planar surface is 2.26 m. The antenna is looking in $-y$ direction and the near field distribution using the regular $\lambda/2$ sampling and the nonredundant sampling is shown in Fig. 7.9. The samples are mapped from a spherical to the planar grid in a same way as before i.e. the sample spacing increases in three steps from $\lambda/2$ to $3\lambda/2$ causing remarkable reduction in the number of measurement points as evident from the white spaces in Fig. 7.9 (b). The white spaces represent the skipped samples in reference to the regular $\lambda/2$ spacing. The AUT multipole order is 170 and along with 4 hierarchical levels in the multilevel setup, the average iteration time reduced from 124 s to 77 s using regular $\lambda/2$ and nonredundant

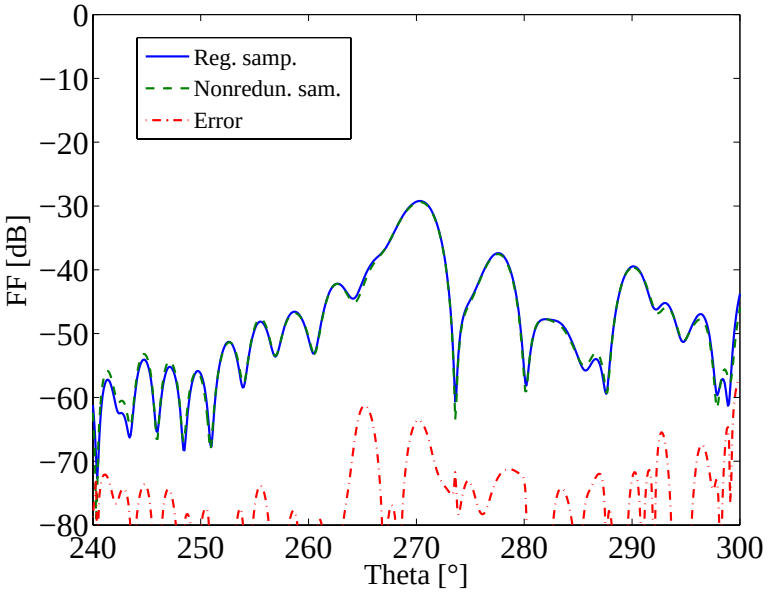

(a) E-plane pattern cut

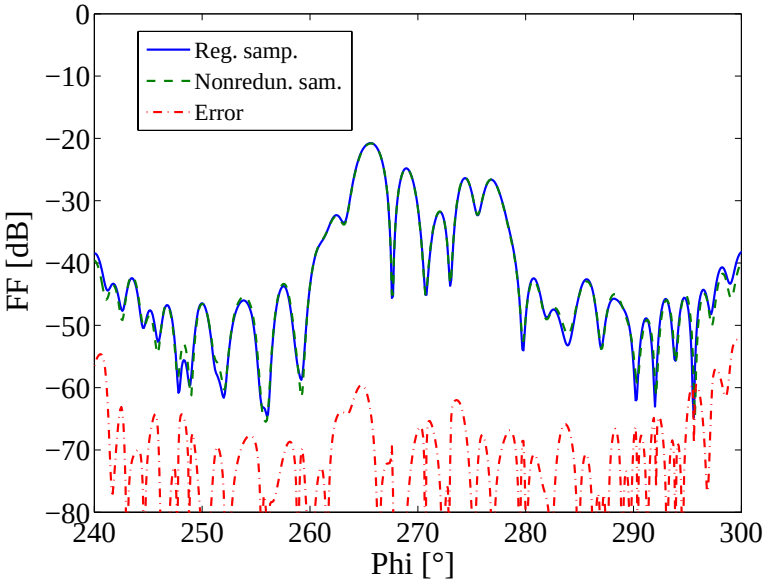

(b) H-plane pattern cut

Figure 7.8: Transformed E- and H-plane pattern cuts for the orthogonal polarisation of the shaped-beam antenna using a planar scan surface.

sampling, respectively.

The near-field data collected using both regular and nonredundant sampling is processed by FIAFTA. Fig. 7.10 and Fig. 7.11 show the transformed E- and H-plane main and orthogonal polarisation pattern cuts along with the error. The error level is computed by taking the logarithm of the difference between the normalized pattern magnitude using regular sampling and normalized pattern magnitude using nonredundant sampling. As obvious from the results, good agreement in the valid region of both patterns is observed even with 62% decrease in the number of sampling

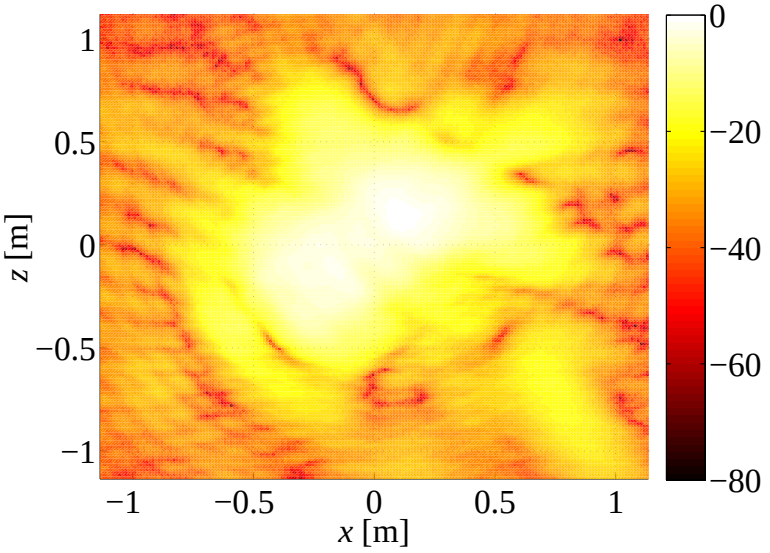

(a)

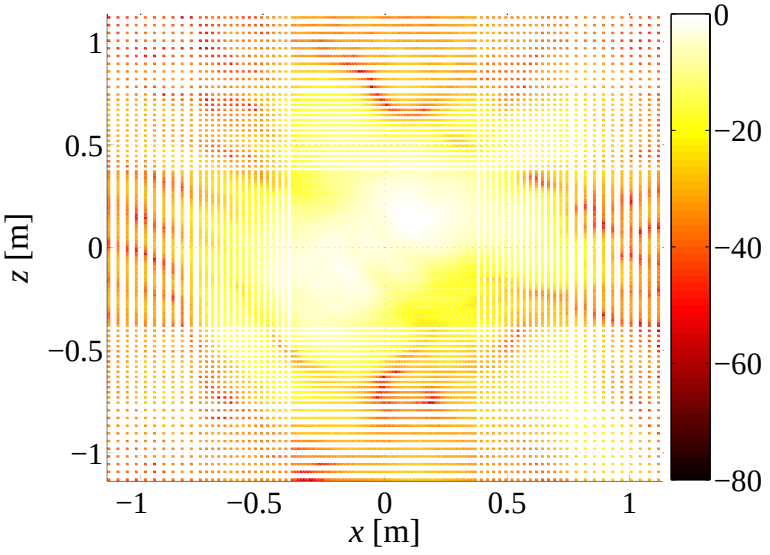

(b)

Figure 7.9: Near-field distribution [dB] of medium gain antenna on a planar surface with regular $\lambda/2$ (a) and the proposed nonredundant sampling (b).

points. Subsequently, the reduction in the measurement time is 40% as discussed in the previous example.

7.3 Cylindrical Near-Field Measurement

For the cylindrical case, a base station type antenna ($11\,\lambda$) with broad and narrow beam in ϕ- and θ-direction, respectively, is modeled using the synthetic modelling technique. The near field of the base station type antenna operating at 3 GHz is collected on a cylindrical surface at a radial

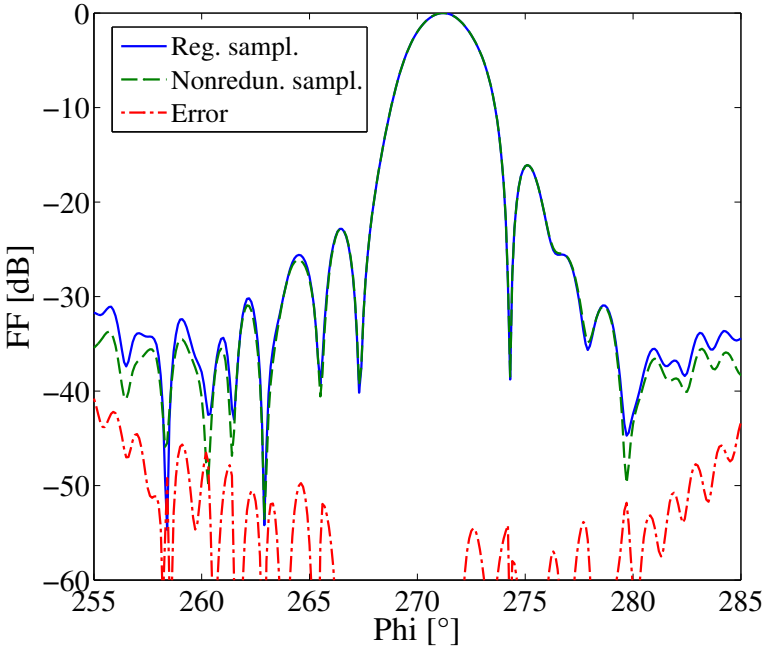

(a) E-plane pattern cut

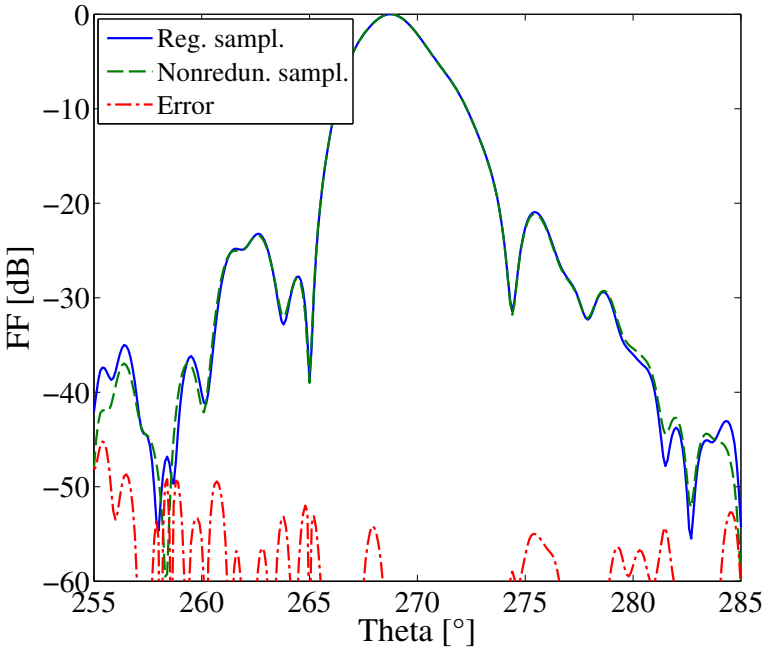

(b) H-plane pattern cut

Figure 7.10: Transformed E- and H-plane pattern cuts for the main polarisation of the medium gain antenna.

distance of 1.5 m. The height of the cylindrical surface is 4 m and both regular and nonredundant sampling representations are used for the computation of the near field. The AUT multipole order is 44 and the average iteration time consumed for a total of 69 iterations is 17 s and 9 s for regular and nonredundant sampling, respectively. The same processor as described in the planar measurement is used with the translation operator recursively processed at 3 hierarchical levels. The

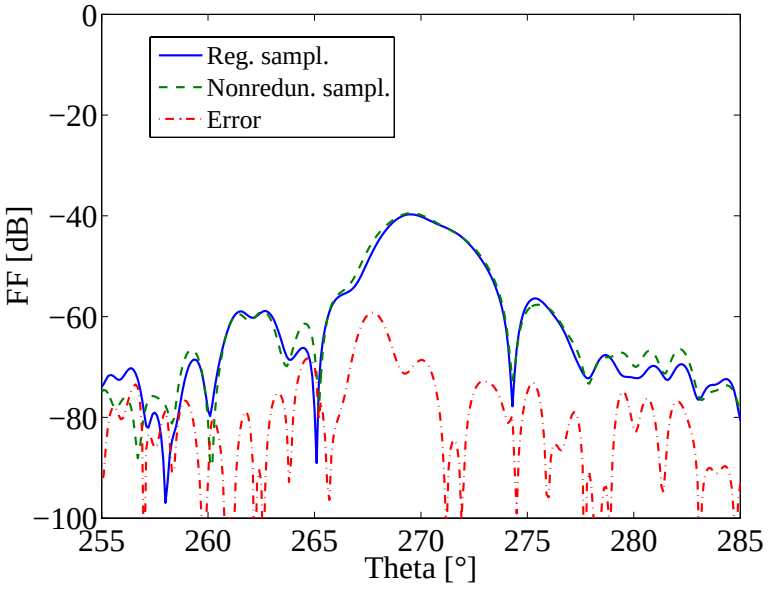

(a) E-plane pattern cut

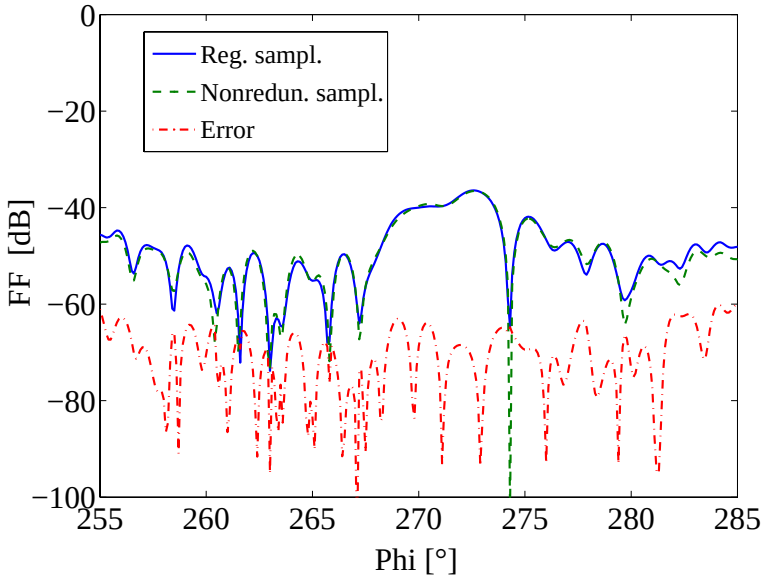

(b) H-plane pattern cut

Figure 7.11: Transformed E- and H-plane pattern cuts for the orthogonal polarisation of the medium gain antenna.

transformed pattern cuts are compared with the reference, as shown in Fig. 7.12 and Fig. 7.13. 55% measurement data reduction along with good accuracy in the valid region have been achieved. The number of ϕ-rings to be traversed by the probe is reduced from 81 to 37 and therefore also results in 55% reduction in the measurement time consumption.

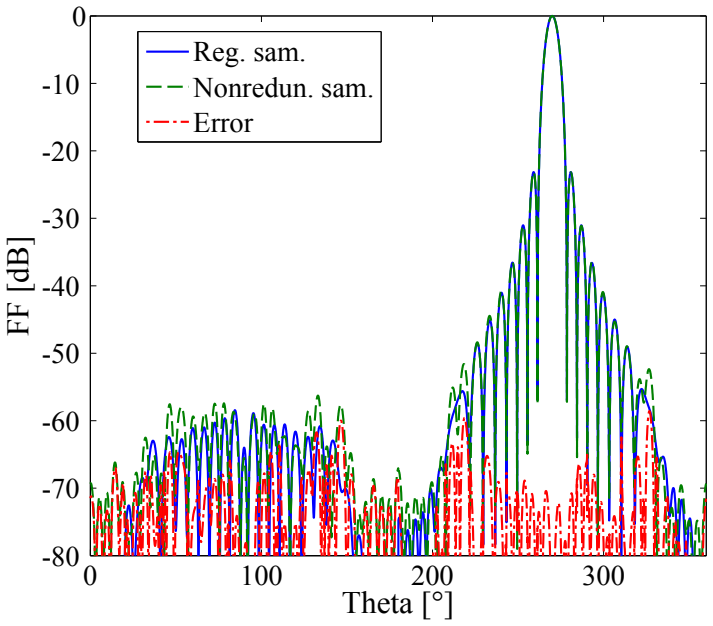

(a) E-plane pattern cut

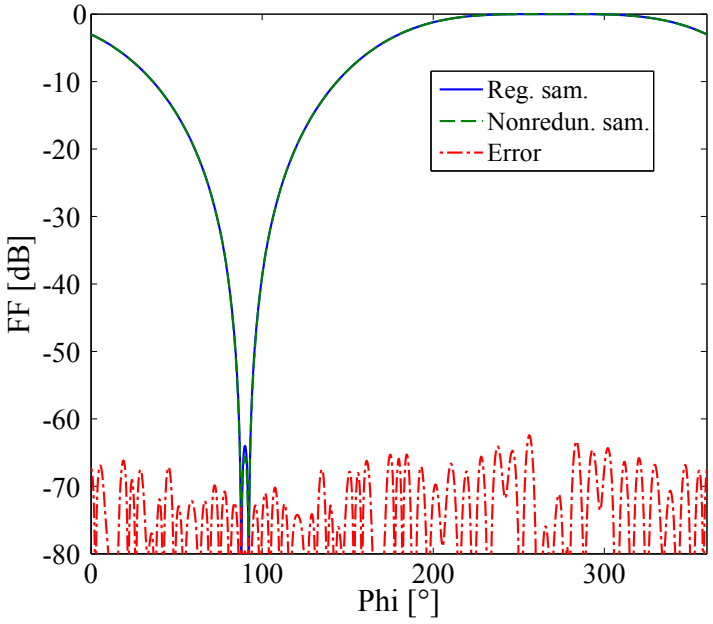

(b) H-plane pattern cut

Figure 7.12: Transformed E- and H-plane pattern cuts for the main polarisation of the base station type antenna using a cylindrical scanning surface.

7.4 Measurements on Arbitrary Grids

In order to prove the effectiveness of the sampling representation over arbitrary surfaces, a semi-spherical surface is created by varying the radial distance of each measurement point from the AUT. The extent of the sampling region (θ_t, ϕ_t) is computed using (7.9) to fulfill a 10° valid angle. The variation in the radius $r_{ab}(\theta, \phi)$ of each measurement point from the AUT is realized

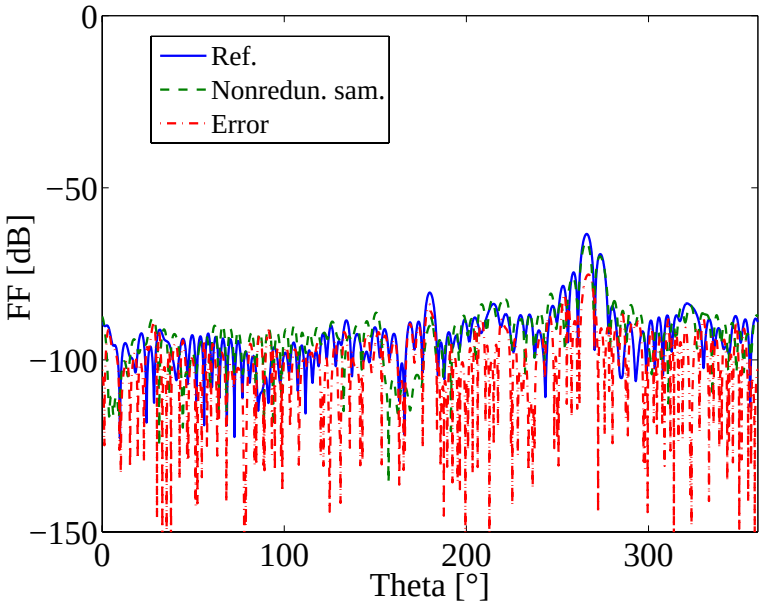

(a) E-plane pattern cut

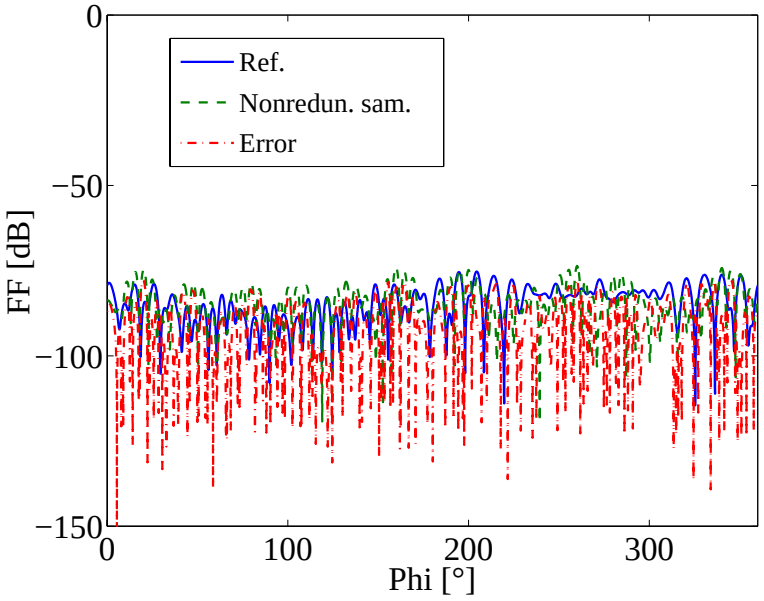

(b) H-plane pattern cut

Figure 7.13: Transformed E- and H-plane pattern cuts for the orthogonal polarisation of the base station type antenna using a cylindrical scanning surface.

as

$$r_{\mathrm{ab}}(\theta,\phi) = r_{\mathrm{sph}} + \mathrm{rand}\left(f\left(r_{\mathrm{sph}};\mu,\sigma^2\right)\right) \tag{7.12}$$

where r_{sph} is the radius of the perfect spherical surface and $f\left(r_{\mathrm{sph}};\mu,\sigma^2\right)$ is the Gaussian function used to superimpose a deviation in the mean radial distance. We use $\sigma = 0.2\,\mathrm{m}$ as a standard deviation to a mean radial distance μ of 1 m. The "rand" function randomly selects a value from the

Gaussian distribution with given parameters[4]. The AUT used is a synthetically modeled parabolic reflector ($64\,\lambda$) operating at 40 GHz. The near-field distribution over a perfectly planar surface (with $\lambda/2$ spacing) and over the semi-spherical surface with nonredundant sampling is shown in Fig. 7.14.

The equivalent planar representation for the arbitrary surface is shown over a valid angle of 10° and the variation in the magnitude profile of the arbitrary surface directly reflects the variation in the radial distance from the AUT. The sampling criterion is fulfilled in the same way as explained in section 3. The transformed E- and H-plane cuts are shown in Fig. 7.15 and Fig. 7.16. The best efficiency in the number of measurement points is observed as compared to the previous scenarios. To cover the same valid angle on a planar surface placed at 1 m using the traditional technique requires 51 000 data points while nonredundant sampling reduced it to only 8 649 data points and thus achieving a reduction of 83%. For this case, the translation operator was recursively processed through 5 different levels. A good accuracy was achieved after 12 iterations and can be further improved by employing more interpolation points and choosing an even lower GMRES residuum. The average iteration time for processing the irregular distribution of measurement points was 238 s.

[4]Though it is difficult to realize the described measurement surface practically, we consider it as a hard test case. Thereby, showing that even if the sampling representation is applied to such a corrupted surface the transformation results are not affected.

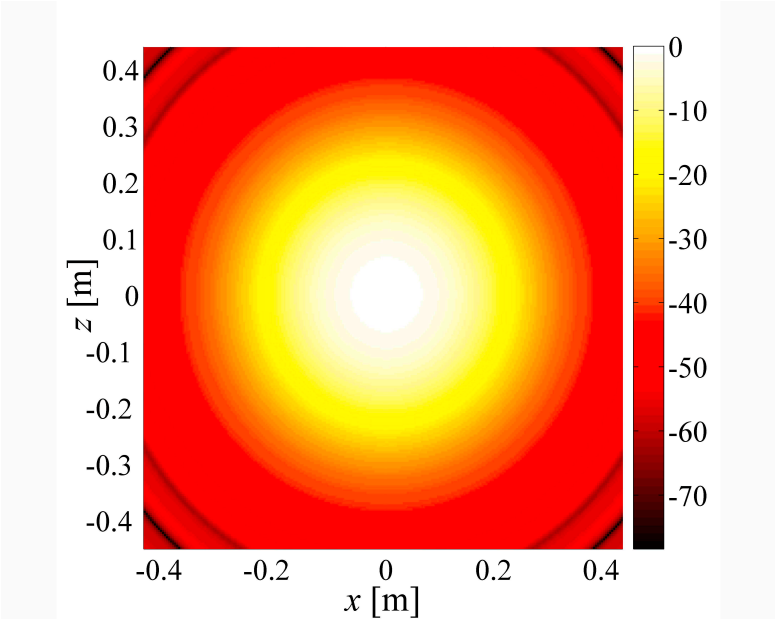

(a)

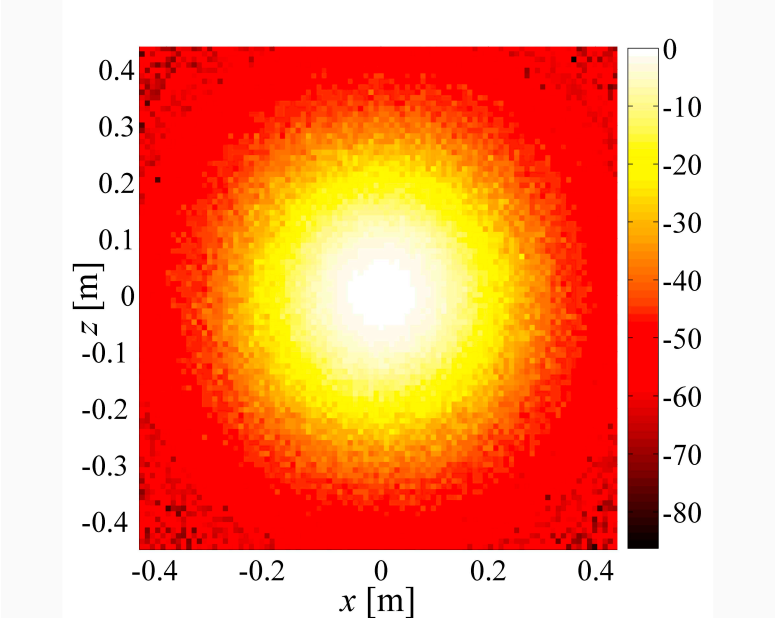

(b)

Figure 7.14: Near field [dB] collected on a regular planar surface (a) and over an arbitrary surface (b).

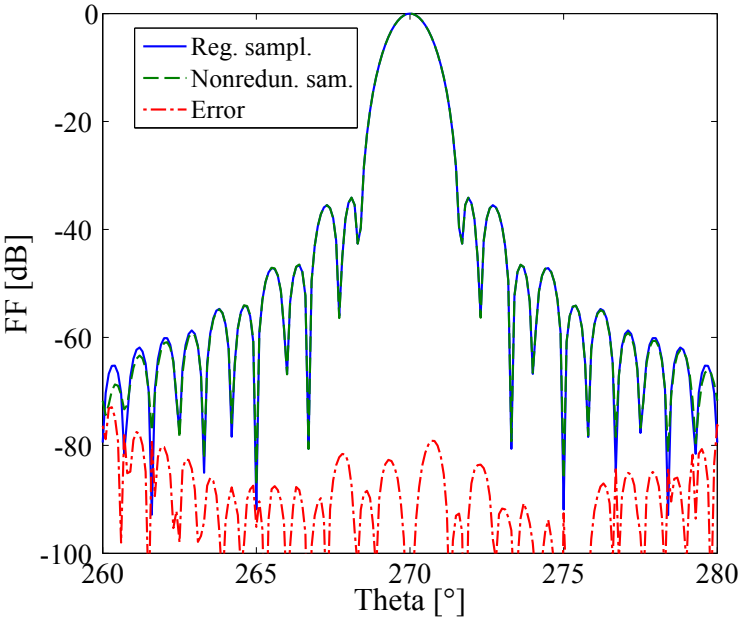

(a) E-plane pattern cut

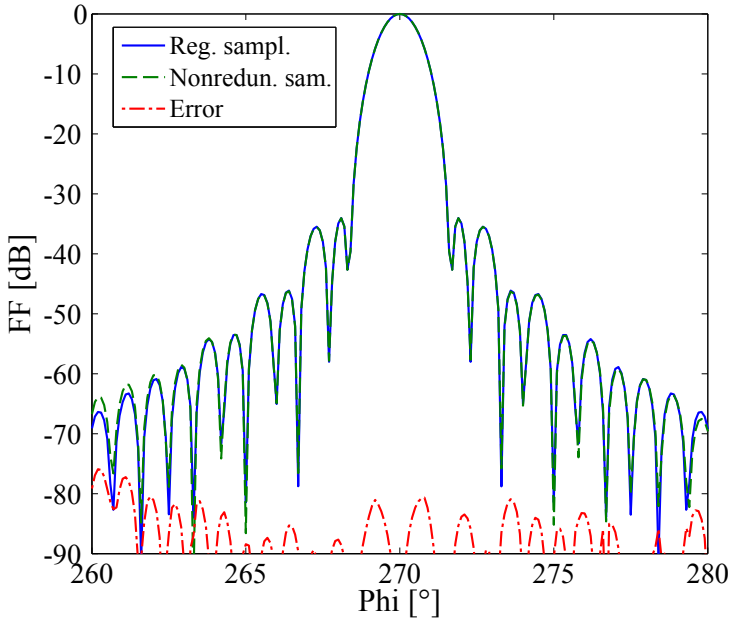

(b) H-plane pattern cut

Figure 7.15: Transformed E- and H-plane pattern cuts for the main polarisation of high gain parabolic reflector using an arbitrary scan surface.

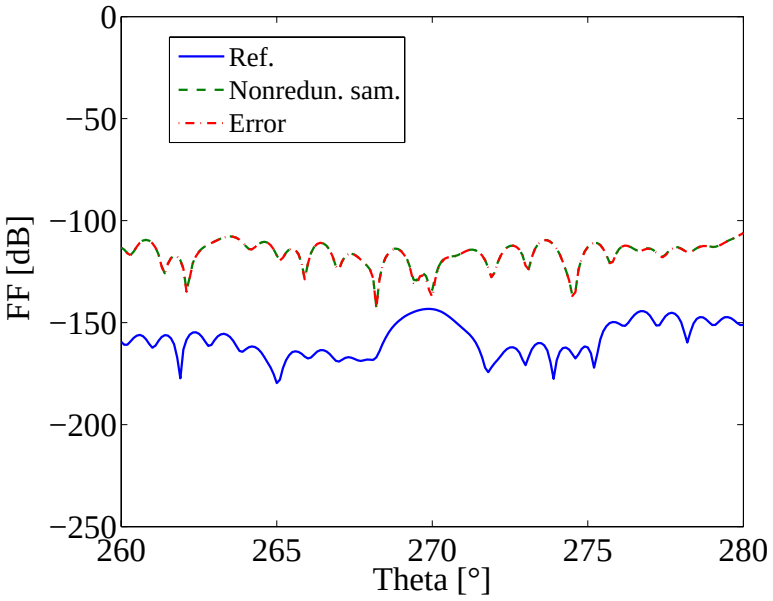

(a) E-plane pattern cut

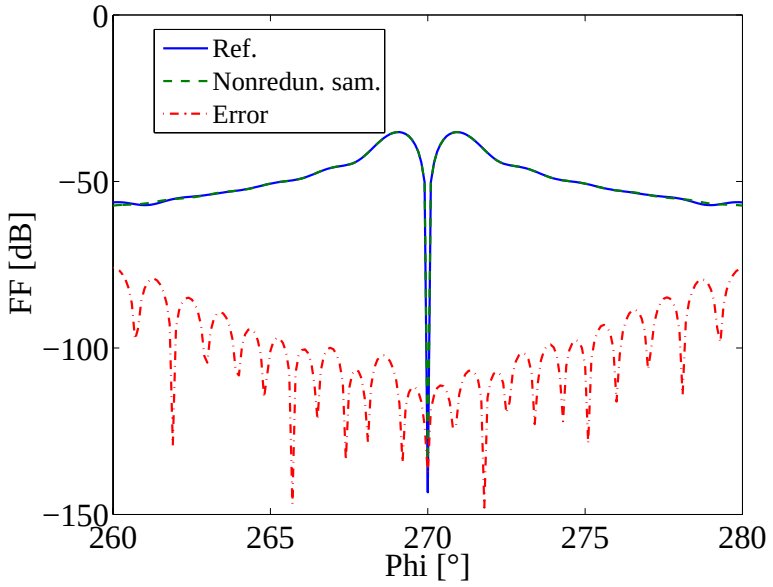

(b) H-plane pattern cut

Figure 7.16: Transformed E- and H-plane pattern cuts for the orthogonal polarisation of high gain parabolic reflector using an arbitrary scan surface.

Chapter 8

Summary and Future Work

A rigorous error analysis for near-field antenna measurements was performed for a recently developed multilevel plane wave based near-field far-field (NFFF) transformation algorithm also known as Fast Irregular Antenna Field Transformation Algorithm (FIAFTA). FIAFTA makes use of equivalent plane wave sources to reconstruct the antenna radiation pattern. It applies the Fast Multipole Method (FMM) for translating the plane waves from a complete Ewald sphere to the measurement points. The computational complexity is further reduced by grouping the measurement points in an hierarchical structure by utilizing a multilevel FMM (MLFMM) like procedure. The major advantages of FIAFTA include measurements on arbitrary grids, since the plane wave translations can be carried out to arbitrary measurement points, and full probe correction.

The performance of FIAFTA was evaluated in comparison with the traditional planar near-field transformation technique making use of two dimensional Fast Fourier Transform (2D FFT). The 2D FFT based NFFF approach is efficient but limited to regular grids like planar, cylindrical, and spherical. Also, the computational complexity worsens when full probe correction is required in spherical transformation. During the error analysis, it was found that FIAFTA offers robust performance against planar near-field measurement errors like scan area truncation, probe pattern inaccuracies, fluctuations in data point spacing, RF amplitude inaccuracy, etc. The multiple reflection error could also be reduced by taking measurements on two partial planes rather than on four planes and using traditional transformation techniques as previously adopted. A huge reduction in the measurement time could thus be obtained while maintaining the accuracy level. The dominant performance of FIAFTA mainly comes from the fact that it utilizes the complete Ewald sphere of propagating plane waves and, unlike the 2D FFT based approach, it does not assume zero field outside the scan plane or a periodic repetition. Also, in the probe correction the whole probe pattern is used even for computing the near field at a single point. This is in contrast to the traditional transformation technique employing 2D FFT which reinforces the error by considering the inaccuracy in a specific direction.

The error analysis was, however, based on a single antenna and assumed only planar near-field measurements. Therefore, a rather demanding analysis was carried out by proper formulation of transmission equations so that the uncertainty in the far-field pattern and in the directivity of the antenna can be determined, most importantly, without the knowledge of the ideal far field. The linearity of the forward operator, used in the formulation of the transmission equation of FIAFTA, allowed to oversee the effect of near-field errors and to estimate the mean and the maximum error in the transformed far field. The analysis considered all kinds of antennas using arbitrary scanning grids and it also took computational errors into account. It was found that the accuracy of the estimated uncertainty is dependent on the knowledge of the near-field measurement inaccuracy,

which is usually available. The proposed model was applied to several antennas and the computed uncertainties were summarized in tabular form. The estimated far-field uncertainties showed good agreement with the reference far-field errors. In this way, by providing the input near-field data along with the magnitude of measurement inaccuracies, FIAFTA not only determines the radiation pattern but also provides the uncertainty in the pattern, directivity, etc. at the same time. The only a priori information required is the size of the antenna to determine the multipole order. Apart form the error analysis, a method to compute optimum parameters is described. Parameters like multilevel hierarchy, number of buffer boxes, residuum of GMRES solver, etc. are discussed based on the gained experience.

The second major part of the thesis dealt with the efficient sampling techniques to be utilized in the near-field measurements. Intelligent scanning techniques have been proposed for measurements on planar, cylindrical, and spherical scanning grids. The fundamental concept used in the scanning was to focus more on the regions with strong near-field variations as compared to smoothly varying regions. In this way, not only one can determine the antenna behavior but can also try to decrease the measurement burden to a great extent. An empirically derived decision criterion based on signal-to-noise ratio of the measured value was utilized to determine the abrupt changes in the near field. The proposed planar scanning involved moving the probe in rectangular spiral locus starting from the center and acquiring near-field data in the form of rings. Based on the near-field distribution, the alternate rings were measured and compared with the extrapolated values. The difference between the two then determined whether the skipped ring should be measured or not. Similarly, for cylindrical scanning, measurements in the form of vertical columns were proposed and based on near-field distribution specific columns were skipped. The analogy was then extended to the spherical scanning technique. Several examples using synthetic and measurement data were presented taking into account the reduction in the number of samples, the measurement time efficiency, and the obtained transformed far-field accuracy. The results showed promising behavior in relation to FIAFTA. The proposed procedure, however, cannot assure a certain accuracy in the transformed far field as it is empirically derived. Nevertheless, it can be used to roughly estimate the radiation pattern of the antenna by acquiring near field on a lower number of sampling points with minimum effort.

The exact derivation of the suitable sample spacing criterion and the representation of sampling points on arbitrary scanning grids was discussed afterwards. Adaptive acquisition of near-field measurement data along with innovative scanning techniques were also proposed. The sampling criterion was found depending on the electrical size of the antenna under test (AUT) and on the separation between the AUT and the measurement surface. The minimum number of samples required were directly linked with the number of unknowns in the linear system of equations derived considering spherical expansion of radiated AUT fields. The minimum number of samples were distributed on a sphere with uniform θ and ϕ spacing. These samples were then mapped to the planar and cylindrical scanning grids using the equator region of the sphere. The projections can also be carried out for any arbitrary grids. It was found that the sampling points were mainly concentrated in the central region of the scan plane and the data point spacing increased gradually in the outer region. A similar observation is valid for the cylindrical surfaces as well in which the sample spacing gradually increases from the center to the outer surface along the length of the cylinder. The sampling distribution was assessed using both synthetic and measured data and showed dramatic decrease in the number of data points and the measurement time.

The measured data utilized for the evaluation of the derived sampling criterion used sampling steps of $\lambda/2$, λ, and $3\lambda/2$ since the near field is traditionally acquired on a $\lambda/2$ grid. Therefore,

the maximum reduction in the sampling burden achieved was limited until 62%. A special measurement setup acquiring near-field data exactly at the projection points can determine the full strength of the proposed criterion. The near-field scanner should be programmed in a way that it traverses the probe in a rectangular spiral locus for planar measurements and skip the intermediate rings based on the decision criterion described in the thesis. For cylindrical and spherical measurements, a similar concept can be adapted which only measures the necessary points.

Bibliography

[1] Y. Alvarez, F. Las-Heraz, and M. R. Pino, "Reconstruction of Equivalent Currents Distribution over Arbitrary Three-Dimensional Surfaces Based on Integral Equation Algorithms," *IEEE Trans. Antennas Propag.*, Vol. 55, No. 12, 3460–3468, 2007.

[2] T. K. Sarkar and A. Taaghol, "Near-Field to Near-Field/Far-Field Transformation for Arbitrary Near-Field Geometry Utilizing an Equivalent Electric Current and MoM," *IEEE Trans. Antennas Propag.*, Vol. 47, No. 3, 566–573, 1999.

[3] A. Taaghol and T. K. Sarkar, "Near-Field to Near/Far-Field Transformation for Arbitrary Near-Field Geometry, Utilizing an Equivalent Magnetic Current," *IEEE Trans. Antennas Propag.*, Vol. 38, No. 3, 536–542, 1996.

[4] C. H. Schmidt and T. F. Eibert, "Multilevel Plane Wave Based Near-Field Far-Field Transformation for Electrically Large Antennas in Free-Space or Above Material Halfspace," *IEEE Trans. Antennas Propag.*, Vol. 57, No. 5, 1382–1390, 2009.

[5] http://www.smartinsights.com/mobile-marketing/mobile-marketing-analytics/mobile-marketing-statistics/

[6] http://mobithinking.com/mobile-marketing-tools/latest-mobile-stats

[7] E. Dudok and D. Fasold, "Analysis of Compact Antenna Test Range Configurations," *International Symposium on Antennas JINA*, Nice, France, 1986.

[8] J. Hartmann, J. Habersack, and H.-J. Steiner, "Antenna Measurement in Compact Ranges," *Workshop on Space Borne Antennae Technologies and Measurement Techniques*, Ahmedabad, India, 2002.

[9] A. D. Yaghjian, "An Overview of Near-Field Antenna Measurements," *IEEE Trans. Antennas Propag.*, Vol. 34, No. 1, 30–45, 1986.

[10] C. H. Schmidt, M. M. Leibfritz, and T. F. Eibert, "Fully Probe Corrected Near-Field Far-Field Transformation Employing Plane Wave Expansion and Diagonal Translation Operator," *IEEE Trans. Antennas Propag.*, Vol. 56, No. 3, 737–746, 2008.

[11] Institute of Electrical and Electronics Engineering (IEEE): "IEEE Standard No. 145: Definitions of Terms for Antennas," *IEEE Trans. Antennas Propag.*, Vol. AP-17, No. 3, May 1969; Vol. AP-22, No. 1, January 1974; and Vol. AP-31, No. 6, Part II, November 1983.

[12] C. H. Schmidt, *Antenna Measurement Techniques*, Lecture Notes: Lehrstuhl für Hochfrequenztechnik, Technische Universität München, Munich, Germany 2012.

[13] http://www.phys.hawaii.edu/ anita/new/papers/militaryHandbook/polariza.pdf

[14] R. E. Collin, *Antennas and Radiowave Propagation*, McGraw Hill Book Company, Singapore 1985.

[15] C. A. Balanis, *Modern Antenna Handbook*, John Wiley & Sons, Inc., USA 2008.

[16] C. A. Balanis, *Antenna Theory: Analysis and Design*, John Wiley & Sons, Inc., USA 1982.

[17] EM Software and Systems: *FEKO Suite 6.2 http://www.feko.info*.

[18] Computer Simulation Technology: *CST Microwave Studio 2010, http://www.cst.com*.

[19] M. Hiebel.: *Grundlagen der vektoriellen Netzwerkanalyse.* 2. Auflage, München: Rohde & Schwarz, 2007.

[20] J. A. Fordham, "An Introduction to Antenna Test Ranges, Measurements and Instrumentation," *Antenna Systems and Technology*, Vol. 2, No. 2, 1999.

[21] http://www.thehowlandcompany.com/

[22] D. Kerns, "Plane-Wave Scattering-Matrix Theory of Antennas and Antenna-Antenna Interactions," *National Bureau of Standards*, Boulder, CO, 1981.

[23] http://www.astrium.eads.net/en/equipment/compensated-compact-ranges.html

[24] A. D. Yaghjian, "Near-Field Antenna Measurements on a Cylindrical Surface: A Source Scattering-Matrix Formulation," *National Bureau of Standards*,Tech. Note 696, Boulder, 1977.

[25] J. Hansen, *Spherical Near-Field Antenna Measurements* , IEEE Electromagnetic Wave Series 26,UK, 1988.

[26] C. H. Schmidt and T. F. Eibert, "Assessment of Irregular Sampling Near-Field Far-Field Transformation Employing Plane-Wave Field Representation," *IEEE Antennas and Propag. Mag.*, Vol. 53, No. 3, 213–219, 2011.

[27] A. C. Newell, R. D. Ward, and E. J. McFarlane, "Gain and Power Parameter Measurements Using Planar Near-Field Techniques," *IEEE Trans. Antennas Propag.*, Vol. 36, No. 6, 792–803, 1988.

[28] K. T. Selvan, "A Modified Three-Antenna Gain Method to Simplify Uncertainty Estimation," *Progress in Electromagnetic Research (PIER)*, Vol. 57, 197–208, 2006.

[29] D. T. Paris, W. M. Leach, and E. B. Joy, "Basic Theory of Probe Compensated Near-Field Measurements," *IEEE Trans. Antennas Propag.*, Vol. 26, No. 3, 373–379, 1978.

[30] C. H. Schmidt, "Effiziente Nahfeldmesstecknik für groβe Antennen, beliebige Messoberflächen und echobehaftete Messumgebungen," *Doctoral Thesis, TUM*, 2010.

[31] J. J. Lee, E. M. Ferren, D. P. Woollen, and K. M. Lee, "Near-Field Probe Used as a Diagnostic Tool to Locate Defective Elements in an Array Antenna," *IEEE Trans. Antennas Propag.*, Vol. 36, No. 6, 884–889, 1988.

[32] M. M. Leibfritz, F. M. Landstorfer, and T. F. Eibert, "Diagnosis of Antenna Arrays Using Near-Field Antenna Measurements and a priori Information," *Proceedings of IEEE AP-S International Symposium*, Honolulu, USA, June 2007.

[33] R. Yaccarino and Y. Rahmat-Samii, "Phaseless Bi-Polar Planar Near-Field Measurements and Diagnostic of Array Antennas," *IEEE Trans. Antennas Propag.*, Vol. 47, No. 3, 574–583, 1999.

[34] C. Cappellino, A. Frandsen, and O. Breinbjerg, "Application of the SWE-to-PWE Antenna Diagnostic Technique to an Offset Reflector Antenna," *IEEE Antennas and Propag. Mag.*, Vol. 50, No. 5, 204–213, 2008.

[35] Y. Rahmat-Samii and J. Lemanczyk, "Application of Spherical Near-Field Measurements to Microwave Holographic Diagnosis of Antennas ," *IEEE Trans. Antennas Propag.*, Vol. 36, No. 6, 869–878, 1988.

[36] M. H. Francis, A. C. Newell, K. R. Grimm, J. Hoffman, and H. R. Schrank, "Planar Near-Field Measurements of Low-Sidelobe Antennas," *Journal of Research of the National Institute of Standards and Technology.*, 143–167, 1994.

[37] Nearfield Systems Inc. website: http://www.nearfield.com.

[38] MI Technologies Inc. website http://www.mitechnologies.com.

[39] R. D. Baird, A. C. Newell, and C. F. Stubenrauch, "A Brief History of Near-Field Measurements of Antennas at the National Bureau of Standards," *IEEE Trans. Antennas Propag.*, Vol. 36, No. 6, 727–733, 1988.

[40] J. E. Hansen and F. Jensen, "Spherical Near-Field Scanning at the Technical University of Denmark," *IEEE Trans. Antennas Propag.*, Vol. 36, No. 6, 734–739, 1988.

[41] E. B. Joy, "A Brief History of the Development of the Near-Field Measurement Technique at the Georgia Institute of Technology," *IEEE Trans. Antennas Propag.*, Vol. 36, No. 6, 740–745, 1988.

[42] A. C. Newell, "Error Analysis Techniques for Planar Near-Field Measurements," *IEEE Trans. Antennas Propag.*, Vol. 36, No. 6, 754–768, 1988.

[43] A. C. Newell, "Near Field Antenna Measurement Theory, Planar, Cylindrical and Spherical", Lecture Notes, Near-Field Systems Inc., 2009.

[44] T. Laitinen and O. Breinbjerg, "A first/third-order probe correction technique for spherical near field measurements using three probe orientations ," *IEEE Trans. Antennas Propag.*, Vol. 56, No. 5, 1259–1268, 2008.

[45] M. A. Qureshi, C. H. Schmidt, and T. F. Eibert, "Planar Near-Field Measurement Error Analysis For Multilevel Plane Wave Based Near-Field Far-Field Transformation," 33^{rd} *Annual AMTA Symposium*, 2011.

[46] R. Coifman, V. Rokhlin, and S. Wandzura, "The Fast Multipole Method for the Wave-Equation: A Pedestrian Prescription ," *IEEE Trans. Antennas Propag.*, Vol. 35, No. 3, 7–12, 1993.

[47] W. Chew, J. Jin, E. Michielssen, and J. Song, *Fast and Efficient Algorithms in Computational Electromagnetics*, Boston, MA: Artech House, 2001.

[48] A. Tzoulis and T. F. Eibert, "A Hybrid FEBI-MLFMM-UTD Method for Numerical Solutions of Electromagnetic Problems Including Arbitrariy Shaped and Electrically Large Objects ," *IEEE Trans. Antennas Propag.*, Vol. 53, No. 10, 3358–3366, 2005.

[49] J. Jackson, *Classical Electromagnetics*, 3rd ed. New York: Wiley, 1998.

[50] W. Jian, H. Jun, and N. Zaiping, "A Novel Strategy of the Multipole Numbers of the MLFMA," in *Proc. APMC Conf.*, Vol. 3, Dec. 2005.

[51] Y. Saad, *Iterative Methods for Sparse Linear Systems* , 2^{nd} ed. Society of Industrial and Applied Mathematics, 2003.

[52] R. Laroussi and G. I. Costache, "Far-Field Predictions from Near-Field Measurements using an Exact Integral Equation Solution," *IEEE Trans. Antennas Propag.*, Vol. 36, No. 3, 189–195, 1994.

[53] H. Y. Chao, C. Lin, K. Pirapaharan, and W. C. Chew, "Fast Field Calculation by a Multilevel Fast Multipole Algorithm for Large Complex Radiators and Scatterers," in *International APS Symposium*, Columbus, Ohio, 2003.

[54] T. F. Eibert, Ismatullah, E. Kaliyaperumal, and C. H. Schmidt, "Inverse Equivalent Surface Current Method with Hierarchical Higher Order Basis Function, Full Probe Correction and Multilevel Fast Multipole Acceleration," *Progress in Electromagnetics Research*, Vol. 106, 377–294, 2010.

[55] T. B. Hansen, "Spherical Near-Field Scanning with Higher-Order Probes," *IEEE Trans. Antennas Propag.*, Vol. 59, No. 11, 4049–4059, 2011.

[56] T. Laitinen and O. Breinbjerg, "A First/Third-Order Probe Correction Technique for Spherical Near Field Measurements using Three Probe Orientations," *IEEE Trans. Antennas Propag.*, Vol. 56, No. 5, 1259–1268, 2008.

[57] M. A. Qureshi, C. H. Schmidt, K. A. Yinusa, and T. F. Eibert, "Far-Field Uncertainty Due to Instrumentation Errors in Multilevel Plane Wave Based Near-Field Far-Field Transformed Planar Near-Field Measurements," 6^{th} *European Conference on Antennas and Propagation*, Prague, Czech, 2012.

[58] M. A. Qureshi, C. H. Schmidt, and T. F. Eibert, "Probe Pattern Inaccuracy in Multilevel Plane Wave Based Near-Field Far-Field Transformed Planar Near-Field Measurements," *IEEE International Symposium on Antennas and Propagation*, Chicago, IL, 2012.

[59] M. A. Qureshi, C. H. Schmidt, and T. F. Eibert, "Comparative Probe Parameter Error Analysis with a Novel Approach for Reduced Probe-AUT Interaction," 34^{rd} *Annual AMTA Symposium*, Bellevue, WA, 2012.

[60] C. H. Schmidt, D. T. Schobert, and T. F. Eibert, "Electric Dipole Based Synthetic Data Generation for Probe-Corrected Near-Field Measurements," 5^{th} *European Conference on Antennas and Propagation*, 2011.

[61] A. D. Yaghjian, "Upper Bound Errors in Far-Field Antenna Parameters Determined From Planar Near-Field Measurements, Part 1: Analysis," *National Bureau of Standards*, Tech. Note 667, 1975.

[62] A. C. Newell and M. L. Crawford, "Planar Near-Field Measurements on High Performance Array Antennas," *National Bureau of Standards*, NBSIR 74-380, 1974.

[63] P. Petre, and T. K. Sarkar, "Differences Between Modal Expansion and Integral Equation Methods for Planar Near-Field to Far-Field Transformations," *Progress In Electromagnetics Research*, PIER 12 , 37-56, 1996.

[64] E. B. Joy and D. T. Paris, "Spatial Sampling and Filtering in Near-Field Measurements," *IEEE Trans. Antennas Propag.*, Vol. AP-53, 253–261, 1972.

[65] C. H. Schmidt, M. A. Qureshi, and T. F. Eibert, "Near-Field Error Analysis of Arbitrary Scanning Grids Using Fast Irregular Antenna Field Transformation Algorithm," *Progress in Electromagnetics Research B (PIER B)*, Vol. 48, 197–220, 2013.

[66] G. P. Rodrigue, E. B. Joy, and C. P. Burns, "An Investigation of the Accuracy of Far-Field Radiation Patterns Determined from Near-Field Measurements," *Report:Georgia Institute of Technology*, Atlanta, Georgia, 1973.

[67] E. B. Joy, "Near-Field Range Qualification Methodology," *IEEE Trans. Antennas Propag.*, Vol. 36, No. 6, 836–844, 1988.

[68] O. M. Bucci, G. Schirinzi, and G. Leone, "A Compensation Technique for Probe Positioning Error in Planar Near-Field Measurements," *IEEE Trans. Antennas Propag.*, Vol. 36, No. 8, 1167–1172, 1988.

[69] L. A. Muth, and R. L. Lewis, "A General Technique to Correct Probe Position Errors in Planar Near-Field Measurements to Arbitrary Accuracy," *IEEE Trans. Antennas Propag.*, Vol. 38, No. 12, 1925–1932, 1990.

[70] F. D'Agostino, F. Ferrara, C. Gennarelli, R. Guerriero, and M. Migliozzi, "On the Compensation of Probe Positioning Errors when using a Nonredundant Cylindrical NF-FF Transformation," *Progress in Electromagnetics Research B (PIER B)*, Vol. 20, 321–335, 2010.

[71] A. C. Newell and C. F. Stubenrauch, "Effect of Random Errors in Planar Near-Field Measurements," *IEEE Trans. Antennas Propag.*, Vol. 36, No. 6, 769–773, 1988.

[72] O. M. Bucci and M. D. Migliore, "A New Method for Avoiding the Truncation Error in Near-Field Measurements," *IEEE Trans. Antennas Propag.*, Vol. 54, No. 10, 2940–2952, 2006.

[73] F. D'Agostino, F. Ferrara, C. Gennarelli, R. Guerriero, and G. Riccio, "An Effective Technique for Reducing the Truncation Error in the Near-Field Far-Field Transformation with Plane-Polar Scanning," *Progress in Electromagnetics Research (PIER)*, No. 73, 213–238, 2007.

[74] Yu. Ding, Y. Lin,Fu. De-min, and L. Q. Zhong, "Analysis and Simulation of System Phase Errors in Planar Near-Field Measurements on Ultra-Low Sidelobe Antennas," *Proceedings of 2010 IEEE International Conference on Ultra-Wideband*, Nanjing, China, 2010.

[75] F. J. Cano-Fácila, S. Burgos, and T. F. Sierra-Castañer, "New Methods to Reduce Leakage Errors in Planar Near-Field Measurements," 5^{th} *European Conference on Antennas and Propagation*, Rome, Italy, 2011.

[76] Rohde & Schwarz website: http://www2.rohde-schwarz.com

[77] A. Björck, *Numerical Methods for Least Squares Problems*, Philadelphia, PA:SIAM, 1996.

[78] C. H. Schmidt, M. A. Qureshi, and T. F. Eibert, "Plane Wave Based Near-Field Far-Field Transformation with Adaptive Field Translations," *URSI General Assembly and Scientific Symposium of International Union of Radio Science*, Istanbul, Turkey, 2011.

[79] K. A. Yinusa, C. H. Schmidt, and T. F, Eibert, "Modeling of Unknown Echoic Measurement Facilities with Equivalent Scattering Centers," 6^{th} *European Conference on Antennas and Propagation*, Prague, Czech, 2012.

[80] O. M. Bucci and C. Gennarelli, "Application of nonredundant sampling representations of electromagnetic fields to NF-FF transformation techniques," *International Journal of Antennas and Propagation*, Vol. 2012, ID: 319856, 2012.

[81] M. A. Qureshi, C. H. Schmidt, and T. F. Eibert, "Adaptive Sampling in Multilevel Plane Wave Based Near-Field Far-Field Transformed Planar Near-Field Measurements," *Progress in Electromagnetics Research (PIER)*, Vol. 126, 481–497, 2012.

[82] M. A. Qureshi, C. H. Schmidt, and T. F. Eibert, "Adaptive Sampling in Cylindrical and Spherical Near-Field Antenna Measurements," 34^{th} *Annual AMTA Symposium*, Bellevue, WA, 2012.

[83] M. A. Qureshi, C. H. Schmidt, and T. F. Eibert, "An Effective Non-redundant Sampling Representation for Planar Near-Field Antenna Measurements," 34^{th} *ESA Antenna Workshop*, Noordwijk, Netherlands, 2012.

[84] M. A. Qureshi, C. H. Schmidt, and T. F. Eibert, "Efficient Near-Field Far-field Transformation for Nonredundant Sampling Representation on Arbitrary Surfaces in Near-Field Antenna Measurements," *IEEE Trans. Antennas Propag.*, Vol. 61, No. 4, 2025-2033, 2013.

[85] P. Petre and T. K. Sarkar, "Planar near-field to far-field transformation using an equivalent magnetic current approach," *IEEE Trans. Antennas Propag.*, Vol. 40, No. 11, 1348-1356, 1992.

[86] E. Martini, O. Breinbjerg, and S. Maci, "Reduction of Truncation Errors in Planar Near-Field Aperture Antenna Measurements Using the Gerchberg-Papoulis Algorithm," *IEEE Trans. Antennas Propag.*, Vol. 56, No. 11, 3485–3493, 2008.

[87] H. Stark, and Y. Yang, *Vector Space Projections: A Numerical Approach to Signal and Image Processing, Neural Nets, and Optics*, Wiley-Interscience, 1988.

[88] F. D'Agostino, F. Ferrara, C. Gennarelli, R. Guerriero, G. Riccio, and C. Savarese, "An Efficient Technique to Lower the Error Due to the Truncation of the Scanning Region in a Bi-Polar Facility," *Microwave and Optical Technology Letters*, Vol. 49, No. 12, 3033–3037, 2007.

[89] F. D'Agostino, F. Ferrara, C. Gennarelli, R. Guerriero, and M. Migliozzi, "An Effective NF-FF Transformation Technique with Planar Spiral Scanning Tailored for Quasi-Planar Antennas," *IEEE Trans. Antennas Propag.*, Vol. 56, No. 9, 2981–2987, 2008.

[90] O. M. Bucci, F. D'Agostino, C. Gennarelli, G. Riccio, and C. Savarese, "NF-FF Transformation with Plane-Polar Scanning: Ellipsoidal Modelling of the Antenna," *Automatika*, Vol. 41, 159–164, 2000.

[91] M. A. Qureshi, C. H. Schmidt, and T. F. Eibert, "Cylindrical Near-Field Acquisition using an Efficient Sampling Representation along with Direct Near-Field Far-Field Transformation," 29^{th} *International Review of Progress in Applied Computational Electromagnetics*, Monterey, CA, 2013.

[92] F. Ferrara, C. Gennarelli, R. Guerriero, G. Riccio, and C. Savarese, "An efficient near-field to far-field transformation using the planar widemesh scanning ," *Journal of Electromagnetic Waves and Applications*, Vol. 21, No. 3, 341-357, 2007.

[93] D. J. van Rensburg, D. McNamara, and G. Parsons, "Adaptive Acquisition Techniques for Planar Near-Field Antenna Measurements," 33^{rd} *Annual AMTA Symposium*, Denver, CO, 2011.

[94] D. J. van Rensburg and D. McNamara, "Adaptive Acquisition Techniques for Planar Near-Field Antenna Measurements: Part 2," 34^{rd} *Annual AMTA Symposium*, Seattle, WA, 2012.

[95] M. A. Qureshi, C. H. Schmidt, and T. F. Eibert, "Adaptive Rectangular Spiral Acquisition Technique for Planar Near-Field Antenna Measurements," 7^{th} *European Conference on Antennas and Propagation*, Gothenberg, Sweden, 2013.

[96] O. M. Bucci, C. Gennarelli, and C. Savarese, "Representation of electromagnetic fields over arbitrary surfaces by a finite and nonredundant number of samples," *IEEE Trans. Antennas Propag.*, Vol. 46, No. 3, 351–359, 1998.

[97] O. M. Bucci and G. Franceschetti, "On the spatial bandwidth of scattered fields," *IEEE Trans. Antennas Propag.*, Vol. AP-35, No. 12, 1445–1455, 1987.

[98] F. D'Agostino, C. Gennarelli, G. Riccio, and C. Savarese, "Theoratical foundations of near-field-far-field transformations with spiral scannings," *Progress in Electromagnetics Research*, Vol. 61, 193–214, 2006.

[99] O. M. Bucci, and C. Gennarelli, "Application of nonredundant sampling representation of electromagnetic fileds to NF-FF transformation techniques," *International Journal of Antennas and Propagation.*, Vol. 2012, 1–14, 2011.

[100] F. D'Agostino, F. Ferrara, C. Gennarelli, G. Gennarelli, R. Guerriero and M. Migliozzi, "On the direct non-redundant near-field-to-far-field transformation in a cylindrical scanning geometry," *IEEE Antennas and Propag. Mag.*, Vol. 54, 130–138, 2012.

[101] O. M. Bucci, C. Gennarelli, G. Riccio, C. Savarese, and Speranza, V., "Non redundant representation of the electromagnetic fields over a cylinder with application to the NF-FF transformation," *Electromagnetic*, Vol. 16, 273–290, 1996.

[102] P. Leopardi, *Distributing points on the sphere: Partitions, separation, quadrature and energy*, Ph.D. Thesis, University of New South Wales, 2006.

List of Author's Publications

[1] M. A. Qureshi, C. H. Schmidt, and T. F. Eibert, "Planar Near-Field Measurement Error Analysis For Multilevel Plane Wave Based Near-Field Far-Field Transformation," 33^{rd} *Annual AMTA Symposium*, 2011.

[2] M. A. Qureshi, C. H. Schmidt, K. A. Yinusa, and T. F. Eibert, "Far-Field Uncertainty Due to Instrumentation Errors in Multilevel Plane Wave Based Near-Field Far-Field Transformed Planar Near-Field Measurements," 6^{th} *European Conference on Antennas and Propagation*, Prague, Czech, 2012.

[3] M. A. Qureshi, C. H. Schmidt, and T. F. Eibert, "Probe Pattern Inaccuracy in Multilevel Plane Wave Based Near-Field Far-Field Transformed Planar Near-Field Measurements," *IEEE International Symposium on Antennas and Propagation*, Chicago, IL, 2012.

[4] M. A. Qureshi, C. H. Schmidt, and T. F. Eibert, "Comparative Probe Parameter Error Analysis with a Novel Approach for Reduced Probe-AUT Interaction," 34^{rd} *Annual AMTA Symposium*, Bellevue, WA, 2012.

[5] M. A. Qureshi, C. H. Schmidt, and T. F. Eibert, "Adaptive Sampling in Multilevel Plane Wave Based Near-Field Far-Field Transformed Planar Near-Field Measurements," *Progress in Electromagnetics Research (PIER)*, Vol. 126, 481–497, 2012.

[6] M. A. Qureshi, C. H. Schmidt, and T. F. Eibert, "Adaptive Sampling in Cylindrical and Spherical Near-Field Antenna Measurements," 34^{th} *Annual AMTA Symposium*, Bellevue, WA, 2012.

[7] M. A. Qureshi, C. H. Schmidt, and T. F. Eibert, "Adaptive Sampling in Cylindrical and Spherical Near-Field Antenna Measurements," *IEEE Antennas and Propag. Magazine*, Vol. 55, No. 1, 243-249, 2013.

[8] M. A. Qureshi, C. H. Schmidt, and T. F. Eibert, "An Effective Non-redundant Sampling Representation for Planar Near-Field Antenna Measurements," 34^{th} *ESA Antenna Workshop*, Noordwijk, Netherlands, 2012.

[9] M. A. Qureshi, C. H. Schmidt, and T. F. Eibert, "Efficient Near-Field Far-field Transformation for Nonredundant Sampling Representation on Arbitrary Surfaces in Near-Field Antenna Measurements," *IEEE Trans. Antennas Propag.*, Vol. 61, No. 4, 2025-2033, 2013.

[10] C. H. Schmidt, M. A. Qureshi, and T. F. Eibert, "Near-Field Error Analysis of Arbitrary Scanning Grids Using Fast Irregular Antenna Field Transformation Algorithm," *Progress in Electromagnetics Research B (PIER B)*, Vol. 48, 197–220, 2013.

[11] M. A. Qureshi, C. H. Schmidt, and T. F. Eibert, "Adaptive Rectangular Spiral Acquisition Technique for Planar Near-Field Antenna Measurements," 7^{th} *European Conference on Antenna and Propagation*, Gothenberg, Sweden, 2013.

[12] M. A. Qureshi, C. H. Schmidt, and T. F. Eibert, "Cylindrical Near-Field Acquisition Using an Efficient Sampling Representation along with Direct Near-Field Far-Field Transformation," 29^{th} *International Review of Progress in Applied Computational Electromagnetics*, Monterey, CA, 2013.